Nuclear Instruments and Methods in Physics Research 221 (1984) 20–25
North-Holland, Amsterdam

THE DESIGN AND EVALUATION OF GRAZING INCIDENCE RELAY OPTICS

J.M. DAVIS, R.C. CHASE *, J.K. SILK and A.S. KRIEGER

American Science and Engineering, Inc., Cambridge, MA 02139, USA

X-ray astronomy, both solar and celestial, has many needs for high spatial resolution observations which have to be performed with electronic detectors. If the resolution is not to be detector limited, plate scales in excess of 25μm arc sec $^{-1}$, corresponding to focal lengths greater than 5 m, are required. In situations where the physical size is restricted, the problem can be solved by the use of grazing incidence relay optics. We have developed a system which employs externally polished hyperboloid–hyperboloid surfaces to be used in conjunction with a Wolter–Schwarzschild primary. The secondary is located in front of the primary focus and provides a magnification of 4, while the system has a plate scale of 28 μm arc sec^{-1} and a length of 1.9 m. The design, tolerance specification, fabrication and performance at visible and X-ray wavelengths of this optical system are described.

1. Introduction

Our understanding of the physical conditions existing in the solar corona and in particular of the importance of the interaction between the coronal gas and the solar magnetic field has increased rapidly during the past decade. This is a direct result of the technical achievements in the fabrication of grazing incidence optics which have enabled the spatial structures of the corona to be imaged at high resolution in soft X-rays. The visual identification of a diverse population of coronal structures has provided both a new framework for the reformulation of the more classical concepts of solar physics and an incentive for new ideas. Since many of the theoretical descriptions describe processes which occur over very small spatial scales, future advances will depend on the acquisition of even higher resolution observations.

In practice resolution is a function both of the intrinsic resolution of the optical system and the relationship of the size of the image to that of the detector pixel. In the past even images recorded on photographic emulsions have been detector limited [1] and the situation is much worse when solid state detectors are used. However, for space instruments, electronic imagery has several advantages over film. It provides better temporal resolution, it is easier to calibrate, and instrument recovery is not required. These are strong incentives for the development of electronic imaging systems and new techniques for improving resolution must be found.

When a system is limited by the detector, the two factors that affect the system angular resolution are the instrument's focal length and the dimensions of the detector pixel. Although considerable efforts are being made to improve the latter, which will undoubtedly prove fruitful, they are unlikely to surpass the performance of photographic film. Therefore, it is essential to simultaneously explore the alternative of increasing the focal length of the X-ray telescope.

As a numerical example, if we baseline the pixel dimensions at 25 μm, the focal length required to subtend an angle of 1 arc sec across a pixel is in excess of 5 m. Even this modest goal, which corresponds to a system resolution of order 2.8 arc sec (where we have defined the system resolution as $2\sqrt{2}$ pixel size), results in an instrument size which is sufficiently large to make it impractical for any but major programs. In normal incidence systems the solution to this problem would be to use secondary optics to increase the effective focal length by magnifying the primary image. Until recently this approach had not been followed for X-ray imaging because of the difficulties anticipated in the figuring of small grazing incidence optical elements and in the loss of signal to noise associated with the increased scattering from four reflections instead of the customary two. However, recent advances in fabrication technology, in particular in the in-process metrology and in the preparation of low-scatter surfaces, have made their development realistic. Consequently, under NASA sponsorship, we have designed a grazing incidence magnifier to be used in conjunction with an existing grazing incidence primarily to be used for solar studies.

1.1. Design considerations

Two distinct designs [2] for the magnifier are possible. Their principle of operation is shown in fig. 1 in which the focal distances are based on using an existing primary and a secondary magnification of 4. In the first

* Present address: Itek Optical Systems Division, Lexington, Massachusetts 02173, USA

0167-5087/84/$03.00

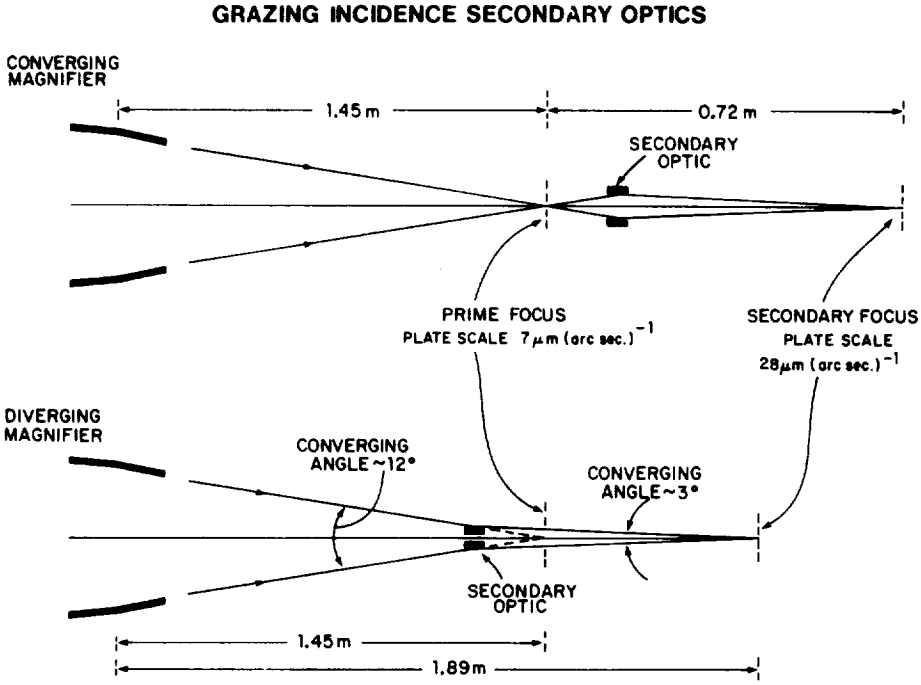

Fig. 1. Diagrams of the two possible designs for secondary grazing incidence optics. The dimensions refer to systems based on an existing primary mirror and a magnification of 4.

design the secondary optic acts as a microscope and is located behind the primary focal plane. It is known as a converging magnifier and has internally reflecting hyperboloid and ellipsoid surfaces. Alternatively the mirror can be placed in front of the focal plane where it acts as a Barlow lens. This configuration is known as a diverging magnifier and the mirror has externally reflecting hyperboloid-hyperboloid surfaces.

In both cases a considerable reduction in system length required for a given plate scale is achieved, the examples shown being roughly one third of the single mirror equivalent. In the present program, this parameter is of critical importance as the telescope will be flown as a sounding rocket payload. Of the two designs, for a given object distance and magnification, the diverging magnifier is the shorter and was selected. An additional benefit of this design is that the primary focused X-rays are bent through a smaller angle to reach the secondary focus, thus minimizing reflection losses and maximizing collecting area. In principle the design is fixed by choosing the magnification and the object distance. In practice increasing magnification lowers the system's speed, and increasing object distance, for a given magnification, lengthens the overall

Table 1
General properties of the X-ray mirrors

	Primary	Secondary
Figure	Wolter–Schwarzschild	hyperboloid–hyperboloid
Material	fused silica	nickel coated beryllium
Principal diameter	30.48 cm	3.15 cm
Focal length	144.9 cm	−19.4 cm
Geometrical area		
On-axis	41.5 cm^2	20.2 cm^2
3 arc min	41.1 cm^2	2.7 cm^2
Plate scale	7.0 μm (arc sec)$^{-1}$	28.1 μm (arc sec)$^{-1}$
Field of view	60×60 (arc min)^2	5×5 (arc min)^2
Resolving power (X-ray)	1 arc sec	1 arc sec

instrument and also increases the physical size of the polished area and a compromise has to be made. We chose a magnification of 4 which provides a plate scale of 28 μm arc sec^{-1} while retaining reasonable exposure times. The object distance, which is the separation between the principal plane of the diverging magnifier and the primary focus, is 14.55 cm. This leads to an overall length for the imaging system of 189 cm which is within the 2 m limit established for the experiment. The general properties of the primary and secondary mirrors are summarized for reference in table 1.

2. Specification and fabrication

The equations for the external mirror surfaces of the diverging magnifier are:
1st Hyperboloid:

$$\frac{(z+c)^2}{c^2-b^2}-\frac{x^2}{b^2}=1,$$

2nd Hyperboloid:

$$\frac{(z+2c+f)^2}{f^2-e^2}-\frac{x^2}{e^2}=1,$$

where $c=1.726981$, $b=0.147002$, $e=0.293203$, $f=6.870371$.
The constants are defined in fig. 2, which shows the geometrical properties of the surfaces and their relation to the primary mirror. The first hyperboloid is located so that one of its foci is co-spatial with the focus of the primary mirror. Its second focus is confocal with the first focus of the second hyperboloid. The second focus of this last surface forms, in turn, the secondary focus of the telescope. Since hyperboloids have two foci, small deviations from the design surface can be compensated for by axial displacements with no drawbacks other than a slight change in the overall focal length.

The mirror is fabricated, in two pieces, from optical grade beryllium. The reflective surfaces are electroless nickel which is applied to a depth of 0.13 mm over all the surfaces of the two elements. Each section is separately mounted to a central plate made of high-strength stainless steel. It is supported by four fingers which together intercept less than 3% of the open aperture. The steel chosen, 17-4PH, heat treated to condition H1150, provides a very close thermal match to the beryllium, which is essential to avoid radial distortions of the mirror surfaces under changing temperature conditions.

Although the primary mirror is made of uncoated fused quartz, there appear to be no scientific reasons for expecting the dissimilar surfaces to adversely affect performance. It will of course modify the passband of the instrument. The choice was made primarily for practical (e.g. cost, manufacturing capabilities of the local area) rather than scientific considerations. On the positive side it results in a lighter optic which allows the supporting fingers to be made narrower than would otherwise have been the case.

The dimensions of the pieces are shown in table 2,

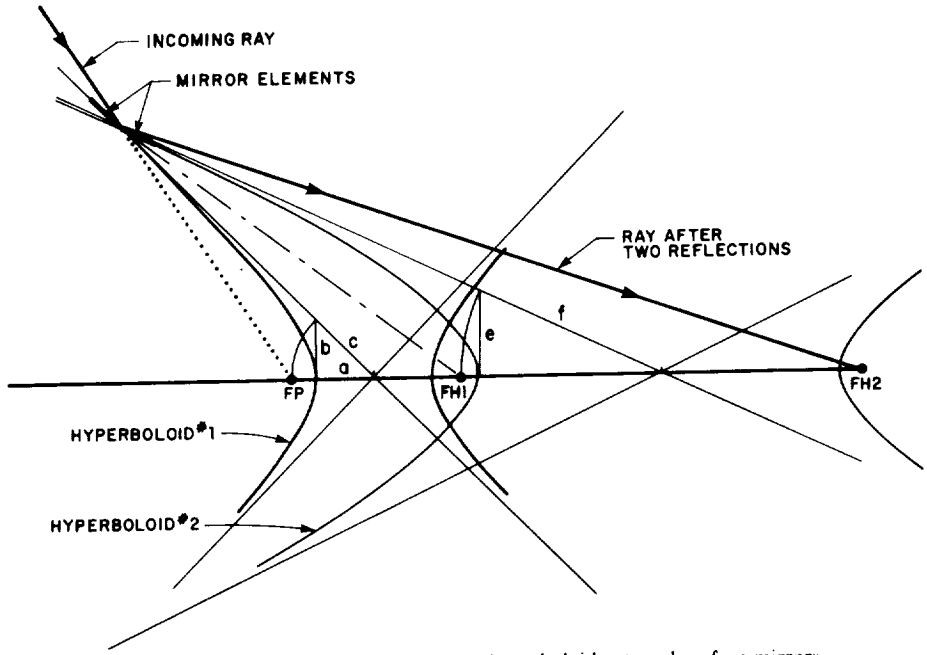

Fig. 2. The geometric relationships for hyperboloid–hyperboloid external surface mirrors.

Table 2
Secondary mirror demensions (Note: dimensions are in inches).

Diameter at front of 1st hyperboloid	1.40804
Diameter at rear of 1st hyperboloid	1.24878
Calculated diameter at mid-plane	1.24000
Diameter at front of 2nd hyperboloid	1.23527
Diameter at rear of 2nd hyperboloid	1.16433
Length of 1st hyperboloid	0.91006
Length of 2nd hyperboloid	0.74605
Gap for center plate	0.10000

and the tolerances placed on the reflecting surfaces are shown in table 3. The most demanding tolerances that must be met during the fabrication of the mirror are the roundness of the elements and the deviation of the local slope from that predicted by the design curve. The principal roundness criterion is the variation in the difference between the forward and aft radii of each piece as a function of azimuth. This tolerance is referred to as $\Delta(\Delta R)$ and for this mirror has to be less than 1.5 μm. This is a tighter specification than usual for grazing incidence mirrors and is a consequence of their small size. However, the tolerance was met in the fabrication of an X-ray microscope [3] which had similar dimensions, and depends on the precision of the turning machine, for which this is not an unreasonable requirement. The axial slope error is 0.05 μm per cm. Achievement of this tolerance depends more on the sensitivity of the in-process metrology than on the figuring techniques. Recent improvements using laser scanning instruments make this possible. A typical observation, after reduction, is shown in fig. 3. The observations are repeatable and demonstrate the ability to measure the surface at the nanometer level.

Fabrication [4] of the secondary mirrors takes place in the following steps. First, the selected beryllium blanks are diamond turned to the approximate dimensions of the mirror elements. Since the polished area is relatively small, roll over at the ends will have a major negative effect. Therefore the blanks are turned and

Table 3
Mirror tolerances (Note: tolerances are in inches).

Optical tolerance	Specification
Out of roundness $\Delta R = (R_{max} - R_{min})$	40×10^{-6}
$\overline{\Delta R}$	200×10^{-6}
$\Delta(\Delta R)$	6×10^{-6}
Sagittal depth	3×10^{-6}
Δ slope per axial length of one inch	5×10^{-6}
Surface finish rms roughness	< 10 Å
Performance tolerance	
Resolution	2 arc sec with a one arc sec design goal

Fig. 3. Analyzed data recorded during acceptance testing of an X-ray microscope [5]. In practice the data are continuous and deviations from the true surface of 1.0 nm or less are easily detectable.

lapped with removeable end pieces in place. The machined blanks are nickel plated and the surfaces are again diamond turned, lapped and the surface profile measured in-situ. The work is being performed in a modified Random [5] machine utilizing linear, air bearing slides to define tangents to the best fit circle. This circle is used to guide the lathe head which holds the mirror during turning and lapping. The radii of curvature, which in our case are on the order of 40 m, are determined with an accuracy of ± 2 cm and the location of the center of curvature with respect to the surface is known to be better than 1 part in 4000.

The in-process metrology uses a laser beam which is scanned over the surface in a controlled way and the local slope is determined from the reflected beam using a position-sensitive detector. The difference between the slope of the required surface and the best fit circle is corrected optically before display and the signal can also be integrated electronically to obtain the sagittal depth as a function of position. Once a satisfactory surface has been obtained the end pieces are removed from the finished mirror and the radial dimensions measured. Finally, the surfaces are superpolished to provide a low-scatter finish.

3. Expected performance

The design was based on optimizing the resolution and effective collecting area of the secondary mirror which are the most important performance parameters. Resolution depends strongly on off-axis angle, and collecting area is, in addition, a function of wavelength. The results of ray-tracing calculations are shown in figs. 4 and 5. NOTE: Resolution is defined in this case as the rms blur cirlce radius which in general underestimates the practical resolution except for on-axis rays.

Our ray tracing indicated that a trade-off had to be made between effective area, resolution and field of view. The design goal was to keep the rms blur circle

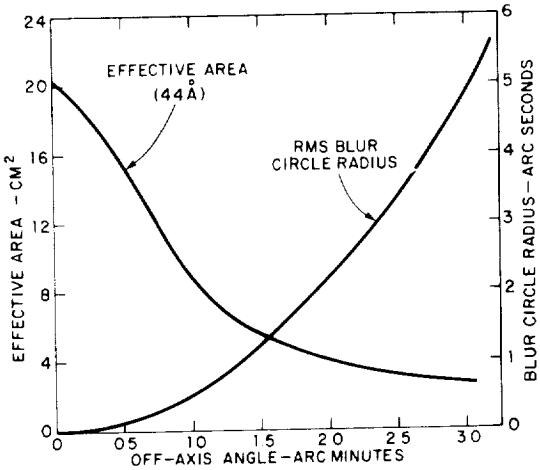

Fig. 4. The dependence of the effective area and the rms blur circle radius of the combined mirror system on the deviation from the optical axis of the incident ray.

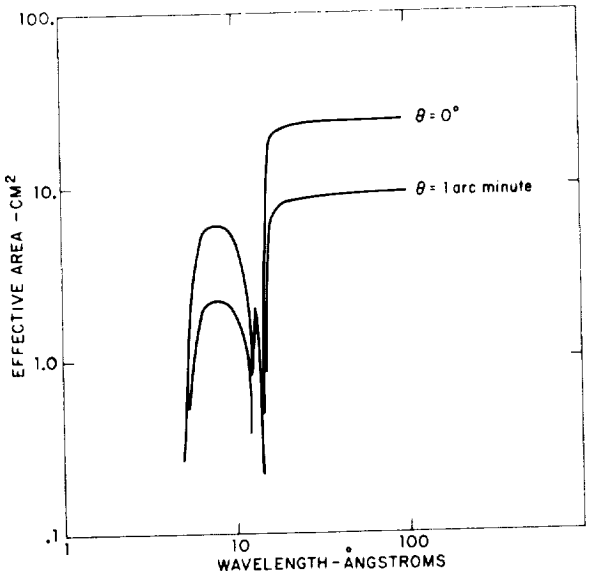

Fig. 5. The wavelength dependence of the effective area for on-axis ($\theta = 0°$) and off-axis ($\theta = 1$ arc min) rays.

radius below one arc second. This criterion limits the field of view to about 1 arc min. From fig. 4 it can be seen that even this restricted field is vignetted around the perimeter. The vignetting results in part from our choice of element length, for not all the primary rays which can contribute to the image are refocused. However, the rays that are missed are in fact poorly focused by the secondary mirror. Therefore, increasing the element length to catch these rays, although increasing the off-axis area, does so only at the expense of greatly increasing the blur circle radius. We have chosen to deliberately sacrifice some collecting area and accept the vignetting in order to maintain the highest image quality.

Alternatively, the field of view could be defined at the position where the effective area has dropped to one-tenth of its maximum value. This occurs a little beyond 3 arc min from the central axis. In practice solar active regions, which will typically be the target for this instrument, occupy areas of order (5×5) arc min^2; and the vignetting at the edge of the field of view will be about 80%. It remains to be seen how severe an impact this will have on the observations. However, since recording and display will be performed electronically, if the system is properly calibrated, it should be possible to remove the effect of the vignetting during display processing. The field of view has to be matched to the physical size of the detector. At the secondary focus, an angular displacement of 5 arc min corresponds to 0.84 cm which provides a reasonable fit to typical CCDs suitable for use in the soft X-ray region.

The on-axis effective area of the combined system is approximately 20 cm^2 which is approximately 50% of the primary alone. This is a result of the combination of reflection losses and the limit set on the element lengths by the resolution criterion. The increase in image size reduces the secondary image brightness by a further factor of 16; therefore, the brightness at the center of the secondary image will be reduced by a factor of 30 from the brightness of the same feature viewed in the primary image. Since imaging bright solar features on photographic emulsions requires exposure times of 1–3 s at the primary focus, exposure times up 100 s will be required at the secondary focus. Although this is possible, the temporal resolution would be poor and it is obvious that secondary optics and solid state detectors make natural partners. The increased sensitivity to soft X-rays of the latter, which is on the order of 1000, will allow exposure times of less than one second at the secondary focus. In this situation, time resolution is more likely to be limited by the data handling capability of the telemetry system than by the sensitivity of the detector.

4. Program status

Although it had been expected that the secondary optic would have been completed by the time of this workshop, this has not been the case. At this time turning and polishing of the first hyperboloid has just started. All the procedures that will be used have been tested on an aluminum blank and we have a high degree of confidence that the finished optic will meet our specifications.

Upon completion of the first hyperboloid the metrology will be reviewed and the surface of the second

hyperboloid recalculated if necessary. Following final assembly the spatial resolution of the optic will be tested in visible light using a USAF 1951 resolution target placed at the focus of a converging beam with an *f*-number of 4.6 and 97% occulted, the acceptance criterion at this stage is 2 arc sec resolution with 1 arc sec as a design goal.

Upon acceptance the optics performance will be tested in both visible light and X-rays in conjunction with the primary. Since the alignment of the two mirrors will be critical, we have designed a special alignment and holding mechanism which will be used for both flight and ground testing. The mechanism permits independent translation along three orthogonal axes together with rotations in pitch and yaw. Adjustment in increments of 2.54 μm is possible along the optical axis, in increments of 25 μm along the two orthogonal axes and of 1 arc sec about the two axes of rotation.

X-ray testing will be performed in AS&E's recently extended 100 m vacuum facility. Parameters measured will include spatial resolution, collecting area and point response function, both on- and off-axis and at several wavelengths including as a minimum 8.3 and 44 Å.

The revised delivery schedule has the optics being delivered in August 1983. The complete testing program will take a further six months. The results of these tests will be reported in a subsequent paper.

It is a pleasure to acknowledge the help of the staff of the Applied Optics Center where the secondary optic is being fabricated. We would also like to thank Alan DeCew who has contributed to the fabrication procedures.

The work is being performed under NASA contract NAS5-25496.

References

[1] J.M. Davis, A.S. Krieger, J.K. Silk and R.C. Chase, Proc. Soc. Photo-Opt. Instr. Eng. 184 (1979) 96.
[2] R.C. Chase, A.S. Krieger and J.H. Underwood, Appl. Opt. 21 (1982) 4446.
[3] J.K. Silk, Proc. Soc. Photo-Opt. Instr. Eng. 184 (1979) 40.
[4] Applied Optics Center, Burlington, Massachusetts 01803, USA.
[5] Random Devices Inc., Newbury, Massachusetts 01950, USA.

4.13 The Spatial Distribution of 6 Centimeter Gyroresonance Emission from a Flaring X-Ray Loop

S.W. Kahler, D.F. Webb, and J.M. Davis

American Science and Engineering, Inc.
Cambridge, Massachusetts 02139

and

M.R. Kundu

Astronomy Program
University of Maryland
College Park, Maryland 20742

THE SPATIAL DISTRIBUTION OF 6 CENTIMETER GYRORESONANCE EMISSION FROM A FLARING X-RAY LOOP

S. W. KAHLER, D. F. WEBB, and J. M. DAVIS

American Science and Engineering, Inc., Cambridge, MA 02139, U.S.A.

M. R. KUNDU

Astronomy Program, University of Maryland, College Park, MD 20742, U.S.A.

(Received 5 September, 1983; in final form 12 March, 1984)

Abstract. We compare simultaneous high resolution soft X-ray and 6 cm images of the decay phase of an M3 X-ray flare in Hale Region 16413. The photographic X-ray images were obtained on an AS & E sounding rocket flown 7 November, 1979, and the 6 cm observations were made with the VLA. The X-ray images were converted to arrays of line-of-sight emission integrals and average temperature throughout the region. The X-ray flare structure consisted of a large loop system of length ~ 1.3 arc min and average temperature $\sim 8 \times 10^6$ K. The peak 6 cm emission appeared to come from a region below the X-ray loop. The predicted 6 cm flux due to thermal bremsstrahlung calculated on the basis of the X-ray parameters along the loop was about an order of magnitude less than observed. We model the loop geometry to examine the expected gyroresonance absorption along the loop. We find that thermal gyroresonance emission requiring rather large azimuthal or radial field components, or nonthermal gyrosynchrotron emission involving continual acceleration of electrons can explain the observations. However, we cannot choose between these possibilities because of our poor knowledge of the loop magnetic field.

1. Introduction

Recently advances have been made in mapping the microwave emission of both the flaring (Kundu and Vlahos, 1982) and the quiet (Kundu, 1982) Sun with high temporal and spatial resolution. While gyrosynchrotron emission from nonthermal electrons appears to be the obvious radiation mechanism for the flaring case, thermal mechanisms involving bremsstrahlung and gyroresonance emission at harmonics of the gyrofrequency are the best candidates in the non-flaring case. In the latter case the gyroresonance absorption process has been invoked for strong sunspot-associated magnetic fields and bremsstrahlung for the plage regions of weaker fields (Kundu *et al.*, 1977; Alissandrakis *et al.*, 1980; Felli *et al.*, 1981).

The combination of simultaneous X-ray observations and microwave maps has constrained the range of possible microwave emission mechanisms by allowing a determination of the electron thermal temperature T_e, linear emission integral $\int n_e^2 \, dl$, and, perhaps, electron density n_e, independently of the microwave observations. Some observers (Chiuderi-Drago *et al.*, 1982; Lang *et al.*, 1983; Shibasaki *et al.*, 1983) have found good agreement between the combined X-ray and microwave observations and the accepted radiation mechanisms for quiescent active region features. Others (Webb *et al.*, 1983; Schmahl *et al.*, 1982) have found some significant differences between the detailed locations of the active region X-ray and microwave sources. In cases of high

Solar Physics **92** (1984) 271–281. 0038–0938/84/0922–0271$01.65.

microwave brightness temperature, T_b, but low X-ray brightness, thermal bremsstrahlung is not a viable microwave emission mechanism, and gyroresonance absorption theory may require unrealistically large magnetic fields.

An interesting long-lasting burst on 19 May, 1979 was mapped at 20 cm by Velusamy and Kundu (1981). The 20 cm emission occurred in three looplike structures and was interpreted as either thermal gyroradiation or as nonthermal gyrosynchrotron emission. Subsequent comparison of these maps with soft X-ray images from the P78–1 satellite revealed that only one of the three 20 cm sources coincided with an X-ray source, leading Schmahl *et al.* (1983) to favor the nonthermal interpretation. The observations discussed here are similar to that event in that we have simultaneous 6 cm microwave maps and soft X-ray images during the decay of an M3/1B flare on 7 November, 1979. We find that the region of peak 6 cm emission is not spatially coincident with the bright soft X-ray loop responsible for the bulk of the X-ray emission. The mechanism of the 6 cm radiation emitted by the X-ray loop is discussed in detail using gyroresonance absorption theory and a simple model of the loop magnetic field.

2. Observations and Data Analysis

2.1. Soft X-ray data

The American Science and Engineering (AS & E) rocket flight of 7 November, 1979 was the first of two flights to observe the X-ray Sun at solar maximum. The grazing incidence X-ray telescope payload included a Wolter-Schwarzchild fused quartz mirror and four different filters. Full-disk images with a spatial resolution of approximately 2 arc sec were obtained on Kodak SO–212 film between 20 : 51 and 20 : 56 UT.

The brightest feature of these images was a flare loop in Hale Region 16413. For our quantitative analysis of this loop we used two adjacent exposures through a 1/2 mil beryllium filter and similar exposures through a 1 micron aluminized polypropylene filter, both obtained at about 20 : 52 UT. The images were converted to arrays of film density with pixels of size 2.8 arc sec square. The analytic procedure given in Vaiana *et al.* (1977) for conversion of film density to effective temperature and linear emission integral was followed closely. Calibrations of film density to energy flux and point spread functions at 8.3 Å and 44 Å were used in the analysis of the beryllium and polypropylene images, respectively. The deconvolved energy flux density image obtained with the polypropylene filter is shown in Figure 1. Arrays of 4 × 4 pixel averages (11.4 arc sec square) were used to obtain maps of effective temperatures and linear emission integrals at points along the loop.

2.2. Microwave data

The radio observations were made of Hale Region 16413 at 6 cm with the Very Large Array (VLA) of the National Radio Astronomy Observatory between 19 : 50 and 20 : 37 and then 20 : 50 and 21 : 18 UT. Seventeen antennas were available during the observations, providing good $u - v$ coverage. The system was sensitive to structures smaller than 3 arc min because the shortest spacing used for these maps was 1200 λ.

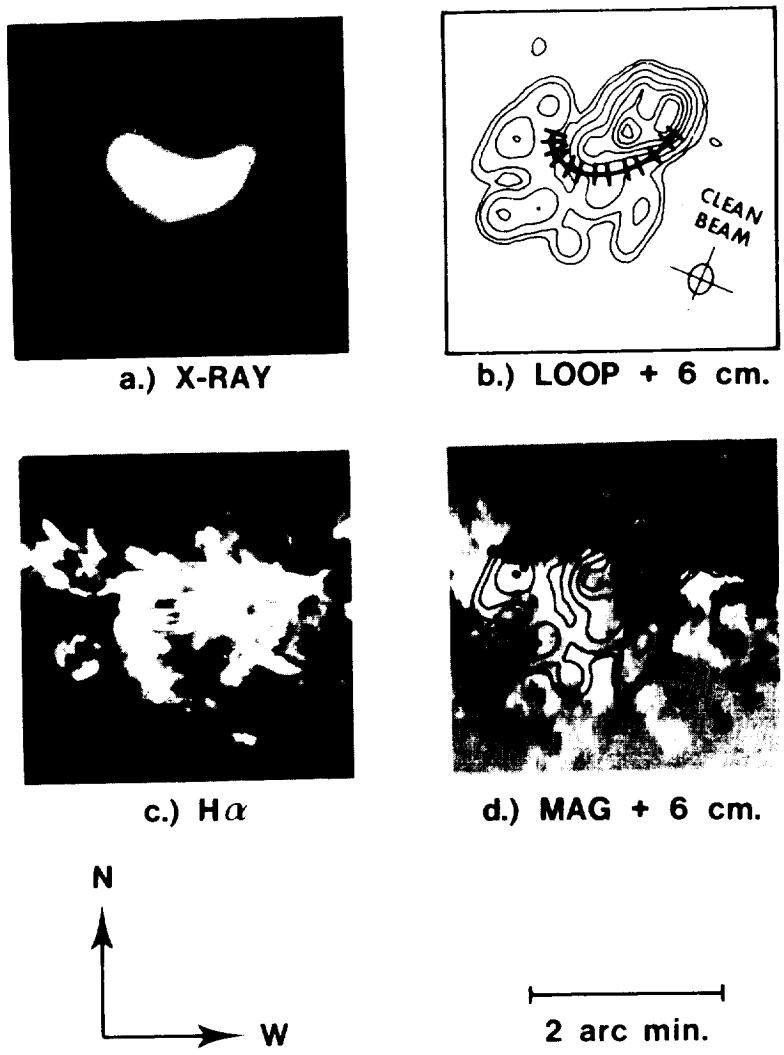

Fig. 1. (a) Deconvolved soft X-ray image of flaring loops in Hale plage region 16413 at 20:52 UT on 7 November, 1979. The original image was obtained on SO-212 film through a 1 micron polypropylene filter with a passband of 8–39, 44–64 Å. (b) Axis of the X-ray loop with every 15° positions of angle α indicated. 6 cm brightness temperature contours are superimposed. The temperature of the lowest contour is 10^6 K with successively higher contours separated by levels of 10^6 K. The radio map is an integration over 20:50–20:55 UT. The 6 cm beam resolution is shown; the long axis lies along celestial N–S. (c) Simultaneous Hα image from the Holloman SOON station. (d) KPNO magnetogram at 19:18 UT with the superimposed 6 cm contours. All images are aligned to within ~10 arc sec.

Synthesized maps of total intensity were obtained of a field of view of 7.2 × 7.2 arc min with a synthesized beam of 19 arc sec by 15 arc sec. The observing procedure, calibration, and cleaning methods were similar to those discussed by Kundu and Velusamy (1980).

2.3. Chromospheric and photospheric data

Hale Region 16413 was a new active region first observed near the east limb at S 15 on 3 November. Over the next several days the plage grew in area and intensity, reaching an area of 5000 millionths of a solar hemisphere on 7 November (*Solar-Geophysical Data*, 1980). Over this same period, the magnetic configuration became more complex; on 7 November it was a bipolar group with a delta configuration and peak fields exceeding 2000 G. This region was the brightest feature on the Sun in the 2.0 cm La Posta daily map.

A 1B Hα flare occurred in region 16413 at S 13 E 22 beginning at approximately 20 : 00 UT with a maximum at ~20 : 34 UT. The associated GOES 1–8 Å X-ray flare reached a peak flux density of 3×10^{-5} W m^{-2} (M3) at about the same time. By 20 : 52 UT, the time of the observations reported here, the 1–8 Å flux density had declined to 1×10^{-5} W m^{-2} (M1). The 2.8 GHz Ottawa burst reported for this event was a gradual rise and fall burst with a peak flux of 14 sfu at 20 : 38 UT. The Hα image from the Holloman Solar Optical Observatory Network (SOON) station is shown in Figure 1 along with the Kitt Peak National Observatory (KPNO) magnetogram obtained that day. The position of the Hα image and magnetogram relative to the 6 cm map was found by converting the solar positions of the sunspots to celestial coordinates and matching those with the radio map. The X-ray, Hα, and magnetogram images were aligned using sunspots as an intermediary. The resulting Hα and X-ray images, magnetogram, and radio map are all aligned to within about 10 arc sec.

2.4. Comparison of the X-ray and microwave data

The images of Figure 1 show that the peak of the 6 cm emission is displaced from the X-ray loop by about 20 arc sec. It appears to be associated with a lower-lying compact Hα flare region on the magnetic inversion line. The earlier radio maps near the peak of the event also show that the centroid of the emitting region coincides with the peak of Figure 1. The peak 6 cm region appears to have no well defined X-ray counterpart although the region is not devoid of X-ray emission. Unfortunately, lack of a well defined X-ray structure has precluded a detailed analysis of that feature. Our interest here is in using the plasma parameters deduced for the X-ray loop to determine the mechanism of the 6 cm radiation from the loop. There are three generally accepted candidate mechanisms: (1) thermal bremsstrahlung; (2) thermal gyroresonance emission; and (3) nonthermal gyrosynchrotron emission.

The length of the X-ray loop is about 80 arc sec, measured linearly between the footpoints while its diameter varies between ~35–45 arc sec, depending upon where it is measured. The longest dimensions of the Hα flare regions at each footpoint of the loop are ~35–45 arc sec. Since these are in agreement with the X-ray observations, we have used an average diameter of 40 arc sec. The temperature distribution of the X-ray loop is confined to the narrow range $T_e \approx 6.5$–8.5×10^6 K. The temperature of the top of the loop averaged over an area 57 arc sec along the loop by 34 arc sec across the loop is $T_e = 8.2 \pm 0.2 \times 10^6$ K and for the larger region of 120 arc sec by 80 arc sec, encom-

passing the entire loop and surrounding area, is $T_e = 7.6 \pm 0.3 \times 10^6$ K. The peak linear emission integral along the line of sight near the axis of the loop is $\int n_e^2 \, dl = 1.4 \times 10^{29} \text{ cm}^{-5}$. For a loop thickness of $l = 40$ arc sec $\approx 3 \times 10^9$ cm, $n_e = 7 \times 10^9 \text{ cm}^{-3}$.

To estimate the importance of thermal bremsstrahlung to the radio emission, we first calculate the optical depth at 6 cm using the derived X-ray parameters in the equation from Kundu (1965),

$$\tau_x = \frac{0.16}{\nu^2 T_e^{3/2}} \int n_e^2 \, dl, \tag{1}$$

where ν is the frequency of the radio observations. For $\int n_e^2 \, dl = 1.4 \times 10^{29} \text{ cm}^{-5}$, $\nu = 5.0$ GHz, and a lower limit of $T_e = 6 \times 10^6$ K, we get an upper limit of $\tau_x = 6.1 \times 10^{-2}$. Therefore, for these conditions the corona is optically thin and $T_b = \tau_x T_e = 3.7 \times 10^5$ K. This value is about an order of magnitude less than the observed values along the loop. Thermal bremsstrahlung may therefore make a small contribution to the observed T_b, but it cannot be the dominant emitting mechanism.

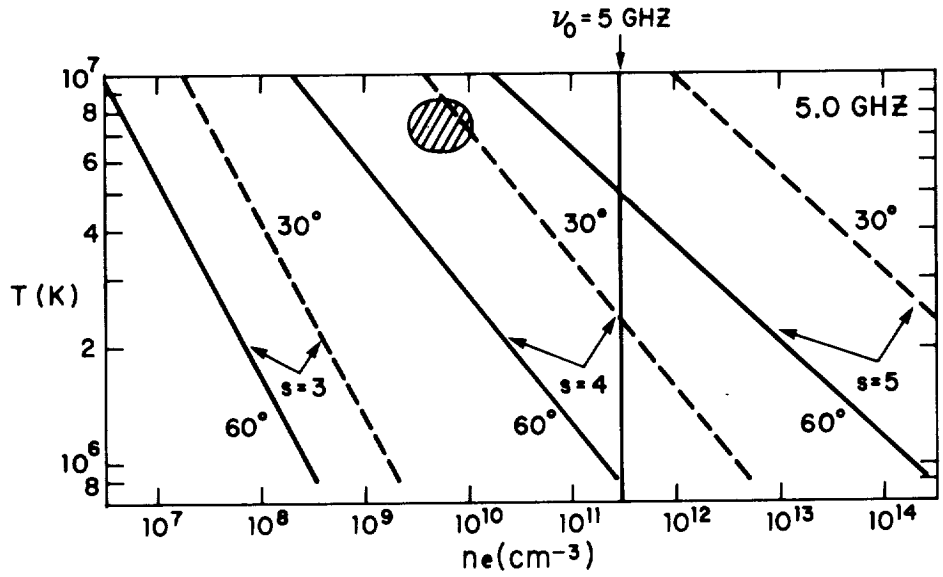

Fig. 2. Loop electron densities and thermal temperatures required to achieve an optical depth of unity in the extraordinary modes of the $s = 3$, 4, and 5 resonant harmonics of the gyrofrequency. The assumed frequency is 5.0 GHz (6 cm) and the e-folding length of the magnetic field magnitude is 10^9 cm. The optical depth scales linearly with both this length and with n_e, being less than unity to the left and greater than unity to the right of each curve. Dashed and solid lines show unity optical depths for values of θ, the angle between the magnetic field and the line of sight, equal to 30° and 60°. The magnetic field intensities required for each harmonic are 600 G for $s = 3$, 450 G for $s = 4$, and 360 G for $s = 5$. Vertical line indicates the density corresponding to the plasma frequency of 5.0 GHz, to the right of which wave propagation does not occur. The shaded oval corresponds to the range of X-ray loop parameters deduced for the 7 November, 1979 flare. After Kundu *et al.* (1980).

Another obvious candidate for the 6 cm emission mechanism is thermal emission due to the enhanced absorption at low harmonics of the gyrofrequency ν_H. Following Kundu *et al.* (1980), we show in Figure 2 the loop densities and temperatures required to achieve an optical depth of $\tau = 1$. We assume, as they did, an e-folding length of 10^9 cm for the magnetic field scale length. For the density and temperature range characteristic of the X-ray loop (shown by the shaded oval) we see that only the fourth and fifth ($s = 4, 5$) harmonics are viable emission mechanism candidates to produce $\tau \leq 1$. These harmonics require magnetic fields of 450 and 360 G, respectively, which do not seem unreasonable in view of the fact that the loop footpoints are in the vicinity of the strong spot fields of the active region.

The optical depth due to gyroresonance absorption is a strong function of θ, the angle between the magnetic field direction and the line of sight. Using the expression for the absorption coefficient of the extraordinary mode and the e-folding thickness of the resonance region of 10^9 cm given by Takakura and Scalise (1970) and by Kundu *et al.* (1980), we have

$$\tau_{res} = 0.030 \Phi n_e \left(\frac{2kT_e}{m_0 c^2}\right)^{s-1} (\sin\theta)^{2s-2}(c_1 + c_2 \cos\theta) \frac{l}{\nu_H}, \qquad (2)$$

where $\Phi = 10.7$ and 63.6 for $s = 4$ and 5, $\nu_H = s^{-1} \times 5.0$ GHz, l is the scale length of the magnetic field, and c_1 and c_2 are functions of s and θ given explicitly in Takakura

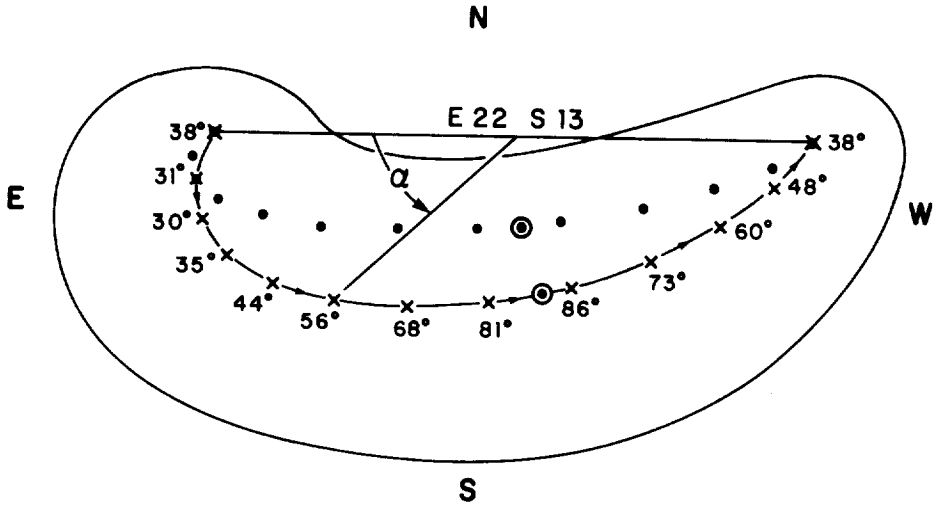

Fig. 3. Schematic model of the X-ray flare loop shown in Figure 1(a). The flare center is taken as E 22 S 13 on the solar disk, but with the loop endpoints assumed to lie in an east-west direction. Curved line is the semicircular loop axis projected onto the plane of the sky with crosses at every 15° increment of α, the angle subtended to the axis of the loop by the arc length, increasing westward from the eastern footpoint. The angle given at each cross is that of θ, the angle between the magnetic field direction and the line of sight. The plane of the loop lies 32° south of the line of sight. A similar semicircular loop lying in a plane in the local solar vertical is shown by the dots; this gave a poor match to the observed loop perspective and was not used. Points with circles indicate positions where $\theta = 90°$ for each loop. The outer line shows approximate outline of loop edges for loop diameter of 40 arc sec or $\sim 3 \times 10^9$ cm.

and Scalise (1970). We can use Equation (2) to calculate τ_{res} for $s = 4$ or 5 at any part of the loop by using the values of n_e and T_e derived from the X-ray observations, assuming an l consistent with those observations, and knowing θ.

In order to find θ at points along the axis of the loop, we have modelled the X-ray loop as a simple semicircular structure as shown in projection in Figure 3. Since the flare position was E 22, we assume a 22° angle between the line of sight and the meridional plane bisecting the loop. The flare was 13° south of the solar equator, which places it about 17° south of the Sun–Earth line. We assumed the loop plane to project radially from Sun center and then calculated the shape of the projected loop axis shown by the dots of Figure 3. The ratio of the projected loop height to the projected loop length was far too small to match the values observed for the X-ray loop. A good match was achieved by letting the plane of the loop be 32° south of the plane containing the Earth–Sun line, which means the loop plane lay 15° south of the local solar vertical. The angle α is defined by the eastern footpoint, the center of curvature of the loop and the point of interest along the loop. Assuming the B field parallel to the loop axis, we have calculated the corresponding values of θ and τ_{res} for 15° increments in α and plotted them in Figure 4. A value of $l = 10^9$ cm, about one third of the apparent loop diameter derived from the X-ray measurement was used. The measured X-ray temperature was used at each point, and $n_e = 7 \times 10^9$ cm^{-3} was assumed for all points. It is known (Kundu, 1965) that the quasi-longitudinal approximation used here is only valid for $\sin^4\theta \ll 4s^2\cos^2\theta$, which limits θ to values less than $\sim 80°$. A substantial decrease in τ is expected at $\theta > 80°$, the region between the dashed lines in Figure 4 (Holman, private communication). With increasing α, θ would become greater than 90° on the west side of the loop, but we have assumed a polarization change and use $\theta = 180° - \theta$ for the extraordinary mode calculation in that region. The 6 cm polarization maps obtained at the VLA were too noisy to be used as a test of this assumption.

The observed 6 cm optical depths along the loop axis derived from the radio brightness temperature maps using $T_b = T_e\,(1 - e^{-\tau})$ are compared with the calculated gyroresonance optical depths in Figure 4. The $s = 5$ optical depths are in fair agreement with the observed values for large angles near the loop top, and the $s = 4$ depths are in fair agreement near the footpoints, but neither individual curve matches the relatively flat distribution of τ with θ over the entire loop. Qualitatively, it is conceivable that the loop magnetic field intensity could be around 450 G at the footpoints, decreasing to around 360 G at the top in just such a way that the sum of the $s = 4$ and $s = 5$ tunately, the photospheric magnetic field observations were severely degraded due to poor observing conditions, so that no quantitative estimates of the magnetic field intensity along the loop could be made. In addition, since the assumed value of l could be in error by a factor of 3 or more, this scenario seems unlikely.

The comparisons of Figure 4 are further limited by our lack of detailed knowledge of the topology of the loop magnetic field. If the ratio of the loop height to the distance between footpoints is larger or smaller than assumed, the range of θ will be somewhat larger or smaller, respectively, than that shown in Figure 4. However, a lower assumed loop height would require that the plane of the loop be inclined at more than 15° to the

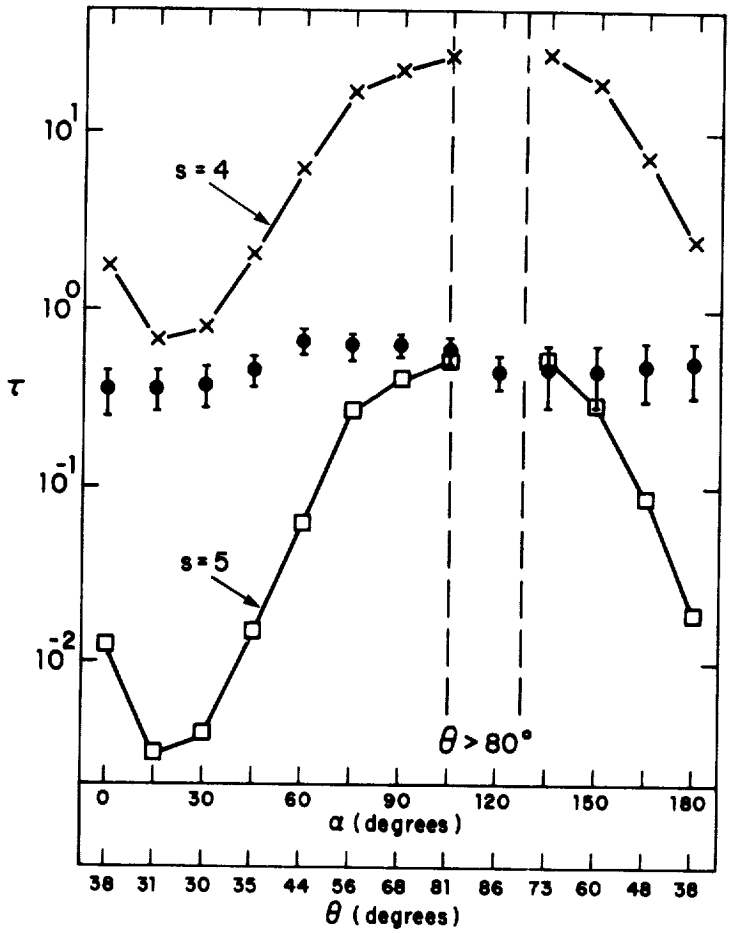

Fig. 4. Crosses and squares show optical depth τ calculated for the fourth and fifth harmonics of the gyrofrequency as a function of both α and θ for the loop model of Figure 3. The quasi-longitudinal approximation is not valid for $\theta \geq 80°$, the region between the dashed lines; a drop in τ is expected there. A density of $n_e = 7 \times 10^9$ cm^{-3} and a magnetic field scale length of $l = 10^9$ cm was assumed for 5.0 GHz; temperatures were then calculated from X-ray measurements for each point along the loop. Filled circles show the values of τ deduced from the measured radio brightness temperatures at corresponding points along the loop.

local solar vertical direction. Another possibility is that the loop field lines are helical, rather than parallel to the loop axis. If so, a range of θ would be associated with each angle α of Figure 4, resulting in a flatter distribution of τ with θ. We calculate that an angle of about 40° between an azimuthal field component B_ϕ and the longitudinal component B_z, both assumed constant throughout the loop, will result in fair agreement between the $s = 5$ curve and the observed values of τ shown in Figure 4. For example, in this case the values of τ at $\theta = 30°$ and 40° are 0.13 and 0.21, respectively, which are only slightly lower than the observed values. Furthermore, the lack of any drop in

τ for $\theta > 80°$ is also expected in this model. Because the observed loop is thick, with $L/a = 4$, where a is the loop radius and L the loop length, the threshold for the external kink instability (Spicer and Brown, 1981)

$$B_\phi^2 \ln(L/a) > B_z^2 \tag{3}$$

is not satisfied, and the loop is stable. A similar range of θ might also result from a spreading of the cross section of the loop with height, particularly near the footpoints. Thus we see that the assumption of large azimuthal or radial field components can result in much better agreement between the observed and calculated values of τ than that shown in Figure 4.

A final candidate to explain the optical depth of at least part of the loop is gyrosynchrotron emission. Petrosian (1982) has modelled the gyrosynchrotron emission expected from a flaring semicircular magnetic loop similar to our model shown in Figure 3. For loops near the center of the solar disk his uniform trap model, in which the magnetic field is nearly uniform and the electron pitch angle distribution isotropic, yields maximum microwave emission near the loop top and a minimum at the footpoints. In his nonuniform trap model, in which the magnetic field intensity decreases rapidly with height and the pitch angle distribution is broadest at the footpoints, the strongest emission arises from the footpoints. The uniform trap model was preferred to account for the observations (cf., Kundu *et al.*, 1982) of the impulsive phase peak flare emission at the tops of loops, but in our case, if gyroresonance absorption from either the $s = 4$ or $s = 5$ harmonic is effective at the loop top as shown in Figure 4, the nonuniform trap model better fits the data.

Any nonthermal electrons responsible for the 6 cm emission observed at 20 : 52 UT cannot have been accelerated tens of minutes earlier near the flare maximum. Using the equation of Kundu and Vlahos (1982) for the collisional deflection time of energetic electrons,

$$\tau_D = 2 \times 10^8 \, E^{3/2} \, (\text{keV}) \, n_e^{-1} \, \text{s} \, , \tag{4}$$

we find that τ_D is only 30 s for the derived loop density and for $E = 100$ keV electrons. Thus, the gyrosynchrotron explanation for the 6 cm emission from the X-ray loop requires continuous or continual acceleration of electrons of $E \geq 100$ keV, the energy range required for microwave gyrosynchrotron emission (Takakura, 1972).

3. Discussion and Conclusion

We have used the plasma parameters deduced from X-ray observations to infer the 6 cm radiation mechanisms of the bright flare loop in its decay phase. The apparently simple geometry of the X-ray loop has allowed us to test gyroresonance absorption theory using a semicircular loop model to look for the strong dependence of τ on θ. Earlier studies (e.g., Schmahl *et al.*, 1982) had invoked gyroresonance harmonics only as high as the fourth ($s = 4$) to explain the 6 cm emission from active regions, but in our study the large values of T_e and n_e combined with the low 6 cm values of τ have made $s = 5$ harmonic

emission a possibility. For a uniform axial field we find that no single gyroresonance harmonic can account for the relatively flat distribution of τ vs θ, but an unlikely combination of the $s = 5$ harmonic at the top of the loop and the $s = 4$ harmonic at the loop footpoints is consistent with the observations. Magnetic fields in the range of 360 to 450 G are required for these harmonics. We also investigated the effect of non-parallel field distributions on the gyroresonance model and find that azimuthal or radial field components at an angle of about 40° to the axial field can explain the observations.

We also investigated qualitatively gyrosynchrotron emission from nonthermal electrons to explain the 6 cm emission mechanism along at least the lower part of the loop. Gyrosynchrotron emission as an alternative to thermal gyroradiation had earlier been suggested by Velusamy and Kundu (1981) as the radiation mechanism for 20 cm postflare loops they observed with the VLA. They used the ≥ 2.5 hr lifetime of the observed burst to infer the loop magnetic field strength on the assumption that this lifetime was the radiative decay time of mildly relativistic electrons. Their calculation is valid, however, only if the radiative loss time is shorter than the collisional loss time, which, in their case, requires $n_e \leq 10^8$ cm^{-3}. This condition is definitely not fulfilled in our case, where $n_e \sim 7 \times 10^9$ cm^{-3}. Thus if the 6 cm emission is nonthermal, it must be from newly accelerated electrons and not from electrons surviving from the earlier flare maximum.

Nonthermal emission has also been suggested for some 6 cm quiescent active region loops by Webb *et al.* (1983). In their case the 6 cm components were not associated with any X-ray emission. The low temperatures and/or densities inferred from the X-ray observations permitted only low harmonics ($s = 2$ or 3) with their associated unrealistically large magnetic fields (900 or 600 G, respectively) as acceptable gyroresonance absorption mechanisms. Schmahl *et al.* (1982), faced with essentially the same dilemma in a similar study, suggested localized current systems to enhance the coronal magnetic fields and retain the gyroresonance mechanism. In our case the fifth harmonic of gyroresonance emission requires a field of only 360 G, which is not unreasonable in view of the presumed strong fields of the flare region. We find that such thermal emission can explain the observations over the whole loop only if there are rather large azimuthal or radial field components. Alternatively, the gyrosynchrotron hypothesis can account, at least in part, for the observations if a continuous supply of energetic electrons is available. We conclude that one or a combination of these mechanisms is the likely source of the microwave emission, but that we cannot choose among them because of our poor knowledge of the loop magnetic field.

This lack of more detailed knowledge of the loop magnetic field intensity and geometry has been a serious obstacle in our effort to assess the role of gyroresonance emission as the 6 cm radiation mechanism. Although the X-ray loop was large, with fairly uniform brightness and well determined longitudinal temperature and density distributions, important assumptions about the shape and orientation of the loop and the helicity and scale length of the magnetic field were required to calculate the gyroresonance optical depth. We find that models based on either gyroresonance or gyrosynchrotron mechanisms can be made to fit the observations by a suitable choice

of poorly known parameters. Complete microwave polarization and multi-frequency observations are required to better infer the coronal magnetic field. Future tests of gyroresonance theory will benefit greatly from a combination of such high-resolution microwave observations and X-ray and photospheric magnetogram images, and should allow us to confirm or elimitate one of these mechanisms from consideration.

Acknowledgements

We are grateful to J. Harvey of KPNO for providing the magnetogram and white-light images and to D. Rust for the Holloman Hα film. We acknowledge the useful comments of the referee and helpful discussions with E. Schmahl and G. Holman about gyroresonance absorption. The work at AS & E was supported by NASA contracts NAS5-25496 and NASW-3586. SWK thanks M. Shea of AFGL for her generous support. The work of MRK at the University of Maryland was supported by NASA contract NSG 5320, NASA grant NGR 21-002-199 and NSF grant ATM 81-03089.

References

Alissandrakis, C. E., Kundu, M. R., and Lantos, P.: 1980, *Astron. Astrophys.* **82**, 30.
Chiuderi-Drago, F., Bandiera, R., Falciani, R., Antonucci, E., Lang, K. R., Willson, R. F., Shibasaki, K., and Slottje, C.: 1982, *Solar Phys.* **80**, 71.
Felli, M., Lang, K. R., and Willson, R. F.: 1981, *Astrophys. J.* **247**, 325.
Kundu, M. R.: 1965, *Solar Radio Astronomy*, Interscience, New York.
Kundu, M. R.: 1982, *Rep. Prog. Phys.* **45**, 1435.
Kundu, M. R. and Velusamy, T.: 1980, *Astrophys. J.* **240**, L63.
Kundu, M. R. and Vlahos, L.: 1982, *Space Sci. Rev.* **32**, 405.
Kundu, M. R., Alissandrakis, C. E., Bregman, J. D., and Hin, A. C.: 1977, *Astrophys. J.* **213**, 278.
Kundu, M. R., Schmahl, E. J., and Gerassimenko, M.: 1980, *Astron. Astrophys.* **82**, 265; Erratum, 1980, *Astron. Astrophys.* **91**, 377.
Kundu, M. R., Schmahl, E. J., and Velusamy, T.: 1982, *Astrophys. J.* **253**, 963.
Lang, K. R., Willson, R. F., and Gaizauskas, V.: 1983, *Astrophys. J.* **267**, 455.
Petrosian, V.: 1982, *Astrophys. J.* **255**, L85.
Schmahl, E. J., Kundu, M. R., Strong, K. T., Bentley, R. D., Smith, J. B., Jr., and Krall, K. R.: 1982, *Solar Phys.* **80**, 233.
Schmahl, E. J., Kundu, M. R., Landecker, P. B., and McKenzie, D. L.: 1983, *Solar Phys.* **83**, 3.
Shibasaki, K., Chiuderi-Drago, F., Melozzi, M., Slottje, C., and Antonucci, E.: 1983, *Solar Phys.* **89**, 307.
Solar-Geophysical Data Bulletins: 1980, published by WDC-A for Solar-Terrestrial Physics, NOAA, Boulder, Colorado, U.S.A.
Spicer, D. S. and Brown, J. C.: 1981, in S. Jordan (ed.), *The Sun as a Star*, NASA SP-450, Washington, D.C., p. 413.
Takakura, T.: 1972, *Solar Phys.* **26**, 151.
Takakura, T. and Scalise, E., Jr.: 1970, *Solar Phys.* **11**, 434.
Vaiana, G. S., Van Speybroeck, L., Zombeck, M. V., Krieger, A. S., Silk, J. K., and Timothy, A.: 1977, *Space Sci. Instr.* **3**, 19.
Velusamy, T. and Kundu, M. R.: 1981, *Astrophys. J.* **243**, L103.
Webb, D. F., Davis, J. M., Kundu, M. R., and Velusamy, T.: 1983, *Solar Phys.* **85**, 267.

4.14 Small-Scale Flux Emergence and the Evolution of Equatorial Coronal Holes

John M. Davis

American Science and Engineering, Inc.
Cambridge, Massachusetts 02139

SMALL-SCALE FLUX EMERGENCE AND THE EVOLUTION OF EQUATORIAL CORONAL HOLES

JOHN M. DAVIS

American Science and Engineering, Inc., Fort Washington, Cambridge, MA 02139, U.S.A.

(Received 18 October, 1982; in final form 4 September, 1984)

Abstract. To study the formation and development of coronal holes, their association with X-ray bright points has been investigated. The areal density of X-ray bright points was measured within the boundaries of coronal holes and was found to increase linearly with time for each of the three, long-lived, equatorial coronal holes of the Skylab era. Analysis of the data shows that the effect is not the result of global changes in bright point number and is therefore a property of the restricted longitude region which contains the coronal hole. The bright point density at the time of the hole's formation was also measured and, although the result is more uncertain, was found to be similar to the bright point number over the solar surface. No association was found between bright points and the rate of change of coronal hole area.

1. Introduction

Coronal holes are regions of exceptionally low density in the inner corona, which have been observed at both soft X-ray and He I 10830 Å wavelengths for over a decade. However, a definitive explanation of their formation and subsequent evolution is still missing. For example, X-ray observations exist for the birth of only a single coronal hole (Solodyna *et al.*, 1977). In this case the hole developed rapidly, i.e., in less than a day and with a growth rate three times faster than the long term average of all holes; a result which is consistent with the He I 10830 Å coronal hole observations (Harvey and Sheeley, 1979). This behavior led Nolte *et al.* (1978a) to conclude that the conditions for coronal hole development are built up over a longer period of time and the actual birth is triggered by an event (or events) which leads to the rapid opening of field lines. This hypothesis is supported by the observations of the photospheric magnetic field beneath the hole which shows little if any change during the period of the hole's rapid growth (Harvey and Sheeley, 1979).

The subsequent development of coronal holes has been linked to the process of random walk diffusion, proposed by Leighton (1964) to explain the transport of surface magnetic fields. This phenomenological description is known generically as the model of locally unbalanced flux (Timothy *et al.*, 1975; Bohlin, 1976; Bohlin and Sheeley, 1978; Broussard *et al.*, 1978). In it the flux from an emerging bipolar magnetic region (BMR) reconnects to opposite but pre-existing flux in its immediate environment. The reconnection results from the separation. through diffusion of the original BMR, and leads to regions of a single polarity with field lines that are open rather than closed.

Observational support for the model was provided by the results of several studies (Timothy *et al.*, 1975; Bohlin, 1977; Nolte *et al.*, 1978a) which measured the areal growth and decay rates of coronal holes. They found that on average $(dA/dt)_{ch}$ is

Solar Physics **95** (1985) 73–82. 0038–0938/85/0951–0073$01.50.

approximately 1.5×10^4 km^2 s^{-1}. In Leighton's (1964) model for the transport of surface magnetic fields, this rate can be related to the diffusion coefficient, D, through the equation (Mosher, 1977)

$$D = \frac{1}{4}\frac{L^2}{t} = \frac{1}{4\pi}\left(\frac{dA}{dt}\right),$$

where L^2 is the mean square displacement over the time interval t. The coronal hole measurements lead to a value for D of 1.2×10^3 km^2 s^{-1} which, although somewhat larger, is still consistent with Leighton's value of 800 km^2 s^{-1}. However, Mosher (1977), who repeated Leighton's analysis using more recent observations and analytical techniques, concluded that the most probable value of D is of order 200 km^2 s^{-1} and that values as high as 1000 km^2 s^{-1} can definitely be excluded. Thus the coronal hole observations join the growing body of evidence, e.g., measurements of the supergranule velocity fields (Worden and Simon, 1976) and the background and large-scale magnetic fields (Stenflo, 1976; Howard and LaBonte, 1981; Topka *et al.*, 1982) which cast doubt on the general applicability of the random walk process to the transport of surface fields.

Sheeley and Harvey (1981) have interpreted their most recent He I 10830 Å observations of mid-latitude holes in terms of their diffusion and regeneration by the organizing action of differential rotation. While their model still retains random walk diffusion as the basic mechanism, apparent growth rates which differ from the canonical value can be explained. However, differential rotation as an organizing force has obvious limitations when applied to the equatorial coronal holes whose boundaries rotate rigidly (Timothy *et al.*, 1975; Wagner, 1975).

An alternative approach would be to supplement the Leighton mechanism by adopting the suggestion of Marsh (1978). He showed that the interaction of ephemeral regions (*ER*) with elements of the supergranulation network could increase the apparent rate of magnetic diffusion, measured over large scales, by superposing large discrete changes upon the random walk mechanism. The changes have the characteristic length of the *ER* pole separation and by integrating over their observed size spectrum Marsh obtained a value for D of 830 km^2 s^{-1}. This is close to the value required to explain coronal hole growth and therefore *ER*s might be expected to play a role in their development.

Inspection of the X-ray images of the Skylab coronal holes (see, e.g., Zombeck *et al.*, 1978) suggests that coronal holes are formed with few X-ray bright points (XBP), the X-ray analogue of an ephemeral region, within their boundaries but that their number increases on successive appearances of the hole. To quantify this impression and to amplify our knowledge of the formation and development of coronal holes, we have sought answers to the following questions. (1) Is the evolution of coronal holes accompanied by an increase in the bright point areal density? (2) Do coronal holes form in regions where the bright point areal density is enhanced? (3) Is the bright point areal density related to changes in the growth and/or decay of coronal holes?

2. Analysis and Results

X-ray bright points (XBPs) are tracers of the emergence patterns of small scale activity. They are clearly identified, discrete sites of emerging magnetic flux with a relatively high frequency of occurrence. They possess two other characteristics which are important for a statistical study; namely, they are shortlived with a mean lifetime of 8 hr and they possess a wide latitude distribution which is not restricted to the active region zone (Golub *et al.*, 1974). Although a more detailed analysis of the observations suggest that their latitude distribution during the period of the Skylab studies was bimodal (Golub *et al.*, 1975), the current study is restricted to the near-equatorial latitudes over which their distribution is approximately flat. Consequently, it was not considered necessary to correct for non-uniformities in the bright point latitude distribution and an equal weight is attributed to the occurrence of an XBP anywhere within a coronal hole.

The coronal hole set used for the study is based on the Skylab atlas prepared by Nolte *et al.* (1976). Six X-ray holes were identified. Of these two have been excluded from the following analysis because they document only the final stages of the hole's existence. The excluded holes are, in the standard nomenclature, CH5, which was observed only during the first rotation, and CH3. The latter, although visible on three rotations, appeared as a badly fragmented extension of the northern polar hole which is consistent with its identification by Timothy *et al.* (1975), using Fe XV observations, as the remnant of a hole formed at least seven rotations before being observed from Skylab. Of the remaining holes CH1 also connects, at times, to the northern polar hole. When this occurs the measurements have been restricted to latitudes below 40 N. The restriction is designed to remove any influence that the northern polar hole, which was a continuous but evolving feature during the Skylab period (Bohlin, 1977; Sheeley, 1980), may have on the data.

To maximize the statistics of each XBP observation, the longest exposure (256 s) through the long wavelength filter (3–32; 43–54 Å bandpass) was used to count the bright points. In the following analysis these numbers will be compared with a global bright point average based on the statistics of Golub *et al.* (1976) which reflect the number of XBPs observed on a 4 s exposure. Different exposures are used because of the difference in visibility of bright points when observed against backgrounds of either the weakly emitting, large scale structure or emissionless, coronal holes. To remove any bias introduced by the background, bright points are generally counted using an exposure which is short enough to suppress the emission from the large scale structure and which for the Skylab instrument was 4 s. This of course reduces the number of XBPs which are observed and increases the statistical uncertainty in any single observation.

In this study we are counting bright points *only* in coronal holes where the obscuration is negligible and are therefore free to use the longest available exposure to maximize the number of counts and minimize the statistical variations. When the two data sets are compared the observations have been normalized following the procedure of Golub *et al.* (1974). They demonstrated that as the exposure was lengthened the

number of XBP observed increased, asymptotically approaching a value ten times that on a 4 s exposure at 256 s. This result suggests that all XBPs belong to the same size distribution and that at the longest exposure all the bright points are being seen. Therefore the numbers of bright points observed on the 256 s exposures should be the total number. The numerical values of bright point areal density quoted in this paper will always refer to this total number. When comparisons are made, the bright point averages of Golub *et al.* (1976) have been normalized to correspond to the same total number.

The simplest procedure for our study would be to straightforwardly count the numbers of XBPs within each hole. However, since the area of each hole changes considerably from one rotation to the next, we have instead determined the number of bright points per unit area. This areal density has been obtained by measuring both the area of the coronal hole and the average number of XBPs it contains at central meridian passage. To improve the precision of the areal measurements an average coronal hole area was derived from nine observations made at approximately 12-hr intervals between $\pm$ 48 hr of CMP, when suitable images were available. The bright point average was based on five counts made over the same period but at 24 rather than 12-hr intervals to allow the points in the earlier sample to decay below the visibility threshold. The longer interval between observations is necessary because the bright point lifetime is a function of the exposure and increases to 15 hr at 256 s. The 24-hr interval between bright point counts was chosen as a compromise between the need to obtain as many measurements as possible but to have the measurements statistically independent.

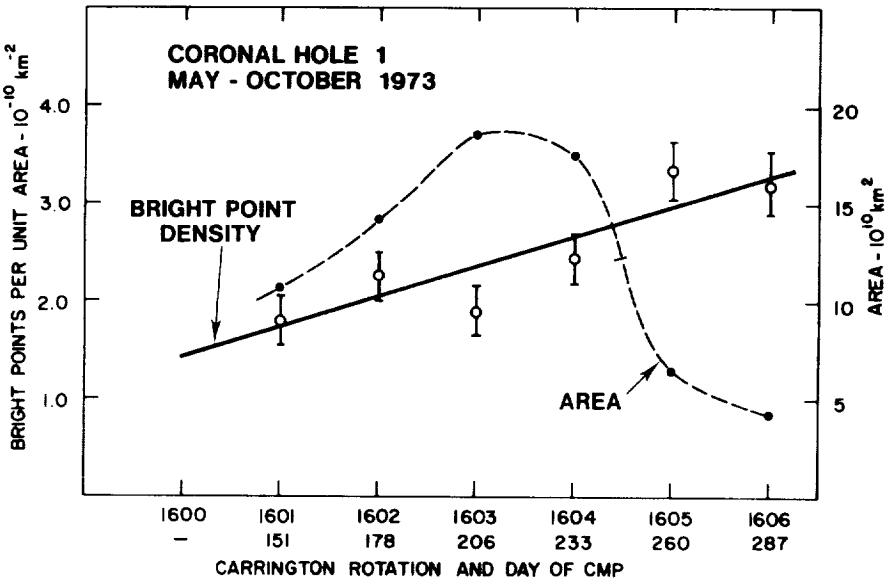

Fig. 1. The variation with time of the X-ray bright point areal density, within CH1. The solid line is a least squares fit to the data points which were measured at successive CMPs. The area of the coronal hole is shown by the broken line.

Of the questions posed in the introduction, the first, namely, whether there exists an increase in the bright point areal density within coronal holes as a function of time, is most easily answered. CH1 was investigated first and the results are shown in Figure 1. The open circles show the bright point areal density measured at each central meridian passage; the error bars represent only the statistical uncertainty in the number of points. Over the six-month interval the bright point density shows a steady increase with no apparent correlation with either the area of the hole, which varies considerably from rotation to rotation (broken line), or its rate of change. A least squares fit to the XBP data produces the solid line shown which has a correlation coefficient of 0.88.

Of the remaining holes in the data set, two, CH2, and CH4, last for more than 3 rotations. The same analysis was applied to these holes and produced similar results (Figure 2 and 3). In all three cases as the hole evolves, the bright point areal density, and therefore the rate of new flux emergence increases linearly, reaching several times its initial value before the coronal hole loses its identity.

The initial density and rate of increase for the four measured holes are summarized in Table I. The first observation of CH1 had a measured areal density of 1.6×10^{-10} km^{-2}. However, CH1 had existed for at least two rotations before it was observed by Skylab (Bohlin, 1977). Using the least squares fit to extrapolate over these two rotations, we obtain an estimated value of 1.16×10^{-10} km^{-2} for the initial density. For CH6, which was the only hole to actually be observed forming on the disk, the initial density, which is the highest of the four, is the average value measured over the first three days of its existence.

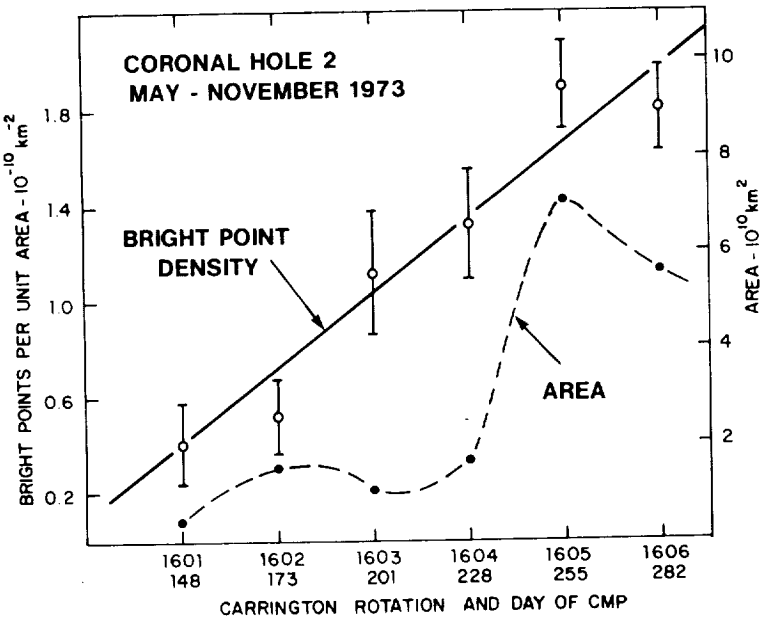

Fig. 2. The temporal variation of the bright point areal density and coronal hole area for CH2 in the same format as Figure 1.

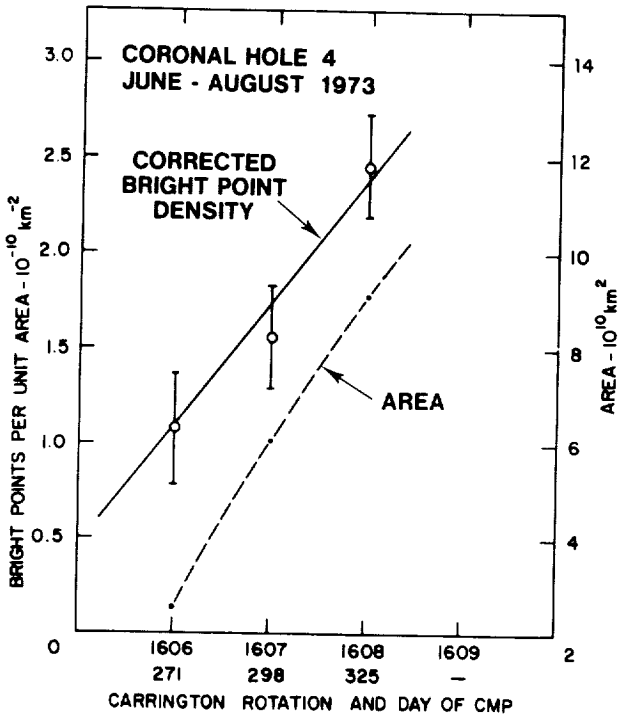

Fig. 3. The temporal variation of the bright point areal density and coronal hole area for CH4. The data points have been corrected by subtracting the globally averaged density from the values measured within the coronal hole.

TABLE I

X-ray bright point data

Coronal hole identification	Bright point density XBP km^{-2}		Rate of increase XBP day^{-1} km^{-2}
	Initial	Global average	
CH1*	1.16×10^{-10}	0.90×10^{-10}	1.14×10^{-12}
CH2	0.41×10^{-10}	0.95×10^{-10}	1.17×10^{-12}
CH4	1.43×10^{-10}	1.14×10^{-10}	1.67×10^{-12}
CH6	1.65×10^{-10}	1.61×10^{-10}	–
Mean	$1.16 \pm 0.54 \times 10^{-10}$	$1.15 \pm 0.32 \times 10^{-10}$	$1.33 \pm 0.30 \times 10^{-12}$

* Values for CH1 have been extrapolated back two rotations.

To determine whether holes form in regions which are characterized by an enhanced bright point areal density, it is necessary to establish a global average for use as a baseline against which the initial densities can be compared. During Skylab the number of bright points on the Sun at any instant of time ranged from 400 ± 90 to 1200 ± 160 (Golub

et al., 1976). The average is usually taken as 500 corresponding to an areal density of 8.3×10^{-11} km^{-2}. However, the bright point statistics suggest an excess within the equatorial latitudes (Golub *et al.*, 1975). The excess is such that two thirds of the bright points lie between $\pm 30°$ latitude. Consequently, an average areal density of 1.1×10^{-10} km^{-2} is more appropriate for the region containing the equatorial coronal holes.

To compare the data against a single global average is questionable because it makes no allowance for the wide variation in the average bright point number over this period. Therefore, we have attempted to construct a more realistic average which reflects the temporal variation of the bright point density and allows one to assign a value to the density existing at the actual time of the formation of the coronal hole. Since the individual observations are restricted to a single hemisphere, the global average has been calculated in the form of a 360-degree running mean using the data set of Golub *et al.* (1976). They compiled averages of XBP observed between latitudes 30° N and 30° S in 10° longitude intervals on 4 s exposures. The data have been normalized as described earlier and a 36-point or 360° running average computed. The eight-month curve is reproduced in Figure 4. Each point is centered on the position of the CMP of the particular Carrington longitude interval and the data are displayed as number per unit area so that they can be compared directly with the results from the earlier analyses. It can be seen that the temporal variation is aperiodic with a magnitude ranging between 0.72×10^{-10} km^{-2} to 1.71×10^{-10} km^{-2}. There are at least two distinct episodes of enhanced bright point emergence; however, the central meridian passages of the coronal holes appear to fall randomly across the distribution.

Comparison of the initial bright point density with the corresponding global average (Table I) shows that they are essentially identical, and one concludes that there is no evidence for coronal hole formation in regions where the small scale flux emergence is either enhanced or reduced. This conclusion is based, however, on only four data points

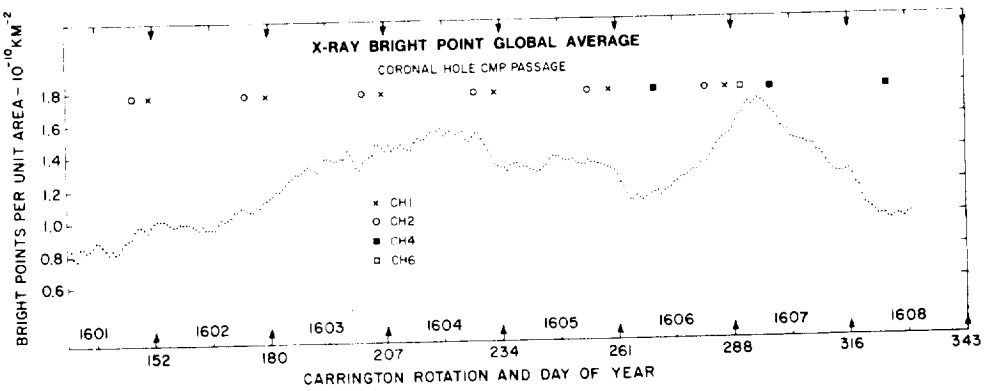

Fig. 4. The variation of the global bright point density with time for the period of the Skylab mission (May–November 1973). The curve is a 360° running average of the bright points counted between latitudes 30 N and 30 S and normalized to include all the points visible on the longest X-ray exposure (256 s). The CMPs of the four coronal holes are indicated.

of which one point (CH1) is based upon a linear extrapolation of the data. The validity of this extrapolation is open to question, since the detailed behavior of the XBP distribution prior to 28 May, 1973 is unknown, with one exception. The exception was a rocket flight which occurred on 8 March, 1973 (Davis and Krieger, 1982) precisely three rotations (81 days) before the first observed CMP of CH1. The corresponding global bright point density for this observation was 0.95×10^{-10} km^{-2} which is similar to the density observed at the start of the Skylab period. Therefore the data are consistent with a constant level of XBP emergence over this period, which justifies the use of the extrapolation.

Finally, by subtracting the global background evaluated at the time of the coronal hole's CMP, a set of points are obtained which give the density excess above the global average. These points can be used to repeat the evolutionary study of the areal density. Apart from an offset, neither the corrected points nor the slopes of the fitted lines exhibit any but minor differences when compared to the original data (Figure 3). This implies that a global variation can be ruled out as being responsible for the steady increase in bright point density found within coronal holes.

3. Conclusions

From a study of the association between X-ray bright points and coronal holes, a linear relationship has been discovered between coronal hole evolution and the emergence of small-scale magnetic flux. The relationship has the form of a steady growth in the emergence of the small scale flux which is maintained throughout the hole's life and reaches levels 3 to 4 times the global average before the hole disappears. Our analysis has ruled out global variations in the bright point emergence patterns as an explanation of this result, which imples that this is a local property of the longitude region which contains the coronal hole. We also found that the initial appearance of coronal holes with an apparent absence of bright points within their boundaries is misleading. Instead the data indicate that coronal holes are born in regions where the XBP density is not suppressed below the global average. In fact, the data show a very slight excess in the rate at which the magnetic flux is emerging. The first result supports and extends the work of Nolte *et al.* (1978b), who found that the number of XBP located near the boundaries of coronal holes also increased as the hole aged.

In the introduction the need for modifying Leighton's model of random walk diffusion in order to explain the rate of growth of coronal holes was described and Marsh's hypothesis (1978) was identified as a candidate for this role. If his hypothesis is valid, one would expect to find a relationship between bright point density and the rate of change of coronal hole area. To test for the latter a comparison between the long term average rate of change of coronal hole area, defined as the difference in area measured on subsequent rotations, and the areal density was made. A scatter plot constructed from the data from all the holes had a random appearance indicating the poor correlation ($r \sim -0.3$) between the two variables. Before dismissing Marsh's hypothesis we should realize the limitations of the present study. Only time-averaged data have been used, and

the averaging period is long compared to bright point life times. Although the use of long-term averages for studying the rate of change of hole area was justified by Nolte *et al.* (1978a), who found excellent agreement between short (~ 2 days) and long-term rates of change, there may be subtleties which have been missed, for instance, perhaps only bright points close to the boundary influence the growth rate. Unfortunately, the present data are insufficient to test this hypothesis.

To summarize the answers to the three questions posed in the introduction, we have found that the evolution of coronal holes is accompanied by a substantial increase in the bright point density, but this increase is not related to the rates of growth or decay. The statistical evidence provides only weak support for the formation of coronal holes in regions of above normal bright point density. Where it is possible to study the formation of a hole in detail, as in the case of CH6 (see Solodyna *et al.*, 1977, Figure 3), a bright point is present at, or close to, the birth of the hole. This could be a random association, and since the subsequent changes in coronal hole area are not directly coupled to the small-scale flux emergence, our observations suggest that the XBP acts only as the catalyst which triggers the birth of the coronal hole within a larger region, in which the conditions for hole formation have been preset by a systematic, widespread mechanism (Frankenthal and Krieger, 1977; Nolte *et al.*, 1978a).

Acknowledgements

It is a pleasure to acknowledge the many useful discussions held with my colleagues D. Webb and A. Krieger of AS&E since the inception of this project and the assistance of Ms. Jadwiga Zmijewski in the counting of bright points. The author also wishes to thank an anonymous referee for his critical review of the original draft of this paper.

The work has been supported by NASA under contract NAS5–25496.

References

Bohlin, J. D.: 1976, in D. J. Williams (ed.), *Physics of Solar Planetary Environments*, Vol. I, Am. Geophys. Union, p. 114.
Bohlin, J. D.: 1977, *Solar Phys.* **51**, 377.
Bohlin, J. D. and Sheeley, Jr., N. R.: 1978, *Solar Phys.* **56**, 125.
Broussard, R. M., Sheeley, Jr., N. R., Tousey, R., and Underwood, J. H.: 1978, *Solar Phys.* **56**, 161.
Davis, J. M. and Krieger, A. S.: 1982, *Solar Phys.* **80**, 295.
Frankenthal, S. and Krieger, A. S.: 1977, *Solar Phys.* **55**, 83.
Golub, L., Krieger, A. S., Silk, J. K., Timothy, A. F., and Vaiana, G. S.: 1974, *Astrophys. J.* **189**, L93.
Golub, L., Krieger, A. S., and Vaiana, G. S.: 1975, *Solar Phys.* **42**, 131.
Golub, L., Krieger, A. S., and Vaiana, G. S.: 1976, *Solar Phys.* **50**, 311.
Harvey, J. W. and Sheeley, Jr., N. R.: 1979, *Space Sci. Rev.* **23**, 139.
Howard, R. and LaBonte, B. J.: 1981, *Solar Phys.* **74**, 131.
Leighton, R. B.: 1964, *Astrophys. J.* **140**, 1547.
Marsh, K. A.: 1978, *Solar Phys.* **59**, 105.
Mosher, J. M.: 1977, Ph.D. Thesis, California Institute of Technology, Pasadena, California.
Nolte, J. T., Krieger, A. S., Timothy, A. F., Vaiana, G. S., and Zombeck, M. V.: 1976, *Solar Phys.* **46**, 291.
Nolte, J. T., Gerassimenko, M., Krieger, A. S., and Solodyna, C. V.: 1978a, *Solar Phys.* **56**, 153.

Nolte, J. T., Davis, J. M., Gerassimenko, M., Krieger, A. S., Solodyna, C. V., and Golub, L.: 1978b, *Solar Phys.* **60**, 143.
Sheeley, Jr., N. R.: 1980, *Solar Phys.* **65**, 229.
Sheeley, Jr., N. R. and Harvey, J. W.: 1981, *Solar Phys.* **70**, 237.
Solodyna, C. V., Krieger, A. S., and Nolte, J. T.: 1977, *Solar Phys.* **54**, 123.
Stenflo, J. O.: 1976, in V. Bumba and J. Kleczek (eds.), 'Basic Mechanisms of Solar Activity', *IAU Symp.* **71**, 69.
Timothy, A. F., Krieger, A. S., and Vaiana, G. S.: 1975, *Solar Phys.* **42**, 135.
Topka, K., Moore, R., LaBonte, B. J., and Howard, R.: 1982, *Solar Phys.* **79**, 231.
Wagner, W. J.: 1975, *Astrophys. J.* **198**, L141.
Worden, S. P. and Simon, G. W.: 1976, in V. Bumba and J. Kleczek (eds.), *IAU Symp.* **71**, 121.
Zombeck, M. V., Vaiana, G. S., Haggerty, R., Krieger, A. S., Silk, J. K., and Timothy, A.: 1978, *Astrophys. J. Suppl.* **38**, 69.

4.15 The Cyclical Variation of Energy Flux and Photospheric Magnetic Field Strength from Coronal Holes

David F. Webb and John M. Davis

American Science and Engineering, Inc.
Cambridge, Massachusetts 02139

THE CYCLICAL VARIATION OF ENERGY FLUX AND PHOTOSPHERIC MAGNETIC FIELD STRENGTH FROM CORONAL HOLES

DAVID F. WEBB and JOHN M. DAVIS

American Science and Engineering, Inc., Fort Washington, Cambridge, MA 02139, U.S.A.

(Received 5 August, 1985)

Abstract. We measured the average soft X-ray emission from coronal holes observed on images obtained during AS & E rocket flights from 1974 to 1981. The variation of this emission over the solar cycle was then compared with photospheric magnetic flux measurements within coronal holes over the same period. We found that coronal hole soft X-ray emission could be detected and that this emission appeared to increase with the rise of the sunspot cycle from activity minimum to maximum. Our quantitative results confirmed previous suggestions that the coronal brightness contrast between holes and large-scale structure decreased during this period of the cycle. Gas pressures at the hole base were estimated for assumed temperatures and found to vary from about 0.03 dyne cm^{-2} in 1974 to 0.35 dyne cm^{-2} in 1981. The increase in coronal hole X-ray emission was accompanied by a similar trend in the surface magnetic flux of near-equatorial holes between 1975 and 1980 (Harvey *et al.*, 1982).

1. Introduction

Coronal holes were first and most easily identified in soft X-ray and XUV images as regions of very low brightness in comparison to surrounding active regions or other large-scale structures. They were first studied in detail during the Skylab period and their observational characteristics at that phase of the solar cycle were well established. These characteristics included nearly rigid rotation, large, low-latitude extensions of polar holes, near-zero X-ray emission and a strong correlation between the low-latitude portions of holes and high speed solar wind streams (Krieger *et al.*, 1973; Nolte *et al.*, 1976; Zirker, 1977; Sheeley and Harvey, 1978, 1981). Also during this period a nearly one-to-one association was established between coronal holes and regions of open field lines derived from potential magnetic field calculations using observed photospheric line-of-sight fields (Altschuler and Newkirk, 1969; Levine, 1977, 1982). However, it has been suggested that these relationships are less clear during other parts of the cycle. For instance, Levine (1977, 1982) showed that during Skylab and around solar maximum open fields also emanate from active regions, and Nolte *et al.* (1977) and Sheeley and Harvey (1978, 1981) showed that during solar minimum and the rise to maximum of cycle 21 there were solar wind sources that could not be identified with low-latitude coronal holes.

Since the Skylab mission, ground-based He I 10830 Å images have been used (e.g., Sheeley and Harvey, 1978, 1981) for determining coronal hole positions and areas and their relationships to solar wind speeds and geomagnetic activity indices. In addition, rocket flights have provided us with high resolution, full-disk solar X-ray images at

Solar Physics **102** (1985) 177–190.

approximately 18-month intervals. At AS & E these images have been used in a program to study the evolutionary characteristics of coronal holes over the solar cycle, including the degree of their correspondence to open field configurations. As part of this program, Kahler *et al.* (1983) compared coronal hole boundaries determined from both AS & E X-ray and Kitt Peak 10830 Å images. During their study, they found what appeared to be a decrease in the brightness contrast between the coronal holes and large-scale coronal structure in the period after 1974. Such a 'weakening' of holes was also observed in the 10830 Å data alone during 1976–1977 by Sheeley and Harvey (1978). Also, Levine (1982) determined that the association between predicted open magnetic structures and 10830 Å coronal holes was less clear after the Skylab period.

Finally, Harvey *et al.* (1982) found that low-latitude coronal holes contained three times more flux near sunspot maximum than near minimum even though their areas were comparable. Taken together, these results suggest that the distinction in terms of open and closed fields between coronal holes and large-scale structure is not always as clear as during the declining phase of solar cycle 20.

This paper describes the next phase of our program, the photometric analysis of the soft X-ray energy flux from coronal holes from 1974 to 1981 and the comparison of this flux with measurements of photospheric magnetic field strength. We have addressed two questions: (1) In terms of apparently contradictory results using Skylab X-ray data, is X-ray emission from coronal holes detectable above background, and if so does it vary over the solar cycle? (2) Can a change in the plasma conditions within low-contrast coronal holes explain the difference in visibility, and are these conditions in turn related to the increased photospheric field strength found in the coronal holes of the new cycle?

2. Observational Analysis

Our approach to this study involved three phases. First, we selected those X-ray images which most clearly showed coronal holes for calibration and measurement of hole emission. The minimum average energy flux within the coronal hole boundaries as determined by Kahler *et al.* (1983) was measured and variations in this emission over the solar cycle were examined. Second, the average magnetic field strength within the same X-ray coronal hole boundaries was measured. Finally, the X-ray and magnetic flux measurements were compared to each other and to the magnetic flux measurements of Harvey *et al.* (1982).

2.1. Calibration and analysis of the X-ray data

Since Skylab, full-disk soft X-ray images of the solar corona have been obtained on seven AS & E rocket flights in 1974, 1976, 1978, 1979, and 1981. Kahler *et al.* (1983) provided details on the dates, times, and instrumentation of the flights (except for 17 November, 1976). Images on these flights were obtained with two mirror systems, a Kanigen metal mirror and a fused silica mirror. To minimize the relative uncertainties between flights and the background from scattering effects, we restricted our analysis to images obtained with the fused silica mirror and through aluminized polypropylene

TABLE I

Selected X-ray images and magnetograms

X-ray images	Time (UT)	Carrington rot.	CR[a]	Mt. Wilson daily maps[b]	Kitt Peak synoptic maps
27 June, 1974	1948	1616	6	26 June; 1456 27 June; 1652 28 June; 1715	No
17 Nov., 1976	1827	1648	32	16 Nov.; 1659 17 Nov.; 2243 18 Nov.; 1751	No
31 Jan., 1978	1841	1664	16	31 Jan. 1 Feb.; 1846	Yes (gap)
13 Feb., 1981	1916	1705	41	14 Feb.; 2326	Yes

[a] The interval in Carrington rotations betwen rocket observations. The 1974 observations occurred six rotations after Skylab.
[b] Times are UT at the midpoint of the mapping interval.

TABLE II

X-ray energy flux in coronal holes

Date	Coronal hole subareas	PP exposure time (s)	Average PDS density	Net intensity (erg cm^{-2} s^{-1})
27 June, 1974	Large hole: center	19.7	21.6 ± 1.2	$2.2 \pm 0.8 \times 10^{-3}$
		59.2	32.6 ± 2.2	$2.1 \pm 0.7 \times 10^{-3}$
	Large hole: northwest	19.7	19.5 ± 0.8	$1.7 \pm 1.3 \times 10^{-3}$
		59.2	27.8 ± 1.9	$1.4 \pm 0.5 \times 10^{-3}$
	North polar hole	19.7	21.0 ± 2.1	$2.1 \pm 1.6 \times 10^{-3}$
		59.2	30.3 ± 4.1	$1.8 \pm 1.2 \times 10^{-3}$
17 Nov., 1976	Equatorial extension of SPH	3.7	13.0 ± 0.7	$7.5 \pm 3.3 \times 10^{-3}$
		16.5	18.8 ± 1.2	$5.6 \pm 2.0 \times 10^{-3}$
	South polar hole	3.7	12.6 ± 0.8	$6.4 \pm 3.0 \times 10^{-3}$
	North polar hole	16.5	17.4 ± 1.1	$4.6 \pm 1.7 \times 10^{-3}$
		3.7	13.5 ± 0.8	$8.3 \pm 3.8 \times 10^{-3}$
		16.5	19.7 ± 1.3	$6.1 \pm 2.2 \times 10^{-3}$
31 Jan., 1978	Southwest hole: center	2.6	18.6 ± 0.9	$1.7 \pm 0.9 \times 10^{-2}$
		8.7	25.8 ± 1.3	$1.6 \pm 0.9 \times 10^{-2}$
	Southwest hole: limb	2.6	18.1 ± 1.0	$1.6 \pm 0.8 \times 10^{-2}$
		8.7	25.4 ± 0.8	$1.5 \pm 0.9 \times 10^{-2}$
13 Feb., 1981	Southern hole: limb	2.8	24.3 ± 1.4	$1.5 \pm 1.2 \times 10^{-1}$
		9.6	39.2 ± 1.6	$1.3 \pm 1.0 \times 10^{-1}$
	Southern hole: center	2.8	26.6 ± 1.7	$1.8 \pm 1.3 \times 10^{-1}$
		9.6	41.8 ± 1.5	$1.5 \pm 1.2 \times 10^{-1}$

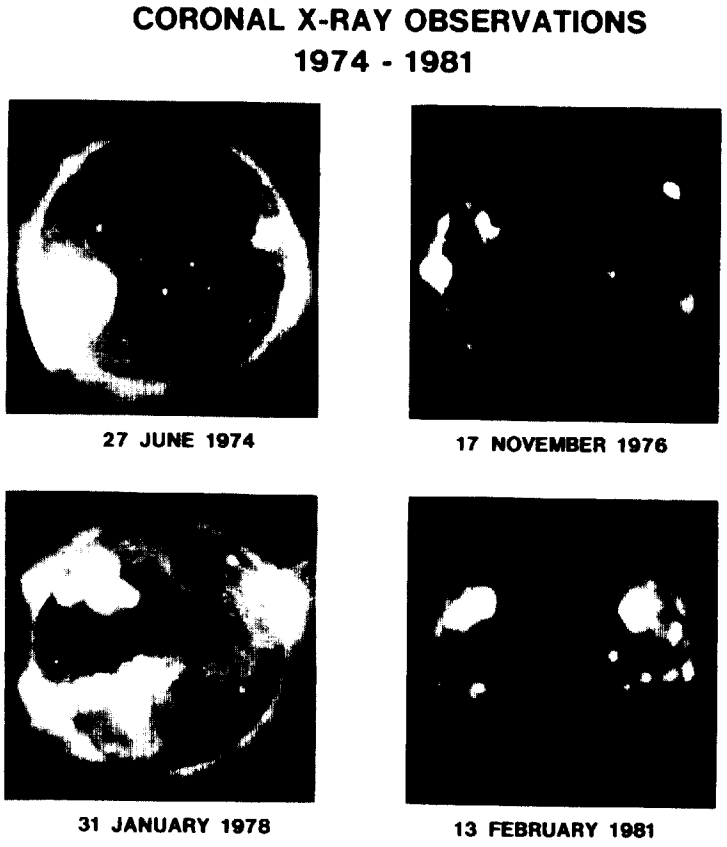

Fig. 1. Soft X-ray images of the solar corona for the four dates analyzed in this study. All images were obtained with the AS & E fused silica mirror and with polypropylene filters. The exposure times vary. Solar north is up and east to the left for all images. The central meridian longitudes L_0 for the four images in time order were: 237, 220, 175, and 298°.

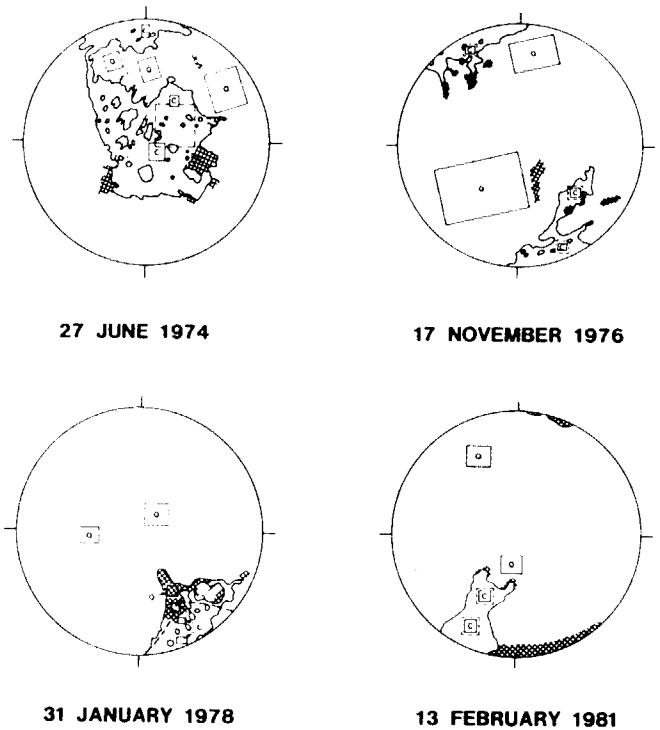

Fig. 2. Tracings of X-ray coronal hole boundaries from Kahler *et al.* (1983) to the same scale as Figure 1. Hatched areas indicate uncertain X-ray holes. See Kahler *et al.* for details on the boundary determinations. The solid boxes indicate the subareas in which the X-ray measurements of emission from coronal holes ('C') and the diffuse background corona ('Q') were made. The dashed subareas indicate where the magnetic flux was measured.

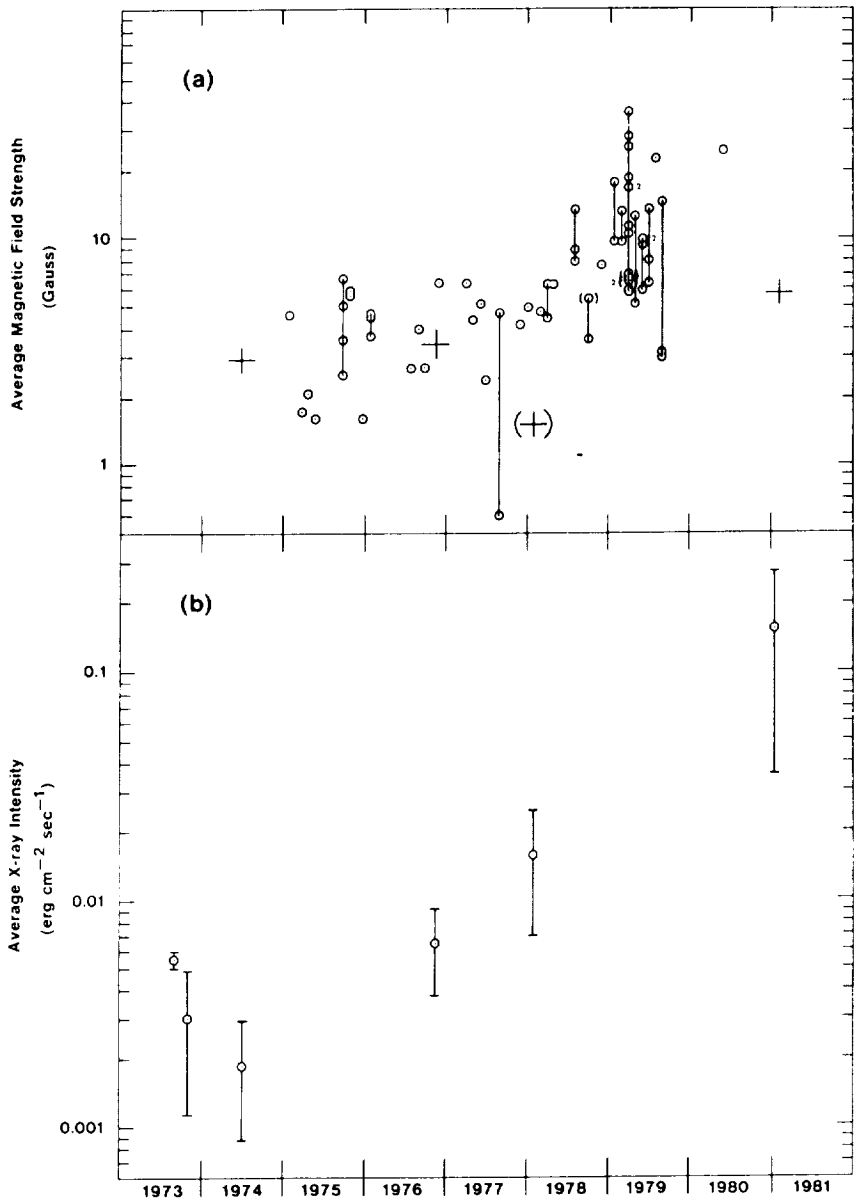

Fig. 3. Overall comparison of the magnetic field strength and X-ray flux of coronal holes from 1974 to 1981. (a) Semi-log plot of magnetic field strengths from Kitt Peak synoptic maps within 10830 Å coronal hole boundaries from 1975 to 1980 (from Table I of Harvey *et al.*, 1982). Points joined by vertical lines represent measurements of different holes made during the same month. The crosses indicate the averaged Mt. Wilson measurements for the X-ray equatorward holes (see text). (b) Semi-log plot to the same timescale as (a) of the X-ray energy fluxes of the Skylab and rocket coronal holes listed in Table II. For each flight all of the measurements have been averaged together and plotted as a single point. Each error bar is a simple average of the measurement uncertainties for each flight.

(PP) and beryllium (BE) filters. The passbands of the PP filters used in these flights are similar to Filter 3 used with the Skylab S-054 instrument (Vaiana *et al.*, 1977) to study coronal holes. Table I lists the dates, times, and Carrington rotations of the X-ray data from the four rocket flights analyzed for this study*, and the dates and times of the magnetogram data we used. Representative PP images from the four flights are shown in Figure 1 and the X-ray coronal hole boundaries from Kahler *et al.* (1983) are reproduced in Figure 2 to the same scale. The 17 November, 1976 boundaries, though not included in their paper, were drawn by Kahler *et al.* during their analysis. Their 1976 and 1981 boundaries compare favorably with those determined independently by Nolte *et al.* (1977) and Webb *et al.* (1984), respectively.

To determine coronal plasma parameters, the X-ray photographic density images must be calibrated and reduced to arrays of energy flux deposited on the film plane. Details of the reduction and calibration of the rocket images are discussed by Davis and Webb (1985). Since the rocket images were obtained with the same film emulsion, Eastman Kodak SO-212, used with the AS&E Skylab telescope, we followed the general calibration procedures developed for the Skylab analysis (Vaiana *et al.*, 1977). Each flight image was scanned with AS&E's PDS microdensitometer to produce a digitized density array with 20 micron pixels, equivalent to 2.8 arc sec spatial resolution. Because of difficulties with laboratory calibration of the wavelength dependence of the X-ray sensitivity of SO-212 film, we used a synthesized calibration procedure based on the image data themselves (cf. Maxson and Vaiana, 1977) to provide absolute energy calibrations for each flight. The uncertainties in the film calibration lead to relatively large error ranges in the measured coronal hole energy fluxes. However, as we will show, our results still provide meaningful limits on the cyclical dependence of energy flux from coronal holes.

Subareas were chosen to encompass areas of minimum brightness in the holes and are indicated on Figure 2 by the boxes labelled 'C'. These subareas were carefully chosen to exclude regions of brighter diffuse emission and bright point-like features within each hole boundary, and to be distant from active regions so as to minimize scattering effects. Generally the average density and statistical error at at least two subareas per hole and on two adjacent PP images was measured. The resulting average X-ray intensities and uncertainties derived for the coronal hole subareas shown in Figure 2 are listed in Table II.

In Figure 3(b) the X-ray coronal hole flux measurements are presented as a function of time over nine years of solar cycles 20 and 21. The two 1973 points are averages of the two sets of published Skylab X-ray measurements of the emission from coronal holes. The first point is the average of six measurements of two areas in Coronal Hole 1 (CH 1) made in August 1973 using two low-density calibration methods (Maxson and Vaiana, 1977). The second point is the average of three measurements of the emission

* Although small coronal holes were visible on the day of our rocket flight on 7 November, 1979 (see Figure 4 in Webb *et al.*, 1984), that data could not be used for this study because scattered radiation from a flare precluded photometric measurements in faint areas.

from CH 6 shortly after its birth on the disk in October 1973 (Solodyna *et al.*, 1977). From 1974 to 1981 the X-ray measurements for each rocket flight in Table II have been averaged together and plotted as a single point. This procedure is justified because the uncertainties of each point are larger than the variations of the intensities between exposures or among the different coronal holes observed on each flight.

A clear trend in the X-ray emission is apparent. The coronal hole emission in 1973, 1974, and 1976 was similar and low, but rose to a maximum in 1981. Examining only the rocket data, average coronal hole emission was lowest in June 1974, a factor of 3 higher in November 1976 near solar minimum, and a factor of 8 higher in January 1978. The emission from the large southern hole in February 1981 near solar maximum was an order of magnitude higher than in 1978, although with larger uncertainties due to the film calibration and possible scattering problems.

We derived gas pressure from the average coronal hole X-ray intensities using the technique developed by Kahler (1976). This method is applicable over the temperature range where a single filter's response is temperature insensitive. Therefore, the method is especially useful when the plasma temperature and density cannot be uniquely determined, as in our case. For the fused silica mirror the pressure, in dyne cm^{-2}, is given by:

$$P_i^2 = 3.49 \times 10^{-14} I_i / L\alpha ,$$

where I_i is the focal plane intensity through filter i in erg cm^{-2} s^{-1}, L is the pathlength in cm, and α is a function of the assumed filtered solar spectrum, corrected for film speed, and T^2. For L we assumed the constant density scale height of 6.5×10^9 cm derived by Vaiana *et al.* (1973) for an X-ray coronal hole observed in 1970. Table III presents the results for the PP images from each rocket flight under two temperature assumptions. Column 2 shows the hole pressures for an assumed constant temperature of 1.3×10^6 K, i.e., the barometric temperature for the 1970 coronal hole (Vaiana *et al.*, 1973). In column 4 are given the pressures derived using an average value of α over the full temperature range over which the PP filter is temperature insensitive to within $\pm 33\%$ (for the rocket PP filter this occurs from 0.7 to 5×10^6 K). Pressures derived

TABLE III

Derived coronal hole pressures[a]

Date	P (1.3×10^6 K)[b] (dyn cm^{-2})	ΔP (above 1974 level)	P ($\langle \alpha(T) \rangle$)[b] (dyn cm^{-2})	ΔP (above 1974 level)
Skylab	0.050	1.8	0.029 – 0.081 ($0.9 < T_6 > 3.0$)	
1974	0.027 ± 0.003	–	0.031 ± 0.004	–
1976	0.054 ± 0.003	2.0	0.063 ± 0.003	2.0
1978	0.078 ± 0.008	2.9	0.090 ± 0.010	2.9
1981	0.310 ± 0.068	11.5	0.352 ± 0.072	11.3

[a] For an assumed density scale height of 6.5×10^9 cm.

[b] The uncertainties represent the ranges in pressures due only to the uncertainties in the film calibration.

by Maxson and Vaiana for Skylab CH 1 are given as a reference. Shown in columns 3 and 5 are the ratios of the hole pressures with respect to 1974, showing a tenfold increase between activity minimum and maximum.

We also estimated the emission measure, $\int n_e^2 \, dl$ (Vaiana *et al.*, 1977), from the average coronal hole intensities. We assumed a constant $T_e = 1.3 \times 10^6$ K and derived average emission measures ranging from about 4×10^{25} cm^{-5} in June 1974 to 5×10^{27} cm^{-5} in February 1981. The values derived from the average hole intensities for 1974, 1976, and 1978 are within a factor of 3 of the emission measure at 1.3×10^6 K for CH 1 of 1.3×10^{26} cm^{-5} (Maxson and Vaiana, 1977).

Because coronal hole fluxes are very small, an understanding of the X-ray calibration and reduction procedures is important. Of particular concern in X-ray measurements are scattering effects arising from surface roughness of the mirrors, which can contribute an important source of background 'noise'. Thus, our decision to make no corrections for scattering in our analysis must be justified. In analyzing the Skylab data, Maxson and Vaiana concluded that CH 1 had significant emission over background. They made no corrections for scattering, claiming that such effects were minimized by choosing subareas far from bright sources, and because CH 1 had a large area and cross sections through the hole revealed flat-bottomed profiles inconsistent with scattering effects. To the contrary, Solodyna *et al.* (1977) estimated significant scattering contributions from individual sources and concluded that the CH 6 emission after its development 'was consistent with zero within our assessment of the experimental uncertainties'. However, unlike CH 1, CH 6 at the time of Solodyna *et al.*'s measurement was a very small hole surrounded by large-scale structures (LSS) and active regions, and flaring occurred in a limb region during some of the observations. Like Maxson and Vaiana we attempted to minimize the effects of scattering by choosing subareas away from bright regions and checking cross-sectional profiles through the holes. More importantly, we only used rocket data obtained with the fused silica mirror, which has improved scattering characteristics compared with the Skylab mirror (Davis *et al.*, 1977). For instance, the scattering is substantially reduced at shorter wavelengths and is nearly wavelength

TABLE IV

Contrast ratios:
diffuse coronal emission / coronal hole emission

Date	Ratio
21 Aug., 1973[a]	8.4 ± 1.2[b]
27 June, 1974	11.1 ± 6.8
17 Nov., 1976	5.4 ± 3.0
31 Jan., 1978	3.5 ± 2.8
13 Feb., 1981	3.0 ± 3.2

[a] Skylab from Maxson and Vaiana (1977). The ratio of the LSS emission from their region 'D' divided by the emission from CH 1.

[b] The errors are the statistical errors of the ratios of the uncertainties discussed in the text.

independent. It must be emphasized that neither the Skylab nor rocket coronal hole measurements include the effects of systematic errors which might arise from uncertainties in the calibration data, including the wavelength dependence of film aging, and the absolute source spectrum.

We measured average intensities of diffuse background coronal subareas as a means of comparing the coronal hole flux variations with overall cyclical variations in coronal plasma conditions and to cross-check the data from each rocket flight. These subareas, labelled 'Q' in Figure 2, were chosen to include large-scale areas of minimal coronal emission on the disk *away* from coronal holes, active regions and bright LSS. For each image these subareas were averaged together and compared with the averaged coronal hole fluxes plotted in Figure 3(b). Table IV shows for each date the coronal contrast ratio between the diffuse emission and the coronal hole emission. This ratio decreased from 1974 to 1981, thereby quantitatively confirming the previous suggestions from both X-ray and 10830 Å observations that the brightness contrast between holes and large-scale structure decreased during the rise to solar activity maximum.

2.2. Analysis of the Photospheric Magnetic Field Strength Data

In the next phase of the analysis we compared as a function of time the X-ray emission and the photospheric magnetic flux density from the coronal holes, using the boundaries determined by Kahler *et al.* (1983). For the magnetic field data we used daily averaged magnetic flux maps from Mt. Wilson Observatory and Kitt Peak synoptic flux maps constructed for each Carrington rotation (Harvey *et al.*, 1980). Table I lists the dates and times of the Mt. Wilson magnetograms. Kitt Peak data were not available for long periods around the dates of the rocket flights in 1974 and 1976, and contained a three-day gap centered on 31 January, 1978, the date of the third flight. However, the Mt. Wilson daily maps were available on or within one day of each of the four rocket flights analyzed. To check for day-to-day variations in the maps, we required maps on the day of the flight, the day before and the day after. However, for the 1978 flight only maps on the day of the flight and the day after were available, and in 1981 only one map was available on the day after the flight. Fortunately, good Kitt Peak data were obtained for the 1981 period.

We obtained the Mt. Wilson data in the form of averaged pixels in Gauss integrated over 34 × 34 equal intervals of sine longitude and sine latitude, therefore representing large area averages of flux density. The magnetograph measures the longitudinal component of the photospheric field in the 5250 Å line of Fe I. Because of line weakening, the values measured are on the order of a factor of two too low, although the magnitude of this effect varies across the disk (Howard and Stenflo, 1972). Our results were corrected for this effect and for foreshortening as described below.

We obtained the Kitt Peak synoptic maps in the form of digitized equal-area pixels in Gauss of one degree longitude by (1/90) unit of sine latitude of the mean field strength. The data were obtained with the 512-channel magnetograph which measures the longitudinal field in the 8688 Å line of Fe I and requires no correction outside of

sunspots. Where necessary a cosine weighting function in longitude has been applied to the synoptic data to merge it across daily data gaps.

We selected rectangular subareas on the magnetic maps that corresponded spatially with the coronal hole subareas in which the X-ray measurements were made. These subareas are shown by the dashed outlines on Figure 2. For the 1976 and 1981 data the subareas coincided with the X-ray subareas, but for 1974 and 1978, we used single large subareas to increase the statistical accuracy of the measurements. Because of the large area of the holes in 1974 and 1978 and the coarse spatial resolution of the Mt. Wilson data, we feel that the integration of the X-ray and magnetic data over dissimilar areas did not significantly effect the results. The results of our analysis of the coronal hole magnetic field strengths are given in Table V. The table lists the dates and subareas measured in terms of the X-ray coronal hole designations used in Table II.

TABLE V

Average magnetic field strength in coronal holes

Date	Coronal hole subareas	Polarity	Observatory	Net B_T (G)	θ_c (deg)
26 June, 1974	Large hole: center	+	MW daily	+2.87	14.5
27 June, 1974	Large hole: center	+	MW daily	+3.06	19
28 June, 1974	Large hole: center	+	MW daily	+2.88	31.5
16 Nov., 1976	Equatorial ext.	−	MW daily	−2.51	27.6
17 Nov., 1976	Equatorial ext.	−	MW daily	−3.23	34.8
17 Nov., 1976	South polar hole	−	MW daily	−3.68	59.8
17 Nov., 1976	South polar hole	+	MW daily	−0.34	59.8
18 Nov., 1976	Equatorial ext.	−	MW daily	−4.53	44.5
31 Jan., 1978	Southwest hole	−	KP synoptic	−1.28	(55)[a]
31 Jan., 1978	Southwest hole	−	MW daily	−2.23	64.6
1 Feb., 1978	Southwest hole	−	MW daily	−0.80	68.4
13 Feb., 1981	Southern hole: limb	+	KP synoptic	+1.55	(58)[a]
13 Feb., 1981	Southern hole: center	+	KP synoptic	+5.60	(40)[a]
14 Feb., 1981	Southern hole: limb	+	MW daily	+4.50	66.4
14 Feb., 1981	Southern hole: center	+	MW daily	+5.74	40.1

[a] The average longitudes for the coronal hole locations on the Kitt Peak maps are estimates only.

Column 3 gives the known polarity of the hole as determined by Hα synoptic charts in *Solar-Geophysical Data* and the magnetic field/solar wind observations of Sheeley and Harvey (1981). With one exception (i.e., the north polar hole on 17 November, 1976) the measured polarities agreed with the expected ones.

The average longitudinal field strength B_m for each hole subarea was calculated by computing the algebraic sum of all pixels within the chosen subarea and dividing by the number of pixels. The Mt. Wilson data were then corrected for line weakening and foreshortening by using the form given by Howard (1977) to derive the 'true' field strength B_T:

$$B_T = B_m \frac{0.48 + 1.33 \cos\theta}{\cos\theta} ,$$

where θ is the great-circle distance from Sun center to the center of the subarea. In Table V the value B_T is given in column 5 and θ in column 6. In addition, the June 1974 Mt. Wilson measurements were increased by 20% to account for a change in the magnetograph aperture in 1975 (R. Howard, private communication). The Kitt Peak synoptic data are already corrected for the longitude projection effect, so we applied a latitude correction of the form $B_c = B_m/\cos\theta$. The Mt. Wilson and Kitt Peak measurements within the February 1981 hole equatorial extension suffer least from foreshortening and agree with 3%.

Harvey *et al.* (1982) used Kitt Peak synoptic images to determine the magnetic fluxes in thirty-three 10830 Å coronal holes from 1975 to 1980. They only analyzed holes below a latitude of 50° and made no corrections for projection effects. In Figure 3(a) we have plotted their field strength data from their Table I. This plot illustrates their result that during this phase of solar cycle 21, low-latitude holes contained three times more flux near activity maximum than at minimum.

The corrected Mt. Wilson flux values (B_T) shown in Table V for the days centered on the rocket flights have been averaged together and plotted as crosses on Figure 3(a). We included the single Mt. Wilson measurement on 14 February, 1981 the day after the rocket flight. One of the Harvey *et al.* measurements (coronal hole No. 18 on 19 October, 1976) was from the southern equatorial extension that we measured one rotation later on 16–18 November, 1976. Our averaged measurement for this hole of − 3.4 G agrees favorably with their value of − 2.7 G. In general, our coronal hole fluxes are consistent with the trend of the Harvey *et al.* data (note: the 1978 value was subject to considerable foreshortening).

3. Discussion

We now summarize our observational results in terms of the questions posed in the Introduction. First, we conclude that the rocket results confirm earlier Skylab results that detectable X-ray emission arises from coronal holes. In addition we find that this emission appears to increase as the cycle evolves from activity minimum to maximum. One can take the view that despite the uncertainties arising from differing calibration procedures, and the diversity in coronal hole area, location on the disk and evolutionary characteristics, the four independent data sets from 1973 to 1976 reveal remarkably consistent X-ray hole emission values varying over this period near sunspot minimum by only about a factor of three. The 1974 rocket measurements are also consistent with Solodyna *et al.*'s (1977) measurements of CH 6 made only 8 months earlier. However, when the data over this entire 9-year period of the solar cycle is examined, the observed X-ray coronal hole emission appears to vary roughly with the sunspot cycle, reaching minimum flux in 1974 just before sunspot minimum*, then increasing through 1981, about one year after sunspot maximum. Finally, because the rate of intensity increase

* We cannot rule out that coronal hole emission in October 1973 (Skylab) and June 1974 (rocket) was below the detection threshold and, therefore, that these values are upper limits.

of the X-ray hole flux was greater than that of the background flux (Table IV), our photometric results confirm the qualitative suggestion of Kahler *et al.* (1983) and Sheeley and Harvey (1978, 1981) that the brightness contrast between coronal holes and large-scale structure decreased during the rise to activity maximum.

Figure 3 provides a partial answer to our second question, namely does a relationship exist between increasing X-ray emission and increasing magnetic field strength from coronal holes over this period of the cycle? The data of Harvey *et al.* (1982; our Figure 3(a)) show an increase of a factor of three in the field strength of near-equatorial coronal holes between 1975 and 1980. Our calculations of field strength within the X-ray hole boundaries are sparse but consistent with the Harvey *et al.* data. The X-ray emission (Figure 3(b)) shows an increasing trend with the cycle, in general agreement with the magnetic flux but with greater amplitude. Comparison of these two data sets over the same time period reveals that they appear to have a power law dependence. The relationship is such that the coronal hole X-ray intensity, which is proportional to the gas pressure (Table III), is consistent with being proportional to B^2. Thus, the data lend support to coronal heating models in which the corona is directly heated by the dissipation of magnetic energy (e.g., Rosner *et al.*, 1978). We may speculate from our results that such magnetic heating occurs routinely in coronal holes over the solar cycle.

It is important to attempt to relate the observed change in coronal hole contrast over the cycle with the degree to which the underlying magnetic fields were open or closed. We examined two approaches to this question: (1) by directly comparing the location and contrast of our holes with regions of open fields as deduced from potential field models, and (2) by examining the interplanetary effects of the low-latitude holes or extensions of holes observed in our data.

Regarding the first approach, Levine compared regions of open fields with the Skylab data on coronal holes (e.g., Levine, 1977) and with 10830 Å holes observed in 1975 and 1978–1979 (Levine, 1982). However, his comparisons were made during periods when we had no rocket observations and, therefore, we are unable to make any direct comparisons. However, our observation of the southern hole extension in January 1978 could be indirectly compared with Levine's (1982) results starting in May 1978. Levine's Figures 3–6 confirm that this lobe was detected as a strong open field region of similar size and shape and persisting through the period of Levine's study.

Concerning the second approach, we decided to examine the interplanetary effects of our holes because of the well-known, strong correlation during Skylab between low-latitude holes and, therefore, apparently open field regions, and high speed solar wind streams. In addition, we sought assurance that our holes were reasonably typical of each epoch with regard to their evolutionary characteristics and effects on the solar wind. We compared the locations and timing of our low-latitude holes with the Bartels displays and discussions of Sheeley and Harvey (1978, 1981).

The large coronal hole in June 1974 was the only one in our data which extended over the equatorial region. This hole evolved from a separate, small equatorial hole during Skylab (CH 4) to join with the north polar hole by mid-January 1974 (Solodyna *et al.*, 1975). The Bartels display shows that in June 1974 this hole was midway through its

lifetime. Through mid-1975 this hole and another of opposite polarity formed a two-sector structure of strong, recurrent solar wind. These holes, and their associated wind streams, had a 27-day recurrence period. These characteristics were typical of equatorial holes observed during Skylab (e.g., Zirker, 1977).

The equatorial extension holes observed on the rocket images on 17 November, 1976 and 31 January, 1978 represented the early development of long-lived, slowly rotating (28–29 day periods) but weak holes. Sheeley and Harvey (1978) described the 1976 hole as follows: "Despite its weak appearance, this hole was associated with one of the most prominent recurrence patterns of high-speed solar wind and enhanced geomagnetic activity that occurred during 1976–1977." Finally, on 13 February, 1981 the large, high-latitude coronal hole was embedded in the first new-cycle polarity region (Webb *et al.*, 1984) and was probably associated with a recurrent wind stream. All of the near-equatorial X-ray holes were associated with IMF polarity of the same sign (Sheeley and Harvey, 1981).

Taken together, these facts suggest that these holes were strongly connected with the interplanetary medium flow by open field lines emanating from the base of the holes. These indirect comparisons support a general correspondence between open field regions and the X-ray coronal holes of our study. But the variation of X-ray flux from coronal holes does not appear to be strongly dependent on the degree of the open field structures. We hope to extend this inference by directly comparing the X-ray coronal hole data with open field structures as deduced from potential field calculations.

In conclusion, our limited X-ray results provide evidence for a solar cycle variation in overall coronal hole emission and gas pressure, which is supported by the qualitative, but more frequent observations of a 'weakening' or decreased contrast of 10 830 Å holes and an increase in the surface magnetic flux within holes over the same period. The variation of the coronal pressure is consistent with being proportional to the square of the magnetic flux, suggesting the importance of magnetic energy dissipation to heating at the base of coronal holes.

Acknowledgements

We would like to thank J. Harvey and R. Howard of the National Solar Observatory for providing the photospheric magnetic field data used in this study and for helpful discussions. We also acknowledge useful discussions on calibration of the X-ray data with C. Maxson of the Center for Astrophysics and S. Kahler of Emmanuel College. We appreciate the assistance of M. Rizza and F. Simpson of AS & E in the preparation of the figures. This study was funded by the Air Force Geophysics Laboratory/PHS, Air Force Systems Command, under contract F19628-84-C-0037. The acquisition and initial reduction of the rocket data was supported by NASA under contracts NAS5-25496 and NAS2-8683.

References

Altschuler, M. D. and Newkirk, G., Jr.: 1969, *Solar Phys.* **46**, 185.

Davis, J. M. and Webb, D. F.: 1985, 'A Study of the Cyclical Variations of Coronal Holes and Their Relation to Open Magnetic Fields', AFGL-TR-85-0003.

Davis, J. M., Golub, L., and Krieger, A. S.: 1977, *Astrophys. J.* **214**, L141.

Harvey, J., Gillespie, B., Miedaner, P., and Slaughter, C.: 1980, *Report UAG-77*, World Data Center A, NOAA, Boulder, CO.

Harvey, K. L., Sheeley, N. R., Jr., and Harvey, J. W.: 1982, *Solar Phys.* **79**, 149.

Howard, R.: 1977, *Solar Phys.* **52**, 243.

Howard, R. and Stenflo, J. O.: 1972, *Solar Phys.* **22**, 402.

Kahler, S.: 1976, *Solar Phys.* **48**, 255.

Kahler, S. W., Davis, J. M., and Harvey, J. W.: 1983, *Solar Phys.* **87**, 47.

Krieger, A. S., Timothy, A. F., and Roelof, E. C.: 1973, *Solar Phys.* **29**, 505.

Levine, R. H.: 1977, in J. B. Zirker (ed.), *Coronal Holes and High Speed Wind Streams*, Colorado Associated University Press, Boulder, Colo., p. 103.

Levine, R. H.: 1982, *Solar Phys.* **79**, 203.

Maxson, C. W. and Vaiana, G. S.: 1977, *Astrophys. J.* **215**, 919.

Nolte, J. T., Krieger, A. S., Timothy, A. F., Gold, R. E., Roelof, E. C., Vaiana, G. S., Lazarus, A. J., Sullivan, J. D., and McIntosh, P. S.: 1976, *Solar Phys.* **46**, 303.

Nolte, J. T., Davis, J. M., Gerassimenko, M., Lazarus, A. J., and Sullivan, J. D.: 1977, *Geophys. Res. Letters* **4**, 291.

Rosner, R., Tucker, W. H., and Vaiana, G. S.: 1978, *Astrophys. J.* **220**, 643.

Sheeley, N. R., Jr. and Harvey, J. W.: 1978, *Solar Phys.* **59**, 159.

Sheeley, N. R., Jr. and Harvey, J. W.: 1981, *Solar Phys.* **70**, 237.

Solodyna, C. V., Nolte, J. T., and Krieger, A. S.: 1975, memo to Skylab Solar Workshop Participants.

Solodyna, C. V., Krieger, A. S., and Nolte, J. T.: 1977, *Solar Phys.* **54**, 123.

Vaiana, G. S., Krieger, A. S., and Timothy, A. F.: 1973, *Solar Phys.* **32**, 81.

Vaiana, G. S., Van Speybroeck, L., Zombeck, M. V., Krieger, A. S., Silk, J. K., and Timothy, A.: 1977, *Space Sci. Instr.* **3**, 19.

Webb, D. F., Davis, J. M., and McIntosh, P. S.: 1984, *Solar Phys.* **92**, 109.

Zirker, J. B. (ed.): 1977, *Coronal Holes and High Speed Wind Streams*, Colorado Associated University Press, Boulder, Colo.

4.16 The Measured Performance of a Grazing Incidence Relay Optics Telescope for Solar X-Ray Astronomy

Dan Moses, Allen S. Krieger, and John M. Davis

American Science and Engineering, Inc.
Cambridge, Massachusetts 02139

Reprinted from SPIE Vol. 691—X-Ray Imaging II

The measured performance of a grazing incidence relay optics telescope for solar X-ray astronomy

Dan Moses, Allen S. Krieger, and John M. Davis*

American Science and Engineering, Inc., Fort Washington
Cambridge, Massachusetts 02139

Abstract

X-ray astronomy, both solar and celestial, requires long focal length optical systems to provide high spatial resolution images and to be used as feeds for spectrometers. In typical experimental situations, the physical size is restricted and grazing angles must be kept at or below one degree. Grazing incidence secondary optics are an alternative to long focal length primary mirrors. We have designed, fabricated and tested a system which employs a secondary with externally polished hyperboloid-hyperboloid surfaces. It is to be used in conjunction with an existing Wolter-I primary. The system has been designed for high resolution imaging of the solar corona with the goal of producing images electronically with the same spatial resolution as achieved at the primary focus with film. The secondary optic is located in front of the primary focus, as in a Galilean telescope, and provides a magnification of approximately four. The combined system has a plate scale of 26.0 μm (arc sec)$^{-1}$, effective focal length 5.4 m, and is contained within an instrument length of 1.9 m. The design, tolerance specification and fabrication techniques are described. The performance of the system at X-ray wavelengths has been determined experimentally and is compared with theoretical results produced by ray tracing.

Introduction

The field of X-ray astronomy has developed rapidly over the past quarter century spurred by technical advances in the fabrication of grazing incidence optics. These optical systems have allowed the study of X-ray emission mechanisms over a range of astronomical sources from the coronae of stars, including the sun, to supernovae remnants, galaxies and quasars. Although the structure of many of the more distant sources remain unresolved, imaging has revealed a wealth of detail for objects which are relatively close (like the sun) or extend over a large angular extent (e.g., supernovae remnants). In general the structures that are observed reflect the interaction between a high temperature plasma and a magnetic field. For the solar corona the visual identification of a diverse population of coronal structures has provided a new framework for the reformulation of the more classical concepts of solar physics. However, many of the theoretical descriptions involve processes which occur over very small spatial scales. Therefore, future advances will require the acquisition of even higher resolution observations.

In practice the resolution in astronomical observations depends on both the intrinsic resolution of the optical system and the relationship of the size of the image to that of the detector. In the past nearly all X-ray images have been detector limited[1] even when the recording medium was photographic emulsion. The situation is worse when solid state detectors are used. However, for most space missions, electronic imaging has to be used since there is no opportunity to recover film. Consequently there are strong incentives for the development of imaging systems, optics and detectors, in which the performance of each element is optimized for maximum system performance.

When the system angular resolution is limited by the detector, the instrument designer has produced a mismatch between the instrument's focal length and the dimensions of the detector pixel. Although efforts continue to improve the latter, electronic detectors are unlikely to surpass the spatial resolution of photographic film. Therefore it is essential to simultaneously explore the second factor, namely increasing the focal length of the X-ray telescope.

To quantify these statements, we establish a requirement for a system spatial resolution of 1 arc second. If features on this scale are to be resolved, they must subtend an angle greater than 1 pixel, and we use the quantity of $2\sqrt{2}$ pixel size to define limiting resolution. Taking the pixel size as 15 microns, the best that is currently available in CCDs, the instrument focal length would have to be 8.75 m. This results in an instrument size which is impractical for any but major programs. The solution to this problem in normal incidence optical systems would be to use secondary optics to increase the effective focal length, i.e., magnify the primary image. Until recently this approach had not

* Present Address: NASA/Marshall Space Flight Center, Code ES-52
Huntsville, Alabama 35812

been followed for X-ray imaging because of the difficulties associated with the figuring of small grazing incidence optical elements and the increased scattering from four reflections instead of the customary two. However, recent advances in fabrication technology, in particular in the in-process metrology and the preparation of low-scatter surfaces, have combined to make their development possible. Consequently, under NASA sponsorship, we have designed and fabricated a grazing incidence magnifier to be used in conjunction with an existing grazing incidence primary for solar studies.

Design considerations

Two options for the design of the secondary magnifier are possible. In the first option the secondary optic acts as a microscope and is located behind the primary focal plane. It is known as a converging magnifier and has internally reflecting hyperboloid and ellipsoid surfaces. The second design places the mirror in front of the focal plane where it acts as a Barlow lens. This configuration is known as a diverging magnifier and the mirror has externally reflecting hyperboloid-hyperboloid surfaces[2].

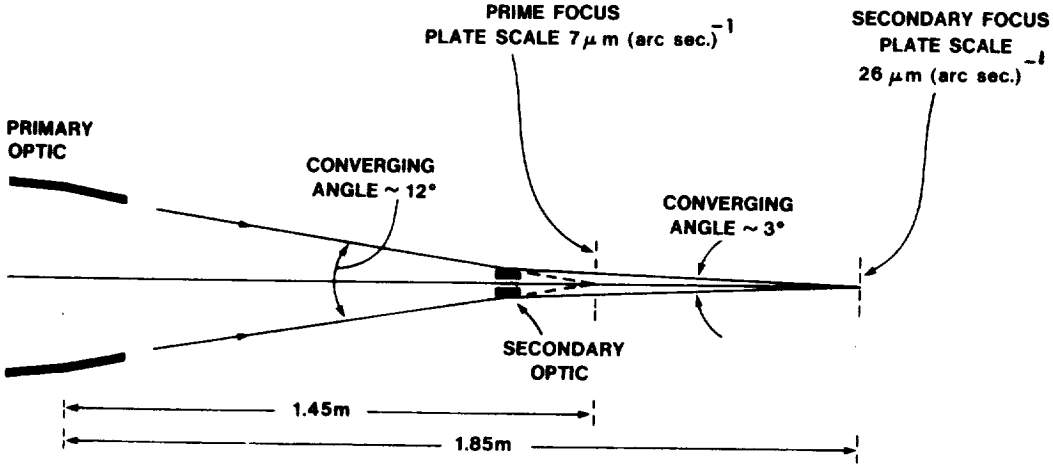

Figure 1. Diagram of the design for the grazing incidence relay optic system.

In the present program, the total length of the system is of critical importance because the telescope will be flown as a sounding rocket payload. For a given object distance and magnification, the diverging magnifier (Figure 1) is the shorter of the two designs. It was selected for this project. An additional benefit of this design is that the primary focused X-rays are bent through a smaller angle to reach the secondary focus, thus minimizing reflection losses and maximizing collecting area.

The design is fixed by choosing the magnification and the object distance (where object distance is the separation between the principle plane of the secondary and the primary focus). In practice increasing magnification lowers the system's speed. Increasing object distance, for a given magnification, lengthens the overall instrument and also increases the physical size of the polished area. A compromise design was chosen which has a magnification of 3.7, corresponding to a plate scale of 26 μm (arc sec)$^{-1}$ while retaining reasonable exposure times. The object distance was set at 14.5 cm. This leads to an overall length for the imaging system of 185 cm which is within the 2 m limit established for the experiment. The general properties of the primary and secondary mirror design are summarized Table 1.

Table 1. Design Requirements of the X-Ray Mirrors

	Primary	Secondary
Figure	Wolter Schwarzschild	Hyperboloid Hyperboloid
Material	Fused Silica	Nickel Coated Beryllium
Principal Diameter	30.48 cm	3.15 cm
Focal Length	144.9 cm	-19.9 cm
Geometrical Area		
On-axis	42.4 cm^2	34.3 cm^2
2 arc minutes	39.6 cm^2	5.8 cm^2
Plate Scale	7.0 μm (arc sec)$^{-1}$	26.0 μm (arc sec^{-1})
Field of View	60 x 60 (arc min)^2	2.5 x 2.5 (arc min)^2
Resolving Power (X-Ray)	1 arc sec	1 arc sec

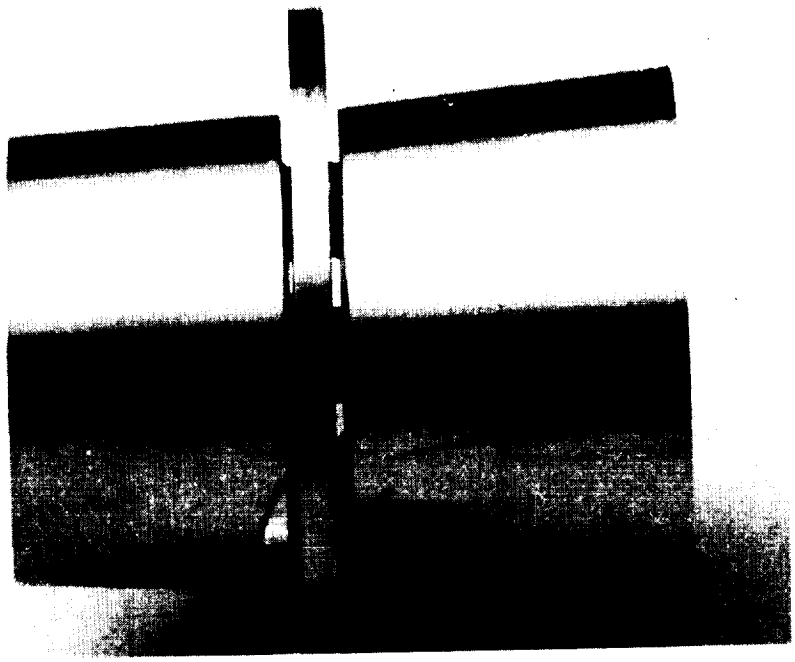

Figure 2. Photograph of the nickel coated hyperboloid-hyperboloid diverging magnifier.

Specification and fabrication

A photograph of the completed diverging magnifier is presented in Figure 2. The equations for the external mirror surfaces of the diverging magnifier are:

$$\text{First Hyperboloid:} \quad \frac{(Z + c)^2}{c^2 - b^2} - \frac{X^2}{b^2} = 1$$

$$\text{Second Hyperboloid:} \quad \frac{(Z + 2c + f)^2}{f^2 - e^2} - \frac{X^2}{e^2} = 1$$

where $c = 1.981416$ $b = 0.167138$
$e = 0.261239$ $f = 6.157995$

The first hyperboloid is located so that its first focus is co-spatial with the focus of the primary mirror. Its second focus is made confocal with the first focus of the second hyperboloid. The second focus of this surface forms, in turn, the secondary focus of the telescope. Since hyperboloids have two foci, small deviations from the design surface can be compensated for by axial displacements with no drawbacks other than a slight change in the overall focal length.

The surface profile was measured in-situ using a laser beam which is scanned over the surface in a controlled way. The local slope is determined from the reflected beam using a position-sensitive detector. The difference between the slope of the required surface and the best fit circle is corrected optically before display. In performing this operation one has to be careful to remember that the geometry established to generate a surface with a given radius will measure a surface with twice that radius and therefore it is necessary to reconfigure the equipment when changing between a polishing and a measuring mode. Typically the best fit spheres have radii on the order of several thousand inches. The error in establishing these radii is on the order of one part in a thousand. This error is acceptable since it can be accommodated during the assembly of the optic by adjustment of the spacer. The signal can also be integrated electronically to obtain the sagittal depth as a function of position. Once a satisfactory surface has been obtained the end pieces are removed from the finished mirror and the radial dimensions measured. As a cost savings measure, the end pieces were made from cast iron. This turned out to be a mistake since it was more difficult to remove this material during polishing. This caused the surfaces near the edges to roll up and the removal of this effect was both difficult and time consuming. Finally, the surfaces were superpolished to provide a low-scatter finish. The mirror was fabricated[3], in two pieces, from optical grade beryllium.

The selected blanks were diamond turned to their approximate dimensions using a numerically controlled lathe. Since the polished area is relatively small, it is important to minimize roll over at the ends and the blanks were turned and lapped with removable end pieces in place. The machined blanks were then nickel plated which was applied to a depth of 0.13 mm over all the surfaces of the two elements. The nickel reflecting surfaces were again single point diamond turned and lapped to the required profile. The work was performed on a modified Random[4] machine utilizing linear, air bearing slides to define tangents to the best fit circle. This circle is used to guide the lathe head which holds the mirror during both the diamond turning and polishing. The radii of curvature, which in our case are on the order of 40 m, are determined with an accuracy of 2 cm and the location of the center of curvature with respect to the surface is known to be better than 1 part in 4000.

Each section is separately mounted to a central plate made of high-strength stainless steel. The plate is supported by four fingers which together intercept less than 3% of the open aperture. The steel chosen, 17-4PH, heat treated to condition H1150, provides a very close thermal match to the beryllium, which is essential to avoid radial distortions of the mirror surfaces under changing temperature conditions. This central plate, in addition to providing support for the two hyperbolas, also acts as the spacer. Adjustment of its thickness allows the two hyperbolas to be made confocal.

The measured dimensions of the individual hyperbolas are compared to the design values in Table 2. The differences are a result of the sequence of operations followed during fabrication. As a result of various technical difficulties, the second hyperbola was completed first. Measurements of the front and back radii were made and the surface profile derived from the measured differences between the actual surface and the best fit circle. An updated hyperbola was calculated to fit these data and the first hyperbola modified to match. The tolerances placed on the reflecting surfaces are shown in Table 3. We identified as the most demanding tolerances that had to be met during the fabrication of the mirror as the roundness of the elements and the deviation of the local slope from that predicted by the design curve. The principal roundness criterion is the variation in the difference between the forward and aft radii of each piece as a function of azimuth. This tolerance is referred to as Δ (ΔR), and for this mirror we established a goal of 6 micro-inches. This is a tighter specification than usual for grazing incidence

Table 2. Secondary Mirror Dimensions (Note: Dimensions Are in Inches)

	Design	Measured
Diameter at front of 1st hyperboloid	= 1.40804	1.40846
Diameter at rear of 1st hyperboloid	= 1.24878	1.25209
Calculated diameter at mid-plane	= 1.24000	
Diameter at front of 2nd hyperboloid	= 1.23527	1.23346
Diameter at rear of 2nd hyperboloid	= 1.16433	1.16485
Length of 1st hyperboloid	= 0.91006	0.9131
Length of 2nd hyperboloid	= 0.74605	0.7433
Gap for center plate	= 0.10000	0.1400

Table 3. Secondary Mirror Tolerances

Optical Tolerance	Definition	Specification (inches or as stated)	Achieved
Average Radius	$R = \bar{R}_a - R_d$	200×10^{-6}	100×10^{-6}
Out of Roundness	$\Delta R = (\bar{R}_f - R_{fd}) - (\bar{R}_r - R_{rd})$	40×10^{-6}	8×10^{-6}
Variation in ΔR	$\Delta(\Delta R) = (R_{f\phi} - \bar{R}_f) - (R_{r\phi} - \bar{R}_r)$	6×10^{-6}	5×10^{-6}
Axial Figures	Sagittal Depth Deviation from Design Curve	3×10^{-6}	5×10^{-6}
Axial Slope Error	$\left(\frac{dR}{dZ}\right)_a - \left(\frac{dR}{dZ}\right)_d$	5×10^{-6} radians	15×10^{-6} radians
Surface Finish	RMS Roughness	5 - 15 A	15 - 20 A

Subscripts: a = actual, f = forward radius, d = design, r = rear radius, ϕ = angular position around circumference

mirrors and is a consequence of their small size. In practice this tolerance depends on the precision of the spindle used during the diamond turning and figuring processes and these proved to be more than adequate. The axial slope error was set at five microradians (1 arc second) and this proved difficult to meet. The final figuring was performed manually and the tendency was to remove material too quickly which, while correcting the slope, adversely affected the figure (sag). Because of program constraints, this deviation from the design requirement was accepted.

X-ray testing

All measurements of the grazing incidence relay optic telescope system performance in the X-ray regime have been conducted in the 89.5 meter vacuum facility at American Science and Engineering, Inc. An Advanced Metals Research X-ray source provides either a point source 30 micrometers in diameter (0.07 arc seconds) or a line source 100 micrometers in width and 1000 micrometers in length (0.2 x 2.3 arc seconds) which can be tilted with respect to the telescope optical axis to produce a 0.2 x 0.2 arc second spot. Since the 5.4 m effective focal length of the compound telescope is a significant fraction of the collimation tube length, the approximation of the laboratory source to a point source at infinity must be evaluated for each quantity measured. The effects of a finite source distance have significant implications for the point response function.

Telescope resolution on-axis

The point response function (PRF) of an optical system describes the radial dependence of the focused image of a point source at infinity. Experimentally, the PRF is derived from an Abel inversion of slit scan data obtained with proportional counters masked by 0.051, 0.254, and 1.270 mm wide slit windows and translated across the image plane. The counting rate of the image plane counter is normalized by comparison to the simultaneous counting rate of a cross-calibrated monitor counter masked with a circular, 0.321 cm^2 aperture and located directly in front of the telescope mirror.

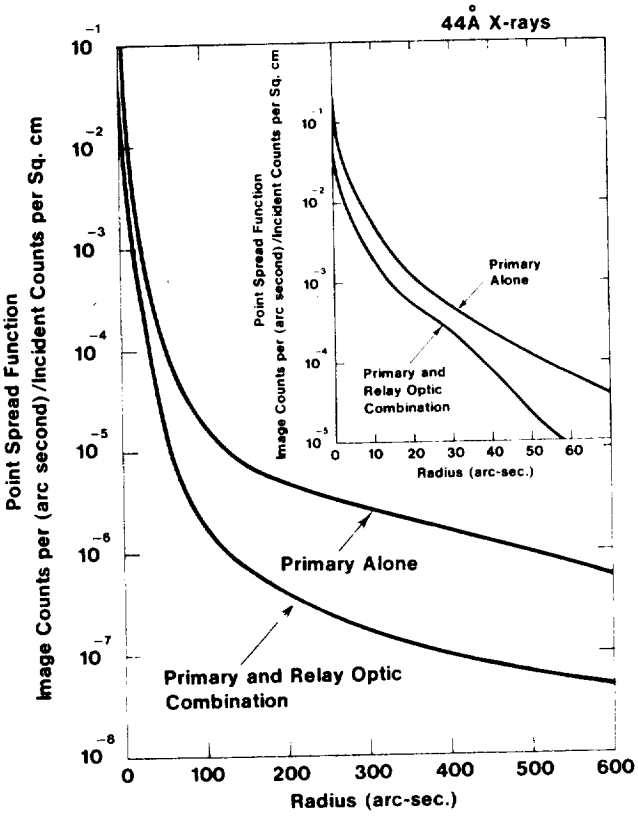

Figure 3. A comparison of the point response function of the compound telescope and the primary mirror alone at 44.5 A.

The compound telescope PRF of a 44.7 A (carbon K-alpha) source located on the axis of the optical system is presented in Figure 3. For comparison purposes the PRF of the primary mirror alone[2] is also plotted in Figure 3. The most significant effect of the addition of the secondary optic is a reduction in the overall efficiency of the system. The PRF is not degraded. In fact, the relative PRF of the compound telescope becomes more narrow than the primary mirror alone at radii greater than 35 arc seconds.

The negligible contribution of scattering from the secondary to the overall PRF has more to do with geometrical optics than with the quality of the secondary. An on-axis ray which undergoes a net scatter from the primary mirror of 1 arc second and is then specularly reflected by the secondary will intersect the compound telescope image plane 26 micrometers from the optical axis because the effective focal length is 5.37 m. An on-axis ray which is specularly reflected by the primary but which undergoes a net scatter from the relay optic of 1 arc second will intersect the image plane 3 micrometers (corresponding to one-ninth of an arc second) from the optical axis because the distance from the relay optic to the image plane is only 0.61 m. Therefore, at the image plane the scattering due to the secondary mirror is completely masked by the scattering due to the primary mirror.

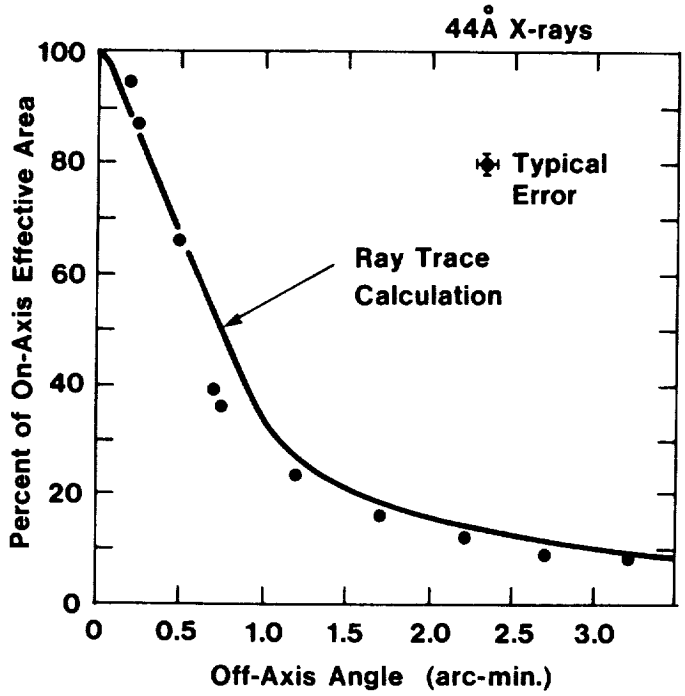

Figure 4. A comparison of the calculated and observed off-axis decline in energy throughput of the compound telescope, expressed as a fraction of the on-axis effective collecting area, for a 89.5 meter source distance.

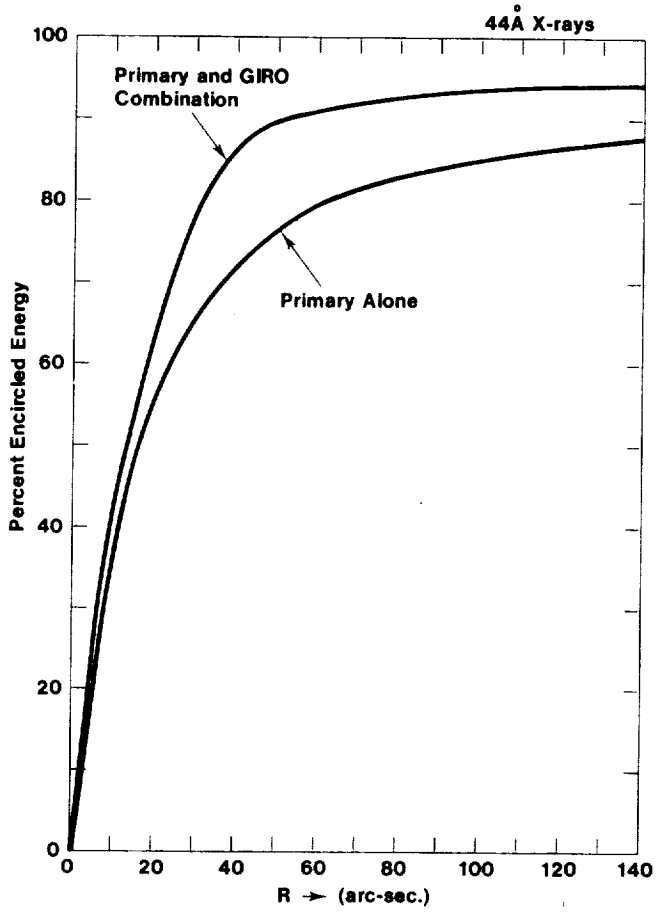

Figure 5. A comparison of the integrated point response function of the compound telescope and the primary mirror alone at 44.5 A.

The apparent narrowing of the compound telescope PRF at large scattering angles is due to vignetting of off-axis rays by the relay optic. The length of the hyperboloid mirrors of the relay optic were chosen to maximize on-axis resolution. Many off-axis rays which are reflected by the primary miss the reflecting surfaces of the secondary. A plot of the relative decrease in effective area with off-axis angle is presented in Figure 4. The solid line is a theoretical curve which is obtained from a ray tracing program which does not include scattering. The measured data points are obtained by removing the slit mask on the image plane proportional counter and rotating the optical bench of the telescope relative to the source. If the field of view is defined as the position where the effective area is 10% of its on-axis value, then the field of view of the compound telescope is restricted to a radius of 2.5 arc minutes.

Integration of the PRF in Figure 3 which yields the percent of total energy in the focal plane within a given radius of the optical axis is presented in Figure 5. The improvement in percent encircled energy of the compound telescope relative to the primary is due to vignetting of off-axis rays by the relay optic. Because of vignetting, rays at large scattering angles are lost so that a higher fraction of the rays that do reach the focal plane are close to the image center.

Vignetting of off-axis rays by the relay optic reduces the total energy throughput of the compound telescope relative to the primary alone. If the energy in the secondary focus image plane within a given radius of the image center were plotted as a fraction of the total energy in the prime focus image plane, each point of the Primary and GIRO Combination curve in Figure 5 would be reduced by a factor of 2.6 and the curve would asymptotically approach the value of 38.5%. Therefore, the improvement in the percent encircled energy of the compound telescope is achieved with a reduction in total energy throughput.

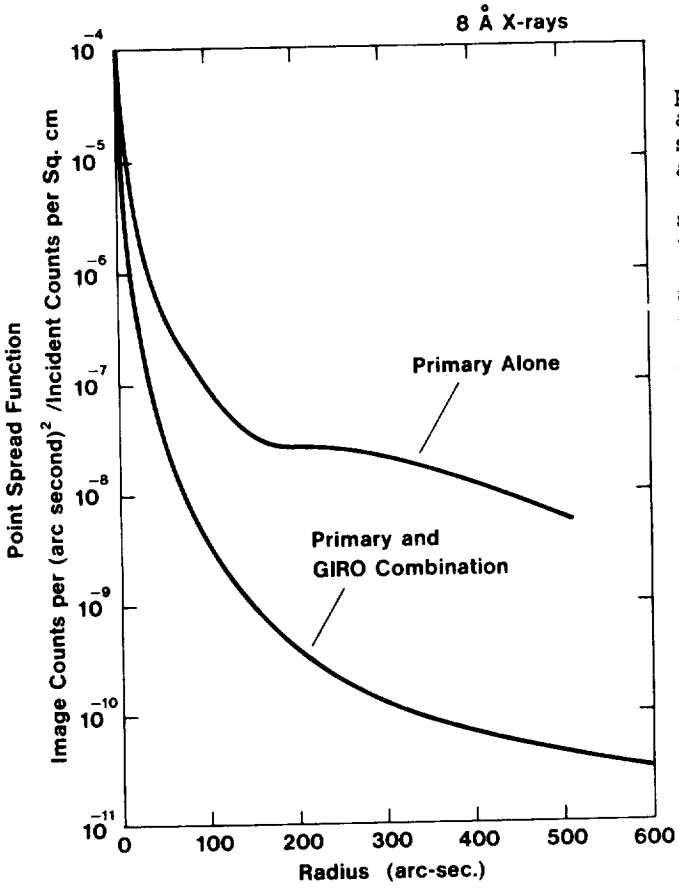

Figure 6. A comparison of the point response function of the compound telescope and the primary mirror alone at 8.3 Å.

At shorter wavelengths, the PRF of the primary mirror is distinguished from its PRF at 44.7 Å by an increase in the large angle scattering[2]. Because these scattered off-axis rays miss the relay optic, the 8.3 Å (aluminum K-alpha) PRF of the compound telescope presented in Figure 6 is similar to the 44.7 Å PRF of the compound telescope. Integration of PRFs of the compound telescope at both 44.7 A and 8.3 Å yield 50% encircled energy radii at 17 arc seconds. In contrast, the 50% encircled energy radii of the prime focus are 18 arc seconds at 44.7 A and 31 arc seconds at 8.3 Å.

Photographs of a pinhole array illuminated by a diffuse source provide another indication of the on-axis resolution of the compound telescope. A pinhole array with 1 arc second diameter pinholes on 2 arc second centers was illuminated with 44.7 Å X-rays from the defocused AMR source. The 6 pinholes which were illuminated are resolved. Although detailed film calibration and densitometry have not been conducted for these photographs, the film developing and printing were conducted in a manner consistent with that used in previous rocket flights.

Finite source distance effects and off-axis resolution

Geometrical ray tracing (without scattering) of the compound telescope image blur diameter for an on-axis point source as a function of source distance is presented in Figure 7. Because the optical elements of the relay optic were shortened to maximize resolution, the energy throughput of the compound telescope is very sensitive to the position of the relay optic. The calculations displayed in Figure 7 are constrained to maximize the energy throughput of the system by adjustment of the relay optic position. At object distances less than 600 m, the goals of zero blur diameter and maximum energy throughput become mutually exclusive and at object distances less than 100 m, it is impossible to achieve zero blur diameter with any relay optic position. Even at infinite source distance, the relay optic position for maximum energy throughput is slightly different from that for zero blur diameter although the resulting blur is small compared to the effect of scattering. While it has not been possible to experiment with different vacuum tube lengths to test these calculations, the experimentally determined relay optic position for maximum energy throughput in the 89.5 m facility corresponds to the 21 mm displacement from infinity focus position predicted by the calculations. The 1 arc second RMS blur diameter predicted by ray tracing for a 89.5 m source distance is significant in comparison to the 1 arc second half width-half maximum of the observed PRF.

All off-axis images of the compound telescope have some level of geometrical blurring which is greater in the direction perpendicular to the displacement of image from the on-axis point. The degree of the blur in the X and Y secondary focal plane directions for an image which is displaced in the X direction from the on-axis point is shown by the geometrical ray trace calculation presented in Figure 8. This aberration is independent of scattering and will limit the practical field of view for high resolution imaging to a 1.25 arc minute radius.

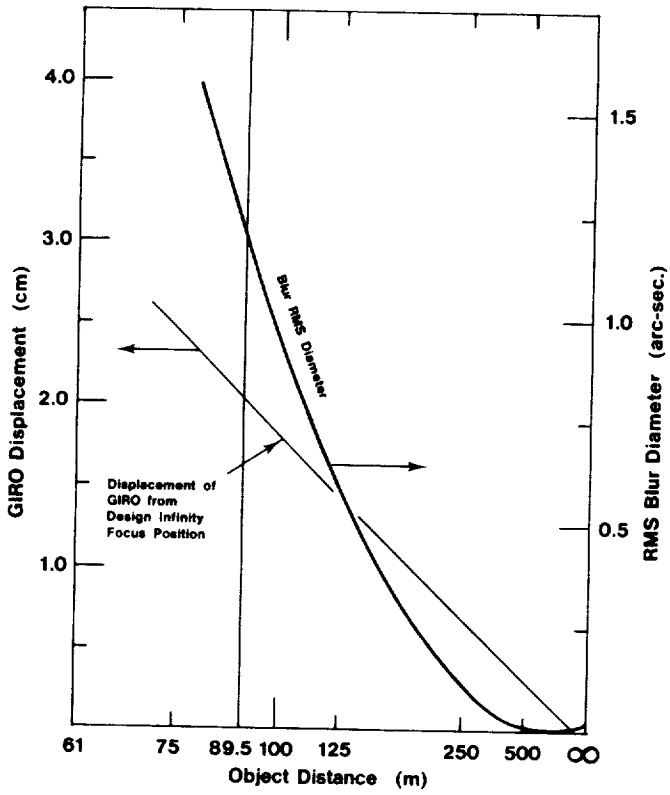

Figure 7. Ray trace calculation of the position of the secondary optic which maximizes the on-axis energy throughput and the resulting blur (not including scatter) for a range of source distances.

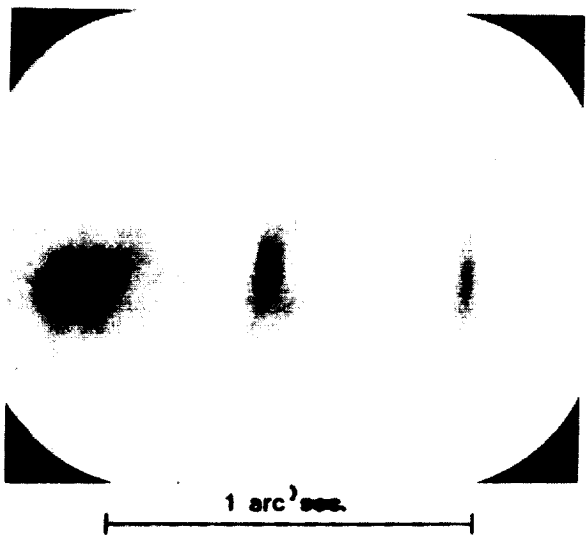

Figure 9. Photograph of X-ray source imaged by the compound telescope for the off-axis displacements (from left to right) of 0 arc seconds, 30 arc seconds, and 60 arc seconds.

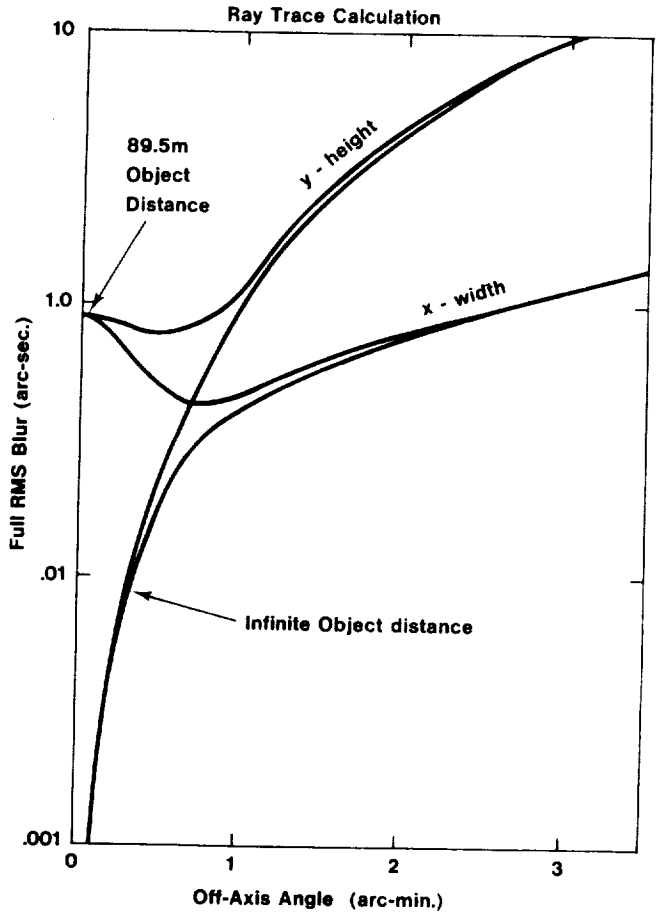

Figure 8. Ray trace calculations of blur (not including scattering) in the two dimensions of the compound telescope image plane for a point source off-axis in the in the X direction

Since the off-axis blur is not a circular intensity pattern, a slit scan along one axis is not sufficient to determine the response function. Accordingly, we used photographic X-ray photometry to measure the two-dimensional structure of the off-axis blur. A composite photograph of three exposures of a 44 Å X-ray source taken at the on-axis point, 30 arc seconds off axis, and 60 arc seconds off axis is presented in Figure 9. Although the tasks of film calibration and densitometry have not been completed at the time of this writing, the three exposures were taken on the same roll of film to the same level of monitor counts at the entrance aperture of the telescope and printed as a negative "sandwich" to eliminate any relative enhancements. Although the line source was utilized to generate a counting rate sufficient for reasonable exposures, the ratios of the height to width in the photograph agree with the ray trace calculation. The elongated geometrical blurring pattern is not obscured by scatter because the majority of the scatter seen in the image plane is due to scatter of the primary

(see above). Since the scattering angle is small (50% in less than 18 arc seconds), the rays scattered by the primary are subject to approximately the same aberration as those not scattered-yielding an overall X-Y asymmetry in the total blur.

Conclusion

The goal of increasing the plate scale of a soft X-ray solar telescope over that of previous optical systems while retaining a physical size less than 2 meters has been achieved with the use of a grazing incidence relay optic. The design and fabrication of the relay optic produced a system with on-axis resolution equal to that of the primary alone. However, the drawback of the compound telescope system is an increase in geometrical aberration and decrease in effective area with off-axis angle. Limits in field of view are 1.25 arc minutes in radius for 1 arc second resolution and 2.5 arc minutes in radius for acceptable effective area. Use of a CCD detector instead of photographic film reduces the problem of effective area because of the higher quantum efficiency of CCDs. Additionally, the larger plate scale of the compound telescope compensates for the larger pixel size of CCDs. It is anticipated that this system will provide a useful tool to study small scale structure in the solar corona.

Acknowledgements

It is a pleasure to acknowledge the help of the staffs of the Applied Optics Center and of Research Optics and Development, Inc., who participated in the fabrication of the secondary optic. We would also like to thank Alan DeCew who as both a consultant and as President of Research Optics and Development contributed to the development of the fabrication procedures. Tireless effort in gathering X-ray performance data was contributed by Daniel O'Mara of AS&E. The work was performed under NASA contract NAS5-25496.

References

1. J.M. Davis, A.S. Krieger, J.K. Silk and R.C. Chase, Proc. Soc. Photo-Opt.Instrum. Eng. 184 (1979) 96.

2. R.C. Chase, A.S. Krieger and J.H. Underwood, Appl. Opt. 21 (1982) 4446.

3. Fabrication was started at the Applied Optics Center, Burlington, MA 01803 USA. When the Burlington facility was closed, the work was transferred to Research Optics and Development, Inc., Waltham, MA 02154 USA.

4. Random Devices Inc., Newbury, Massachusetts 01950, USA.

4.17 The Plasma and Magnetic Field Properties of Coronal Loops Observed at High Spatial Resolution

D.F. Webb

American Science and Engineering, Inc.
Cambridge, Massachusetts 02139

and

Emmanuel College
Boston, Massachusetts

G.D. Holman

Laboratory for Astronomy and Solar Physics
NASA/Goddard Space Flight Center
Greenbelt, Maryland 20771

J.M. Davis

American Science and Engineering, Inc.
Cambridge, Massachusetts 02139

and

NASA/Marshall Space Flight Center
Huntsville, Alabama 35812

and

M.R. Kundu and R.K. Shevgaonkar

Astronomy Program
University of Maryland
College Park, Maryland 20771

THE ASTROPHYSICAL JOURNAL, 315:716–728, 1987 April 15

THE PLASMA AND MAGNETIC FIELD PROPERTIES OF CORONAL LOOPS OBSERVED AT HIGH SPATIAL RESOLUTION

D. F. WEBB
American Science and Engineering, Inc., Cambridge, Massachusetts; and Emmanuel College, Boston, Massachusetts
G. D. HOLMAN
Laboratory for Astronomy and Solar Physics, NASA Goddard Space Flight Center, Greenbelt, Maryland
J. M. DAVIS
American Science and Engineering, Inc.; and NASA Marshall Space Flight Center, Huntsville, Alabama
AND
M. R. KUNDU AND R. K. SHEVGAONKAR[1]
Astronomy Program, University of Maryland, College Park
Received 1986 May 22; accepted 1986 October 6

ABSTRACT

We compare coordinated, high spatial resolution observations obtained in 1979 and 1981 in soft X-rays in microwaves at 1.45 GHz (20 cm) and 4.9 GHz (6 cm) and with photospheric magnetograms, of six coronal loops. The loops were found to have plasma parameters typical of quiescent active region loops. Each loop had a compact microwave source with $T_b = 1$–2.5×10^6 K cospatial with or near the loop apex. Contrary to some interpretations, no complete loops (as determined by the X-ray observations) were imaged in microwaves. Model loops using the derived observational plasma and magnetic parameters are constructed, and the predicted distribution of thermal microwave emission compared with observations. The loop emission observed at 4.9 GHz is best described by fourth harmonic gyroresonance emission from a dipole loop model, but with less field variation along the loop than in the models of Holman and Kundu. The 1.45 GHz emission is likely to be free-free, since the X-ray loops are optically thick to free-free emission. The modeling results require the existence of an external plasma around the X-ray loops with a temperature of $\sim 10^5$ K or less. We are also able to deduce or place constraints on the magnetic field strengths within and their variations along the loops.

Subject headings: plasmas — Sun: corona — Sun: magnetic fields — Sun: radio radiation — Sun: X-rays

I. INTRODUCTION

High spatial resolution observations over more than a decade have revolutionized studies of active regions and coronal loops. In particular, microwave observations have revealed broad, diffuse areas coincident with plage emission and small, intense components associated with sunspot penumbrae and satellite spots, transverse fields over neutral lines or filaments (Kundu *et al.* 1977; Kundu, Schmahl, and Gerassimenko 1980), and emerging flux regions (Kundu and Velusamy 1980). Observations with the Very Large Array (VLA) have revealed looplike structures reminiscent of those observed in soft X-rays and EUV (e.g., Lang, Willson, and Rayrole 1982; Lang and Willson 1983; Kundu and Velusamy 1980), suggesting that some of this microwave emission arises in individual coronal loops.

Most of the coronal plasma in an active region is at high temperature (i.e., $T_e > 10^6$ K) and has its dominant emission in the soft X-ray regime (e.g., Webb 1981). In the radio regime, the slowly varying component of emission over active regions has a spectral maximum at centimeter wavelengths. Therefore, coordinated high-resolution observations in X-rays and microwaves can provide physical insights into coronal loop structures. The X-ray observations provide information on the three-dimensional distribution of plasma and the overall topology of the coronal magnetic field in a loop. The microwave observations provide details on the scale height, strength, and direction of the loop magnetic field and the relative contribution of magnetic and gas pressure, while photospheric magnetograms measure the strength of the field in the feet of the loop.

At low spatial resolution ($\sim 0'.5$), quiescent active region microwave emission has been interpreted as either thermal, low-harmonic gyroresonance (gr) emission associated with strong sunspot fields, or thermal bremsstrahlung from plage regions. Recent combined, high-resolution X-ray and microwave observations reveal a more complicated picture. Some observers (Chiuderi-Drago *et al.* 1982; Lang, Willson, and Gaizaukas 1983; Shibasaki *et al.* 1983; Strong, Alissandrakis, and Kundu 1984) have found good agreement between the X-ray and microwave observations and the accepted emission mechanisms for quiescent features. Others (Schmahl *et al.* 1982; Webb *et al.* 1983, hereafter Paper I; Kahler *et al.* 1984, hereafter Paper II) have observed significant differences between the detailed locations of these sources. We will emphasize that the detailed correspondence in active regions between X-ray and microwave emission is poor, and that a major problem with interpreting loop microwave emission is that this emission is often compact and restricted to the loop top.

Comparisons between models and observations of active region loops have been inconclusive because of the lack of high spatial resolution data at different wavelengths and information on the three-dimensional structure of the magnetic field in the corona. Recently, comparisons have been attempted between X-ray, EUV, and radio observations of loops and

[1] Also Indian Institute of Astrophysics, Bangalore.

static loop models, but these suffered from either a lack of high-resolution radio data (e.g., Pallavicini, Sakurai, and Vaiana 1981) or a lack of simultaneous X-ray or EUV and microwave data (e.g., McConnell and Kundu 1983). Our results demonstrate the importance of simultaneous high spatial resolution microwave and soft X-ray (and EUV) observations for the testing and refinement of coronal magnetic loop models.

This paper is the third of a series studying the detailed plasma and magnetic field properties of active region loops, with the goal of constraining models of the structure and heating of active regions. The first two papers (Paper I and Paper II) described combined soft X-ray rocket and 6 cm VLA observations on 1979 November 16 and 7 respectively and were primarily observational. In this paper we first describe new results from the comparison of a third set of X-ray rocket and 20 cm VLA observations of an active region on 1981 February 13, and then analyze six loops from these data sets observed to have significant cospatial soft X-ray and microwave emission. Based on this set of observations and the dipole loop models of Holman and Kundu (1985), we then construct model loops and compare the predicted distribution of thermal microwave emission with observations.

In the next section we describe the comparative analysis of the 1981 February 13 observations of Hale region 454 and briefly review the analysis and results from Paper I of the two active regions observed on 1979 November 16. In § III we discuss the derivation of the plasma and magnetic properties of the six loops observed on these two dates to have cospatial soft X-ray emission and microwave sources. Comparison of these data with the loop models are described in § IV, and the results are summarized and discussed in the last section.

II. COMPARATIVE ANALYSIS OF ACTIVE REGIONS

a) 1981 February 13 Observations and Results

i) *Observational Data*

Instrumental details of the AS&E rocket payloads have appeared in Kahler, Davis, and Harvey (1983) and Webb and Davis (1985). The 1981 February 13 flight payload utilized the fused-quartz grazing-incidence mirror, four different filters (with bandpasses over the range 8–65 Å), a moderate-speed film emulsion (SO-212), and a fine-grain emulsion (SO-253). Full-disk X-ray coronal images with an on-axis spatial resolution of $\sim 2''$ were obtained between 1916 and 1921 UT. Examples of these images are shown in the aforementioned papers.

Radio observations were made with the VLA of the National Radio Astronomy Observatory[2] between 1600 and 2330 UT. Twenty-six antennas were available in the B-configuration during the observations, providing good UV coverage. The system was sensitive to structures smaller than 1'.5 because the shortest spacing used for these maps was $\sim 2000\lambda$. Observations were obtained at 4.9 GHz (6.1 cm) and 1.45 GHz (20.75 cm), and the phase center for continuous tracking was N11W37 at 1915 UT. This was centered on one of the leading sunspots in Hale region 454. A reliable synthesized map of total intensity at 1.45 GHz was produced with a synthesized beam of $4''.7 \times 4''.7$. Unfortunately, reliable 5 GHz maps and polarization data at both wavelengths were not obtained because the sources were not bright enough at 5 GHz. The observing procedure, calibration, and cleaning methods were similar to that of McConnell and Kundu (1983).[3]

A full-disk photospheric magnetogram was obtained at the National Solar Observatory[4] (NSO)–Kitt Peak at 1507 UT, and a video magnetogram at Big Bear Solar Observatory (BBSO) at 2009 UT. (It was cloudy at BBSO earlier in the day.) We obtained contour plots and printouts of the NSO magnetogram for use in the analysis. A high-resolution Hα image of H454 was obtained at BBSO at 2008 UT. A cine version of the daily full-disk Hα patrol film from 1428 to ~ 2000 UT was obtained from NSO–Sacramento Peak Observatory and used to study the evolution of the active centers on this day.

The X-ray and visible light images, the microwave map, and the magnetogram were co-aligned and compared in the same manner as discussed in Papers I and II. Briefly, the major sunspots in H454 were used to co-align the X-ray image, the 20 cm map and the magnetograms. The alignment accuracy was within $\sim 10''$.

ii) *Comparative Results*

Since we are interested in studying only the quiescent features of the active region corona, each radio map was synthesized from several hours of observations which excluded periods with fluctuations exceeding $\sim 10\%$ of the total intensity signal (i.e., bursts). Therefore, flarelike periods were excluded, but not necessarily slower or evolutionary changes in the active region. In addition, the 1.45 GHz beam included nearly the full Sun, so that contributions to the signal from activity in distant regions were possible.

For the two active regions studied on 1979 November 16 (Paper I), we are confident that the data were obtained during a quiescent period. However, this was not the case on 1981 February 13, when there were three main active region complexes on the Sun: H454 in the northwest, H461/67 in the northeast, and H465 in the southeast. All these regions were active during the VLA observing period, with flares sometimes occurring nearly simultaneously in two or three of the regions. To aid in identifying this activity, we examined Sagamore Hill Radio Observatory fixed-frequency records from 1600 to 2000 UT, NOAA *GOES* plots and lists of X-ray events, and Solar Geophysical Data (SGD) lists of Hα flares and radio bursts (SGD 1981).

The evolution of H454 is important to an understanding of the X-ray observations. H454 was a new region that appeared at the east limb on February 4 on the trailing side of H391. It grew steadily in area and complexity. On February 13 it had roughly equal areas of east-west plage and contained 41 sunspots balanced between polarities (SGD 1981). There were three large spots: two separate symmetrical, positive-polarity spots, and one large negative spot complex. This large spot had peak fields exceeding 2100 G and an area of 1000 millionths of a solar hemisphere.

[2] NRAO is operated by Associated Universities, Inc., under contract with the National Science Foundation.

[3] Radio interferometric observations of H454 were also obtained at Owens Valley Radio Observatory (OVRO) at 10.6 GHz (2.8 cm) (Hurford 1986). A single strong, unresolved source ($T_b \gtrsim 10^5$ K) was detected at a location of 137 north and 542" west of Sun center in celestial coordinates. The source was $\sim 50\%$ circularly polarized and cospatial with the largest sunspot in H454. Its high polarization, intensity, and position over the strong spot fields are consistent with low harmonic, gr emission. Because this source was not detected at 1.45 GHz nor associated with X-ray emission, we will not discuss it further.

[4] NSO is a facility of National Optical Astronomy Observatories, which is operated by the Association of Universities for Research in Astronomy, Inc., under contract with the National Science Foundation.

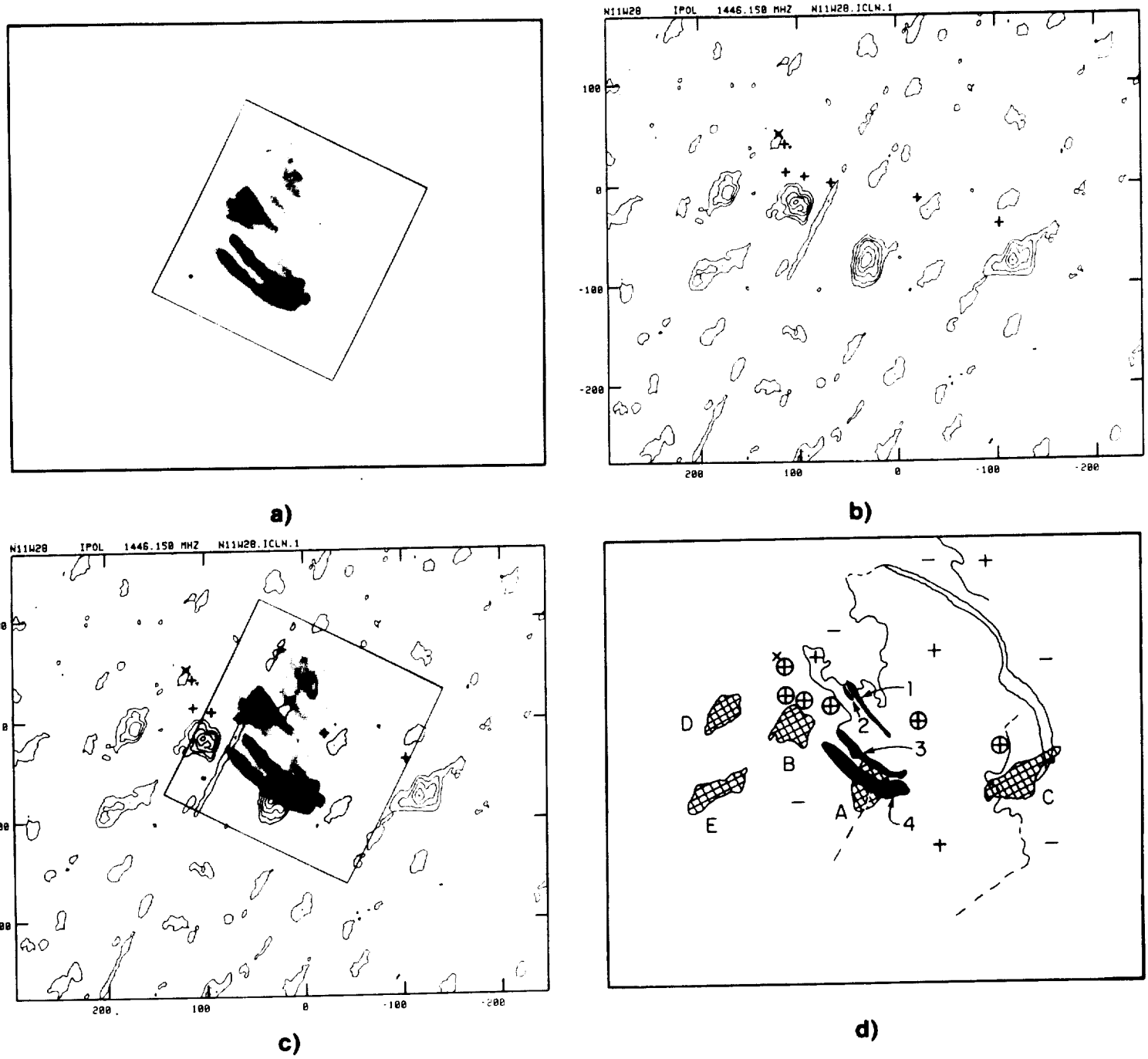

FIG. 1.—Co-aligned, high-resolution images (*a*) in soft X-rays and (*b*) at 1.45 GHz (20 cm) of active region H454 on 1981 February 13. The X-ray image is an "edge-enhanced" digitized image of a 20 s exposure on Kodak SO-253 emulsion obtained at 1920 UT. The edge-enhancement program, described in the Appendix of Kahler, Webb, and Moore (1981), essentially filters out low spatial frequencies, yielding enhanced images of coronal structures. Solar north is to the upper right parallel to the border of the X-ray image, and east is to the upper left. The 1.45 GHz VLA map is oriented with celestial north up and east to the left. The scale unit is 100″. The map is in total intensity with a synthesized clean beam of 4″.7 × 4″.7. The phase center (0, 0) of the map was at 661″ west and 87″north of disk center at 1915 UT. The lowest contour and the contour interval are 1.72×10^5 K. The plusses (circled on the schematic) denote the centroids of six major sunspots (Fig. 4*b*). The cross marks the location of the single strong source observed at 10.6 GHz (see text). (*c*) An overlay of the X-ray and radio images. (*d*) A schematic drawing of the salient features from co-aligned X-ray, 20 cm radio, photospheric magnetogram, and Hα images. The brightest X-ray loops are denoted by numbers. The five 1.45 GHz sources with two or more contours are cross-hatched and denoted by letters. The thin solid and dashed lines are our estimate of the positions of the photospheric inversion lines separating opposite magnetic field polarities. We have drawn the outline of a long Hα filament bordering the region to the northwest.

Figure 1 shows for H454 (*a*) a high-resolution, digitally enhanced soft X-ray image, (*b*) the $7\frac{1}{2}$ hr synthesis 1.45 GHz VLA map in total intensity, (*c*) the overlay of these two images, and (*d*) a schematic diagram relating the salient features from all the observations. The pluses on the 20 cm map and the circled pluses on the schematic denote the centroids of six major sunspots in the region (see Fig. 3*b* below—the large negative spot had a double umbra). The schematic drawing compares the locations of the brightest 1.45 GHz (and single 10.6 GHz) sources with the brightest X-ray loop, our estimate of the location of the photospheric inversion line(s), and the photospheric magnetic field polarities, both from the Kitt Peak magnetogram at 1507 UT.

As observed in Figure 1*a*, the dominant X-ray emission was confined to generally east-west-directed loops spanning the negative (east) and positive (west) bright plage areas between the eastern negative and middle positive spots (Fig. 1*d*). The northern loop systems, including the shorter, bright loop systems 1 and 2 in the center of the region, did not change during the rocket observations. However, the long southern loops, labeled "3" and "4" in Figure 1*d*, did evolve during this period. Since these loops are the subject of our comparison with 1.45 GHz emission in the next section, we examine this evolution more closely.

Figure 2 shows the NOAA *GOES* 1–8 Å and 0.5–4 Å soft X-ray flux plots around the period of the rocket flight. Two major events are evident starting at 1910 and 1933 UT. The first event involved a compact Hα flare and surge in H454 that was homologous with an earlier Hα event at ~1700 UT. It occurred in the northern penumbra of the large spot. This subflare appeared in the rocket images during its decay as a small, bright X-ray kernel which faded at 1918 UT. The images used in our quantitative analysis were obtained at about 1917 and 1919 UT and were not affected by this tiny flare.

After about 1920 UT, nearly simultaneous events occurred in the southeast region H465 and in H454. The relatively long duration *GOES* X-ray signature commencing at 1933 UT was probably dominated by an Hα flare and mass ejection from H465. However, the SGD only listed a 1N flare in H454 with an onset at 1929 UT and a maximum at 1938 UT. The Hα movie revealed that the flare commenced about 1920 UT in the plage at the feet of the large southern X-ray loops 3 and 4. The X-ray image in Figure 1a was obtained at 1920 UT and shows the west foot of loop 3 brightening. This area did not appear in the earlier images that were used in our analysis. Therefore, we believe that the results of our X-ray analysis of those loops are representative of a fairly quiescent but preflare state of the loops.

To improve our understanding of the plasma and magnetic field properties of coronal structures, we need to identify emission at both X-ray and microwave wavelengths arising from the same volume of a coronal structure. However, as in the only previous studies involving simultaneous X-ray and microwave (5 GHz) observations at high spatial resolution (Paper I and Paper II), we find that the X-ray emission was generally not associated with the 1.45 GHz microwave sources. Only one of the five 1.45 GHz sources (source A, Fig. 1) was cospatial with X-ray emission.

Table 1 lists the brightest 1.45 GHz sources as designated on Figure 1*d* in decreasing order of peak brightness temperature T_b. To be considered, a source had to contain at least two contours; the other features on the map may be noise or artifacts of the CLEANing process. For each source in Table 1 we

TABLE 1

BRIGHTEST 1.45 GHz SOURCES IN ACTIVE REGION H454

Source	Peak T_b (10^5 K)	Size*	Association
A	8.6–10.3	22″ × 38″	Top of coronal loop arcade; photospheric neutral line
B	8.6	22 × 32	Large sunspot umbra or penumbra; near feet of coronal loops
C	8.6	20 × 35	Photospheric neutral lines/filament; sunspot
D	5.2–6.9	15 × 30	? (Faint Hα plage)
E	3.4	5 × 30	?

* The approximate FWHM dimensions of the total intensity along the short and long axis of each source. These are uncorrected for the beam shape.

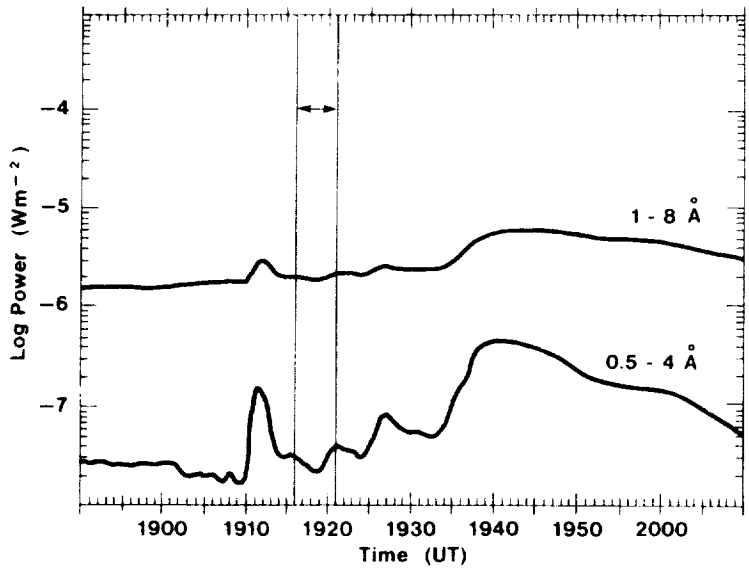

FIG. 2.—NOAA *GOES2* satellite whole-Sun soft X-ray flux evolution around the time of the rocket flight on 1981 February 13. Plots from both the softer (*top*) and harder (*bottom*) channels are shown. The period of the rocket flight is denoted by the arrows. Date courtesy of S. Kahler, Emmanuel College.

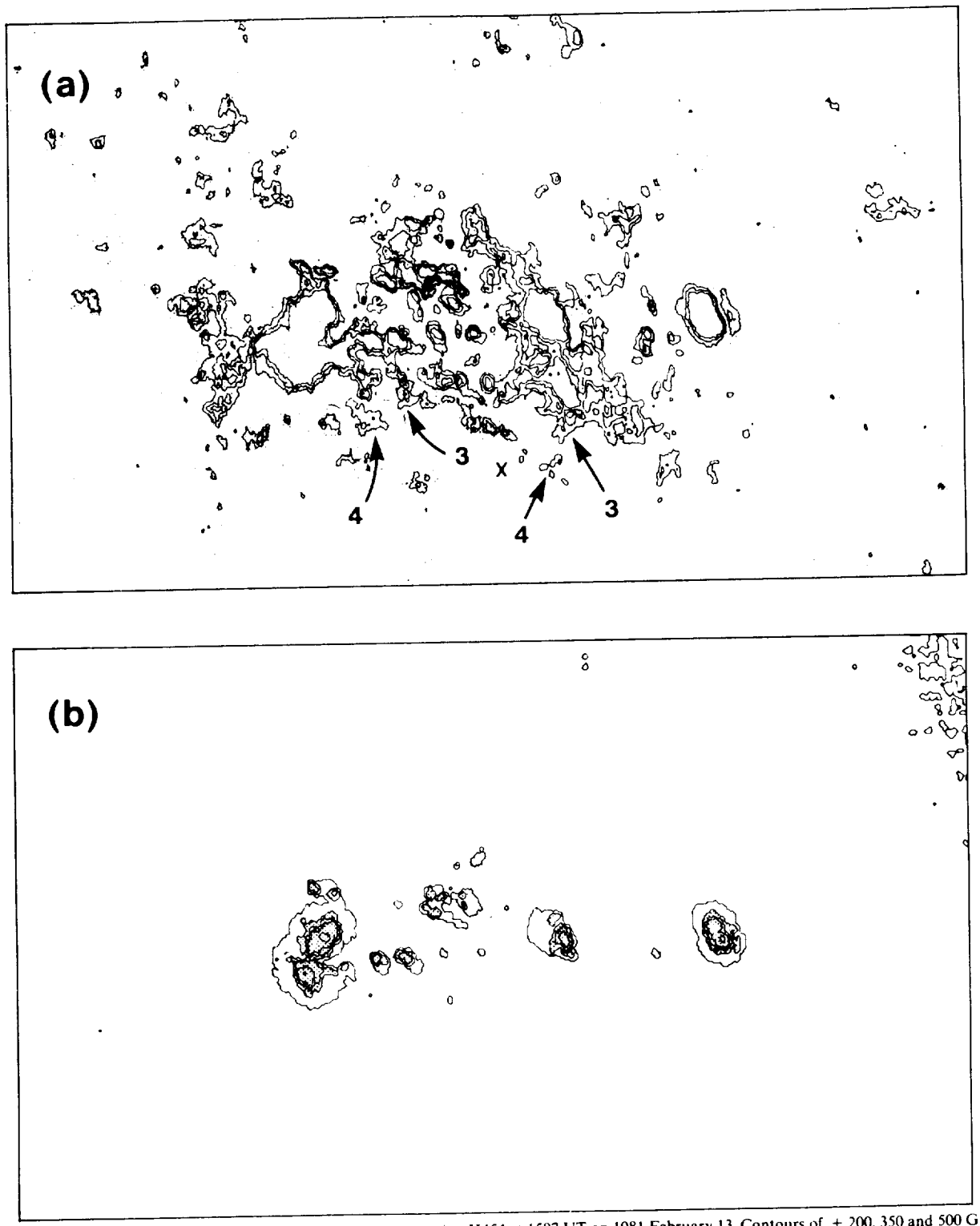

FIG. 3.—Contour map of the photospheric magnetic field in active region H454 at 1507 UT on 1981 February 13. Contours of ± 200, 350 and 500 G are shown. Negative fields are shaded; fields less than − 50 G are shown without contours. The numbered arrows point to the locations of the footpoints of X-ray loops 3 and 4 (see Fig. 1). The cross denotes the position of the peak 1.45 GHz emission from source A. (*b*) Co-aligned white light continuum contour map showing locations of the sunspots in H454. Solar north is up and east to the left. The horizontal dimension of the boxes is 8'.5. Data courtesy of J. Harvey, NSO (Kitt Peak).

also list its size and possible physical association in the manner of Paper I.

Source A was one of the brightest and largest 1.45 GHz sources and was positioned at or near the apex of the bright sourthern X-ray loops (Fig. 1*c*). Source A also overlaid an area of moderate Hα plage and was near a bend in the photospheric inversion line. But this area of the photosphere generally had magnetic fields of low strength and low gradients. Figure 3 presents Kitt Peak contour maps of (*a*) the photospheric magnetic field and (*b*) sunspots in H454 on 1981 February 13. The "X" in Figure 3*a* denotes the center of source A, and the arrows point to the locations of the feet of X-ray loops 3 and 4.

Source B was a strong, circular source lying near the eastern foot of loop 4. It overlaid an area of weak negative polarity field without bright Hα emission. The center of the source was only 25″–30″ from the southern umbra of the large spot. Given the alignment uncertainty and the possibility of projection effects, it might have been associated with the corona above this umbra or with the penumbra.

The elongated source C lay 40″ west of the westernmost positive spot in an area of no Hα activity and moderate magnetic field strength. The source straddled the inversion line, an area of high field gradients, and the southern end of a long-curving filament which formed the region to the west. Projection effects would be significant for this coronal source. Both sources D and E lay in areas of weak negative polarity field, with only faint Hα plage and no activity. No magnetic pores or spots existed in these areas (see Fig. 3*b*). The reality of source E was questionable.

Finally, we note that 1.45 GHz emission was *not* detected over regions where we might have expected it based on previous results. With the possible exception of source B, no emission was detected near sunspots or other strong fields where gr emission might be expected. And other than source A, no 1.45 GHz emission was associated with the X-ray loops, the flare-active area to the northeast, nor any bright Hα plage regions. Such associations have been emphasized by Lang, Willson, and Rayrole (1982), Lang, Willson and Gaizaukas (1983), and Chuideri-Drago *et al.* (1982), based on the expected dominance of bremsstrahlung radiation at 1.45 GHz. But even the associated source A did not resemble the size or shape of the X-ray loops.

b) Review of 1979 November 16 Results

Here we briefly review the main results of Paper I to provide the background necessary for the derivation of loop parameters in the next section. That study was based on a determination of the spatial correspondence in two active regions of the most intense sources of 5 GHz emission to coronal loop structures, sunspots, chromospheric structures, and photospheric magnetic fields. Some of the fanter microwave components were associated with X-ray (bandpass of 3 $\sim$60 Å) loops, but the brighter components were not. Also, most of the bright 6 GHz sources were *not* associated with sunspots. In both Paper I and Paper II, the X-ray and magnetic field observations were used to constrain possible mechanisms for the centimeter radio emission.

Those authors found that free-free emission did not provide sufficient opacity to explain the 5 GHz sources (for which $T_b > 10^6$ K). Gyroresonance absorption at the third or fourth harmonic (requiring magnetic fields of 450 or 600 G; Paper I) or at the fourth or fifth harmonic (fields of 360 or 450 G, Paper II) could explain some but not all of the emission. However, in both studies, a nonthermal mechanism was proposed to explain sources of intense emission (not associated with sunspots). This result suggests that discrete regions of continuous particle acceleration might be common in active regions, an unexpected result with potential importance to theories of loop heating.

On 1979 November 16 about one-third of the 5 GHz sources in both active regions were cospatial with the feet or upper parts of coronal loops of lengths 5×10^4 km or less. These loops were either inferred from the geometry of the magnetic field or detected directly in soft X-rays. However, only four of the loops had both cospatial X-ray and 5 GHz emission from near the top of the loop. These are summarized in Table II of Paper I and are shown here schematically in Figure 4 superposed on the VLA intensity maps. Only the microwave sources cospatial with the four X-ray loops and the sunspot locations are labeled on Figure 4. Such emission clearly arises from the lower corona. Based on the assumption that the emission in the two wavebands arises from the same volume, direct tests of microwave emission mechanisms and derivation of loop parameters, such as temperature gradients and magnetic field structure, can be made.

The two loops of interest in region H421 are shown in Figure 4*a*. The weak source E′ was cospatial with the top of a short, bright X-ray loop. This loop bridged the main inversion line of the region in an area of high field gradient near a large sunspot (the plus). The western foot ended in or near the spot penumbra and the eastern foot was cospatial with strong ($T_b \approx 4.8 \times 10^6$ K) source E. Because source E was compact and cospatial with a magnetically complex area, we could not unambiguously associate it with the X-ray loop and will not discuss it further. The length of ($\sim 2 \times 10^4$ km), shape, and location of the X-ray loop were typical of penumbral coronal loops (Webb and Zirin 1981). North of the spot lay a classic arcade structure with X-ray loops joining opposite polarity plage divided by a weak Hα filament. The X-ray loop drawn on Figure 4*a* was the largest diffuse arch forming the northern limit of the arcade. Cospatial with or just above the arch was the microwave source H. This source was bipolar and weakly polarized with a peak $T_b \approx 2.5 \times 10^6$ K. There were no microwave sources at the feet of the X-ray arch.

The two loops of interest in region H419 are shown in Figure 4*b*. The most interesting was a long, thin X-ray loop whose top was apparently fainter than its feet. Cospatial with the loop top was source M, a broad, weak microwave source with moderate polarization. Again there were no sources at the footpoints. Finally, just south of the largest sunspot in H419 lay a bright, triangular-shaped area of X-ray emission associated with Hα fibrils and multiple, elongated sources, all of which were labeled source J. The north-south orientation of the radio emission, the X-ray structure, and the Hα fibrils suggested that the emission was associated with an arcade of low-lying loops crossing the inversion line with their northern feet possibly in the penumbra. This source also showed significant polarization.

III. DERIVATION OF LOOP PARAMETERS

In this section we derive the pertinent coronal plasma parameters for the six X-ray loops observed (on the rocket images of 1979 November 16 and 1981 February 13) to have cospatial microwave sources at the loop top. We then use these parameters to interpret the microwave emission in terms of the thermal emission mechanisms (free-free or gr emission). For

the two flights, pairs of adjacent exposures through beryllium and aluminized polypropylene filters were converted to digitized arrays of film density. These arrays were obtained at 1702–1703 UT on 1979 November 16 and 1917–1919 UT on 1981 February 13. To determine plasma parameters of the X-ray loops, the density arrays were calibrated and reduced to arrays of energy flux at the film plane following procedures discussed by Vaiana *et al.* (1977) and modified by Davis and Webb (1985) for the rocket data. For the 1979 data we used the same laboratory calibrations at 8.3 and 44 Å of the SO-212 film used in Paper II, whereas for 1981 we used the modified procedure discussed by Davis and Webb (1985).

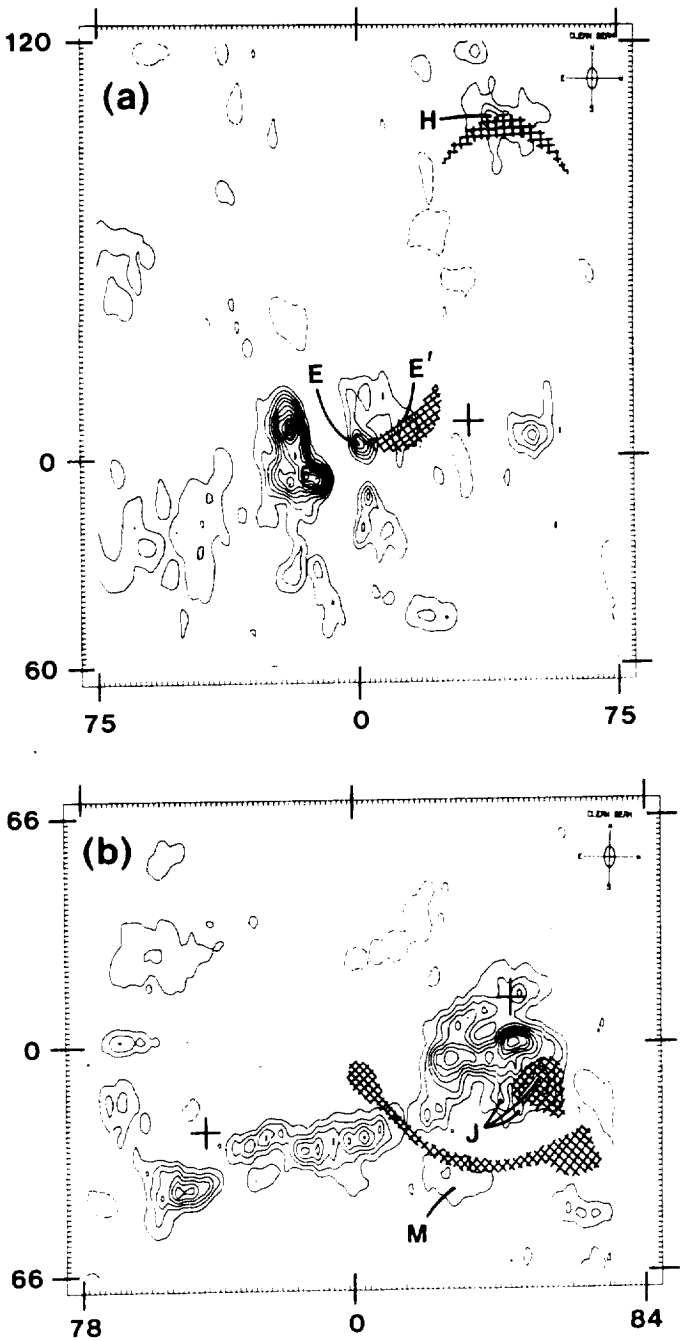

FIG. 4.—VLA intensity maps at 5 GHz (6 cm) of active regions (*a*) H421 and (*b*) H419 on 1979 November 16. The size of the synthesized beam was 6″ × 3″, shown in the upper right. Celestial north is at the top and east to the left. The phase centers (0, 0) of the two maps were N10W23 and N32W33 heliocentric for H421 and H419 respectively, at 00 UT. The scale units are in arcseconds. On both maps the lowest contour and the contour interval are 8×10^5 K. Large sunspot locations are denoted by plusses. The four X-ray loops with associated 5 GHz sources are overlaid and cross-hatched on the maps, and the microwave sources are labeled with letters. See text for details. This figure was adapted from Figs. 1–3 of Paper I.

The X-ray images on the two flights were obtained with two different mirror systems, a Kanigan metal mirror on 1979 November 16 and the fused silica mirror in 1981. These mirrors have different characteristics, but both yield image-plane pixel sizes of ~3″. The mirrors also have different scattering characteristics. This scattering is characterized by point spread functions which are used to produce deconvolved energy flux arrays. These arrays were then used to obtain maps of electron temperature and linear emission measure, both integrated along the line of sight.

Table 2 summarizes the derived X-ray, microwave, and photospheric magnetic data for the six X-ray loops. Columns (3)–(6) list the plasma quantities of the loops derived from the X-ray arrays. The listed errors are those due to film calibration and do not directly include errors due to deconvolution of the spread functions. This latter factor might yield uncertainties in absolute values as great as 50%, especially for the 1979 data. Because of apparent brightness differences along each loop, these parameters were averaged over the eastern and western parts of the 1981 loops, and in 1979 over the bright loop cores near their apices and along the entire loops. Despite the brightness gradients, we see that within loop segments the actual differences in emission measure, density, and temperature were small. The electron temperatures and densities all lay within ranges typical of quiescent coronal active region loops (e.g., Webb 1981). For each flight the brightness differences between loops were due mostly to density differences, not temperature differences, as also reported before (e.g., Davis *et al.* 1975; Cheng 1980). Within the uncertainties each loop was isobaric and isothermal, at least along their axes.

Following Papers I and II, we can use the X-ray loop parameters to estimate the importance of thermal bremsstrahlung to the microwave emission. The free-free optical depth is (cf. Lang 1980)

$$\tau_{\rm ff} = \frac{9.8 \times 10^{-3} \ln (4.7 \times 10^{10} T_e \nu)}{\nu^2 T_e^{3/2}} \int n_e^2 \, dl \, ,$$

where ν is the frequency of radio observations, and the electron parameters are obtained from the X-ray measurements. For these conditions at 4.9 GHz (1979 data), the corona is optically thin ($\tau_{\rm ff} \approx 0.01$–$0.06$) and $T_b(\rm ff) = \tau_{\rm ff} T_e$. The calculated $T_b(\rm ff)$ (col. [7]) is factors of 10–50 too low to account for the observed T_b at the loop top (col. [8]). At 1.45 GHz (1981 data), the corona is optically thick ($\tau_{\rm ff} \approx 2.8$–$4.5$) and $T_b(\rm ff) = T_e(1 - e^{-\tau_{\rm ff}})$. For these conditions the calculated $T_b(\rm ff)$ is about a factor of 2.5 *greater* than the observed T_b for source A, and optically thick bremsstrahlung is a viable emission mechanism.

Average values for the photospheric magnetic field at the loop footpoints estimated from the NSO contour maps are given in the last column of Table 2. The X-ray loops cospatial with sources H421-E′ and H419-J each might have had one foot in a spot penumbra where kG fields are possible. Thus significant longitudinal field gradients were possible in these loops; indeed, these loops were among the brightest in their respective active regions. The fields at the other loop feet (a few hundred G) are typical of plage fields.

TABLE 2

DERIVED PARAMETERS FOR X-RAY LOOPS WITH MICROWAVE SOURCES

Source or Loop (1)	Region (2)	$\int N_e^2 dl$[a] (10^{28} cm^{-5}) (3)	Δl[b] (10^8 cm) (4)	N_e[c] (10^9 cm) (5)	T_e[d] (10^6 K) (6)	T_b(ff)[e] (10^6 K) (7)	Peak T_b(obs)[f] (10^6 K) (8)	Polarity[f] (9)	Percent Polarity[g] (10)	Footpoint B[h] (G) (11)
				1979 November 16						
H421-E'	Core	3.9 ± 0.3	6.5	7.8 ± 0.2	3.0 ± 0.2	0.15	1.5	L	...	50–200 East
	Loop	3.6 ± 0.3	6.0 ± 0.8	7.8 ± 0.8	2.9 ± 0.3	0.15				< 1000 West
H421-H	Core	4.2 ± 0.4	8.7	6.9 ± 0.3	2.8 ± 0.2	0.17	2.5	R	33%	350–500
	Loop	3.4 ± 0.2	13 ± 4.2	5.4 ± 1.1	2.9 ± 0.2	0.14				
H419-M	Top	0.74 ± 0.06	7.0 ± 1.8	3.4 ± 0.6	2.9 ± 0.2	0.03	1.5	R	50	50–200
H419-J	Core	2.5 ± 0.2	(10)	(5.0 ± 0.2)	3.0 ± 0.2	0.10	1.5–2.5	R	33–100	> 500
	Loops	2.2 ± 0.2	(10)	(4.7 ± 0.2)	3.0 ± 0.2	0.09				< 1000
				1981 February 13						
3	East	21 ± 8.8	7.0	17 ± 3.8	2.5	2.5	0.9–1.0	...	...	300
	West	20 ± 8.4	3.5	23 ± 5.2	2.4	2.4		...	...	
4	East	14 ± 6.0	8.7	13 ± 2.8	2.6	2.4	...	...	...	250
	West	15 ± 6.4	(12)	(11 ± 2.4)	2.4	2.3		...	...	

[a] Integral emission measure along the line of sight (LOS). Errors are uncertainties due to the film calibration.
[b] Loop thickness along the LOS estimated from the loop width on the fine-grain SO-253 film. Quantities in parentheses are less reliable.
[c] Electron density derived by dividing the emission measure by Δl.
[d] Electron temperature along the LOS from two-filter method. Errors are uncertainties due to the film calibration.
[e] For 1979 values, average brightness temperature due to optically thin thermal bremsstrahlung calculated from X-ray parameters; for $\nu = 4.9$ GHz. For 1981 values, $T_b = T_e(1 - e^{-\tau_\nu})$ because at 1.45 GHz and with these X-ray parameters corona is optically thick.
[f] From Paper I, Table II.
[g] From Paper I, Table I.
[h] Average photospheric magnetic field strength estimated from magnetogram contour maps (e.g., Fig. 3).

Following Kundu, Schmahl, and Gerassimenko (1980) and Papers I and II, curves of unit optical depth are plotted in Figure 5. Figure 5*a* is for an observation frequency of 4.9 GHz, and Figure 5*b* is for 1.45 GHz. The pairs of curves running from upper left to lower right are for second to fifth harmonic, extraordinary mode gr absorption. The lower (*dashed*) curve of each pair is for an angle $\theta = 60°$ between the line of sight and the magnetic field, while the upper (*solid*) curve is for an angle of 30°. The curves are computed from the absorption coefficients given by Takakura and Scalise (1970).

In computing the optical depth, the scale length for variation of the magnetic field, $L_B = B/(dB/dl)$, was assumed to be 1×10^9 cm. This is consistent with estimates from magnetic field models (Kundu, Schmahl, and Gerassimenko 1980; Schmahl *et al.* 1982; McConnell and Kundu 1983) and with the sizes of observed X-ray loops. The curves vary as $L_B^{1/(1-s)}$, where s is the harmonic number, and, therefore, the higher harmonics are not very sensitive to small changes in the value of L_B. The short-dashed curves represent unit optical depth for free-free absorption when the density scale length (or loop thickness) is 1×10^9 cm. A source is optically thick to gr absorption if it lies above and to the right of the appropriate curve, and to free-free absorption if it lies below and to the right of the dotted curve. Also shown are the electron densities corresponding to the plasma frequency (*vertical line*). Gyroresonance emission is suppressed in the vicinity of and to the right of the plasma frequency line.

The small rectangles in Figures 5*a* and 5*b* encompass the range of electron temperatures and densities deduced from the X-ray observations for the six loops. Free-free emission should be an important contributor to the microwave emission of the loops observed at 1.45 GHz, since the X-ray loops are optically thick to free-free absorption. Gyroresonance emission may also have contributed to the 1.45 GHz source, but it is likely

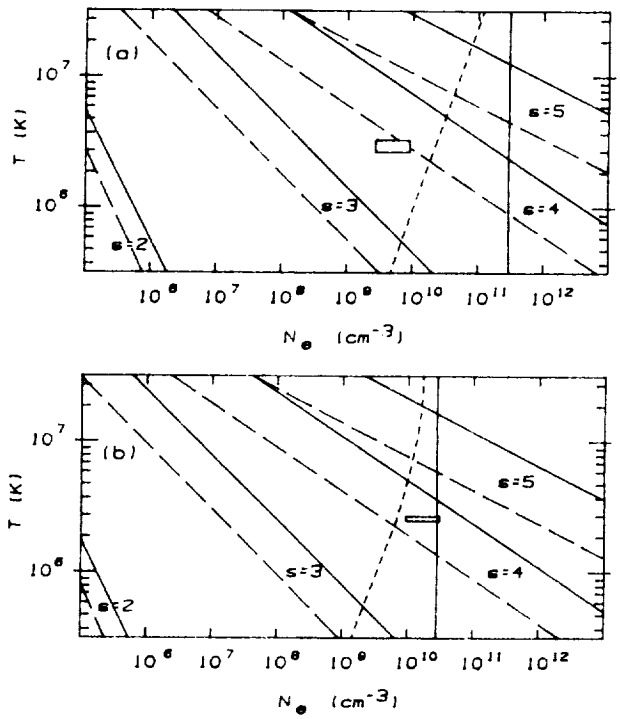

FIG. 5.—Curves of unit optical depth as a function of plasma temperature and density for the observation frequencies of (*a*) 4.9 GHz and (*b*) 1.45 GHz. The pairs of diagonal curves are for thermal gyroemission at the second through fifth harmonics. The lower (*dashed*) curve is for $\theta = 60°$ and the upper (*solid*) curve is for $\theta = 30°$. The short-dashed curves show unit optical depth for thermal bremsstrahlung, and the solid vertical lines show the electron densities corresponding to the plasma frequency. The box shows the range of temperatures and densities of the coronal loops determined from the X-ray data for (*a*) 1979 November 16 and (*b*) 1981 February 13.

that the observed emission was predominantly free-free. At 5 GHz free-free emission is not important and the loop sources are probably gr emission or, possibly, gyrosynchrotron emission from a more energetic population of electrons. Since the observed brightness temperatures were on the order of or slightly less than the electron temperatures, it is likely that the 5 GHz sources arose from low harmonic gr emission. The highest optically thick harmonic is the fourth, corresponding to a magnetic field strength of 440 G. Such a field strength is consistent with that found in the photosphere at the loop feet, except possibly for source H419-M. This source is consistent with fourth harmonic gr emission *and* the observed photospheric field strength only if either the photospheric field is directed at a high angle (60°) to the line of sight or if the photospheric field is concentrated in small, unresolved areas.

Because the solar atmosphere cannot be modeled by a simple plane parallel atmosphere, the microwave emission could have arisen from harmonic emission lower than the fourth (see Holman and Kundu 1985). The polarization data can be used to test this possibility. Following Takakura and Scalise (1970), in Figure 6 we have plotted the polarization as a function of the angle θ for the second through the fourth harmonics at 4.9 GHz (a polarization of 1.0 corresponds to 100% polarization in the extraordinary mode). Based on the X-ray data, we assumed the magnetic scale length to be 1×10^9 cm and the loop temperature and density to be 3×10^6 K and 5×10^9 cm^{-3}. All the 4.9 GHz sources showed some polarization, and three of the four showed polarizations of 33% or more (see Table 2). If the emitting region was essentially isothermal, as assumed, this would limit the emission to the third or fourth harmonic. Since the observations revealed single compact sources near the X-ray loop tops, high values of θ are likely, which favors fourth-harmonic emission (Fig. 6).

IV. COMPARISON WITH MICROWAVE LOOP MODELS

In the previous section we concluded that the most likely source of the microwave emission at 1.45 GHz (1981 February) was thermal bremsstrahlung, and at 4.9 GHz (1979 November) was fourth-harmonic gr emission. Now we would expect the bremsstrahlung microwave emission to be cospatial with the entire X-ray loop, since, to first order, they are isothermal and isobaric. Computations of the thermal gr emission from isothermal, two-dimensional dipole magnetic loop models have been made by Holman and Kundu (1985). In these dipole models the variation of the magnetic field strength along the length of the loop is such that several harmonics will contribute to the loop emission. However, contrary to our expectations for the thermal mechanisms, in most of the X-ray loops in our observations the microwave source appeared as a single, fairly compact region near the top of the loop. Therefore, we were forced to consider alternative models for both the 1.45 and 4.9 GHz observations.

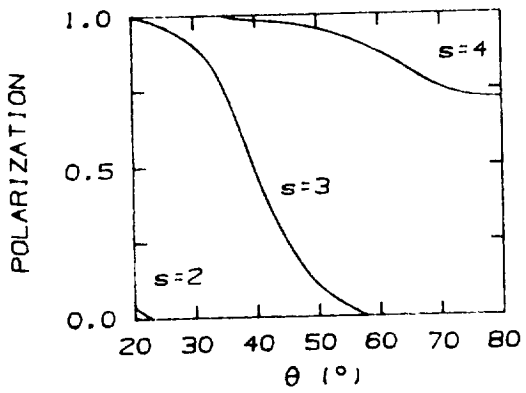

FIG. 6.—Fractional polarization (thermal gr emission in the extraordinary mode) as a function of θ, the angle between the line of sight and magnetic field, for the second, third and fourth harmonics of the gyrofrequency at 4.9 GHz. Plasma parameters consistent with the X-ray observations are assumed (see text).

a) 4.9 GHz: *1979 November 16*

At least two of the X-ray loops observed on 1979 November 16, namely H421-H and H419-M, had a single isolated microwave source near the loop top. In the simple isothermal dipole models, it is difficult to have fourth or even third gr harmonic emission from near the top of the loop without also detecting lower harmonic emission from the legs of the loop. Source H419-J could be consistent with the dipole model if the multiple microwave peaks arose from a single east-west loop. However, the authors of Paper I interpreted the X-ray and Hα data as indicating an arcade of north-south directed loops. Source H421-E′ could be consistent with a large variation in field strength along an asymmetric loop if H421-E were also associated with the western side of the X-ray loop. A difficulty with such an interpretation in this case, however, is that the peak brightness temperature of source E was greater than the electron temperature deduced from the X-ray observations. Thus, for these latter two sources, direct application of the dipole models of Holman and Kundu does not seem appropriate. (We note that both 419-M and 421-E′ were weak sources. The observations, however, reveal three cases of similar microwave structures coincident with X-ray loop tops, a situation unlikely to be due to chance.)

Therefore, we have examined two alternative models. In the first, the magnetic field is held constant along the loop, while in the second the field varies along the loop, though not as much as in the Holman and Kundu (1985) dipole models, and a limited temperature gradient exists in the loop. To obtain a model in which the magnetic field strength does not vary along the length of the loop, we use, instead of a dipole field, the field generated by a line current ($B \propto r^{-1}$). If the current is taken to be at the solar "surface" and hot (3×10^6 K) plasma is present only along field lines with $B \approx 400$–500 G, a semicircular loop (or arcade) might be observed in X-rays. At 4.9 GHz only fourth-harmonic emission would be observed. If the loop were observed from a direction perpendicular to the plane containing the loop, $\theta = 90°$ and the entire loop would be detected at 4.9 GHz. If the observer looked directly down upon the loop, however, θ would vary from 90° at the top to 0° at the footpoints. Since, for the observed densities and temperatures, the fourth harmonic is only optically thick at high values of θ, only the upper part of the loop would be observed. A computation of the 4.9 GHz brightness temperature (extraordinary mode) as a function of position x_0 along such a loop with average electron temperature and density is shown in Figure 7. The magnetic field strength of 440 G, corresponding to the fourth harmonic, is taken to be constant at the loop radius of $r = 2 \times 10^9$ cm. The scan is for the observer in the plane of the loop with the line of sight perpendicular to the surface ($\phi = 90°$). Some corresponding values of θ are also shown ($\cos \theta = x_0/r$).

The lowest brightness temperature plotted in Figure 7

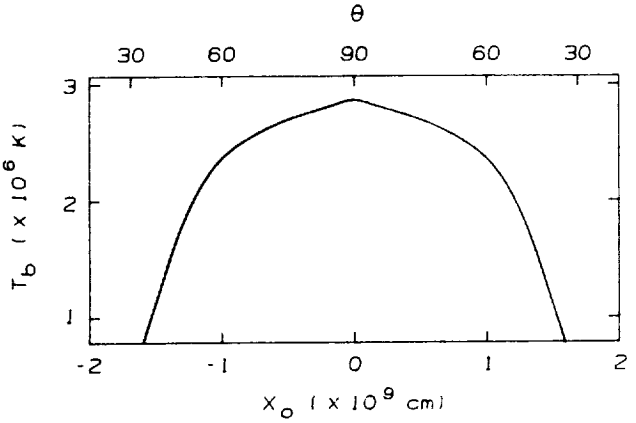

FIG. 7.—Computed 4.9 GHz brightness temperature (extraordinary mode) as a function of position for a scan along the projected length of a model semicircular loop with a constant field strength of 440 G (fourth-harmonic emission) at the loop radius of 2×10^9 cm. The loop electron temperature and density are taken to be 3×10^6 K and 5×10^9 cm^{-3}. The angle ϕ between the line of sight and the solar surface is 90°. Representative values of θ are also shown.

(8×10^5 K) corresponds to the lowest intensity contour on the microwave maps (Fig. 4). An important conclusion is that although part of the loop is not expected to be observed, the predicted microwave emission is still too extended to explain the compactness of the observed sources. Since the line-of-sight component of the loop magnetic field changes direction at $\theta = 90°$, the observed microwave polarization should change sign where the brightness temperature is greatest. It is interesting that source H421-H did show evidence for such a polarization reversal (percentage polarization: 33%), and the lowest contour was elongated along the axis of the X-ray loop (Fig. 4 and Paper I, Fig. 1). However, the region of left-hand polarization was less intense and the total intensity contours not as elongated as predicted by this model. On the other hand, source H419-M showed neither evidence for a polarization reversal nor significant elongation along the X-ray loop. It appears that, at least for source M, some variation in field strength along the loop would be required, although not as much as in the simple dipole model.

Sources such as H421-H and H419-M can most easily be explained by a temperature gradient along the loop, with the hottest region in the upper part of the loop as in the model considered by McConnell and Kundu (1983). However, as is typical (e.g., Webb 1981), the X-ray observations revealed the loops to be essentially isothermal along their length. Such a gradient is consistent with these observations if the hot, X-ray emitting plasma is limited to an extended region in the upper part of the loop, with a thin transition zone at the ends of the hot region. For fourth-harmonic emission, the transition zone must occur above the 580 G level within the loop, so that emission from the lower harmonics is not observed.

Detailed models of the observational results are beyond the scope of this paper. Full three-dimensional loop models are presently in preparation (Holman and Brosius 1986). In Figure 8 we demonstrate how the observed 4.9 GHz loop properties can be obtained from a modified dipole loop model. In the figure the third and fourth harmonic levels are shown in a model dipole loop with a minimum magnetic field strength of 425 G (at the top of the loop where $y = 10.4 \times 10^9$ cm) (cf. Fig. 1 of Holman and Kundu 1985). The y-coordinate is measured from the position of the dipole. The transition zone must occur

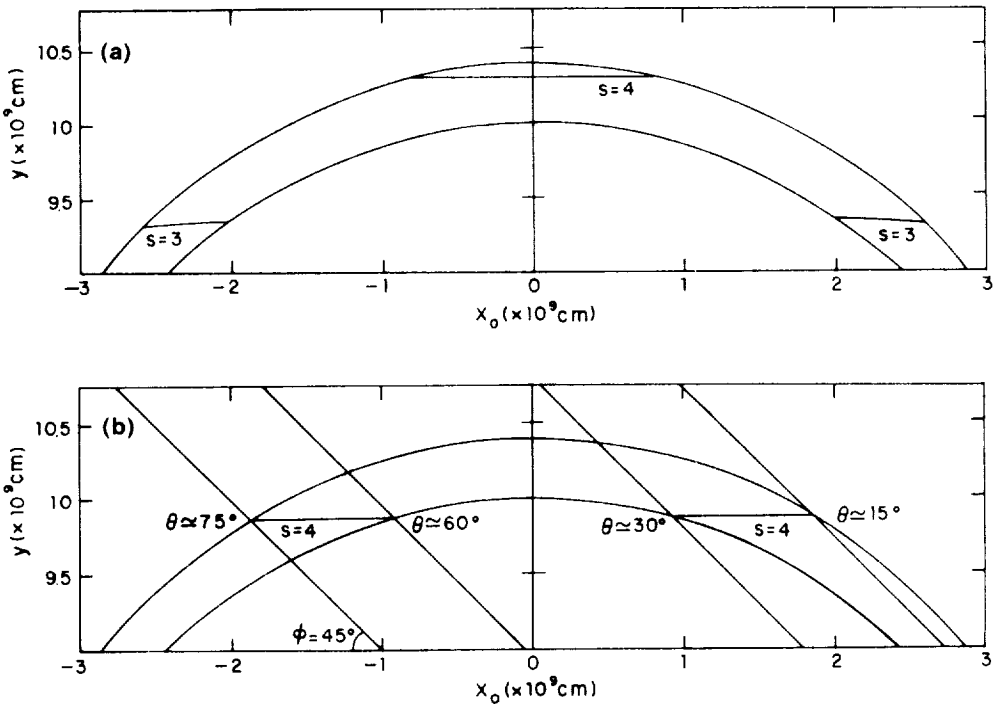

FIG. 8.—(*a*) A model dipole magnetic loop with a minimum magnetic field strength of 425 G at $y = 10.4 \times 10^9$ cm. The third- and fourth-harmonic thermal gr emission levels for an observation frequency of 4.9 GHz are shown. The y-axis coordinates are measured from the position of the dipole. (*b*) Same geometry, with a minimum magnetic field strength of 375 G at $y = 10.4 \times 10^9$ cm. Lines of sight with an inclination of $\phi = 45°$ are shown at the edges of the fourth-harmonic level, and corresponding values of θ are shown.

at or above the $y = 9.4 \times 10^9$ cm level so that third harmonic emission is not observed. The level at which fourth harmonic emission occurs ($B = 440$ G) is near the top of the loop, so that only a single microwave source at the top would be observed. If the observer looked down on the loop ($\phi = 90°$), a polarization reversal would be expected, as for the line-current model. A slight inclination of the line of sight at $\phi = 75°$ or less, however, will give a source of uniform polarization. An inclination angle somewhat larger than 75° may in fact explain the polarization structure of source H421-H. The line of sight might also have an inclination out of the plane of the loop, as in the actual observations, without changing these basic features.

It seems unlikely that the 440 G level typically will appear just at the apex of a magnetic loop. Figure 8*b* shows a model loop for which the fourth-harmonic level is somewhat lower, so that it is separated into a region in each leg of the loop. The field strength at the top ($y = 10.4 \times 10^9$ cm) of this loop is 375 G, and the third harmonic level is just below the x_0 axis. If the observer looked directly down on the loop ($\phi = 90°$), a microwave source would be observed in each leg. These sources are identical if $\phi = 90°$ (except for sign of polarization). For smaller values of ϕ they differ, since the range of θ is no longer the same for the two regions. As an example, in Figure 8*b* lines of sight with an inclination of $\phi = 45°$ are shown. The values of θ for the fourth-harmonic source in the left leg of the loop range from 60° to 75°. In the right leg, however, θ ranges from 15° to 30°. For the parameters of this model, the fourth harmonic is not optically thick at these small angles, and the maximum brightness temperature of the region in the right leg of the loop would be sufficiently low to be unobservable. Hence, once again, only a single, relatively compact microwave source would be observed near the top of the projected image of the loop. The same results can be obtained for an observer outside the plane of the loop, as long as $\theta \lesssim 30°$ for the region in the right leg of the loop.

An alternative to requiring that the transition zone occur above the third harmonic level might be to have free-free absorption in the plasma external to the loop mask microwave emission from the lower parts of the loop. In the previous section the free-free optical depth at 4.9 GHz for the X-ray loops was determined to be $\tau_{ff} \approx 0.01$–0.06. If the external medium had a similar emission measure but a temperature an order of magnitude smaller than in the loop, $\tau_{ff} \approx 0.3$–1.6 for the external plasma. Thus, this mechanism is a possibility, particularly if the density scale length is larger than the thickness of the X-ray loop. However, if the density scale length of the external plasma is determined by gravity, it will decrease with decreasing temperature, e.g., $l = 1 \times 10^9$ cm for a 3×10^5 K plasma. Also, if the external plasma density is much lower than the loop density, the free-free optical depth will be too small for absorption to occur.

b) 1.45 GHz: *1981 February 13*

We found earlier that free-free absorption was important for the loop emission at 1.45 GHz. The X-ray loops were optically thick, but, as at 4.9 GHz, only a single, compact microwave source was observed (Fig. 1). Hence, both the failure to detect in emission the entire X-ray loops or any of the other observed X-ray structures, and the compactness of the associated microwave source, must be explained. That most of the loops were not observed at 1.45 GHz suggests that absorption by an external plasma might be important. If we assume that microwave source A was directly associated with X-ray loops 3 or 4 or both (Fig. 1), we can estimate the characteristics of the external plasma needed to detect the loop top but mask the emission from the sides of these loops. A plot of the free-free emission from a model demonstrating how this can occur is shown in Figure 9. The model consists of a semicircular loop with an outer radius of 3×10^9 cm and an inner radius of 2.5×10^9 cm. The loop has a uniform temperature and density of 2.5×10^6 K and 1.5×10^{10} cm^{-3}, like those of the observed X-ray loops. The loop is surrounded by a plasma with a uniform temperature of 1×10^5 K. The external plasma density falls off exponentially with a scale height of 3.3×10^8 cm, the gravitational scale height for a plasma of this temperature. The external plasma density at the top of the loop (height $= 3 \times 10^9$ cm) is 1.6×10^9 cm^{-3}. Figure 9 shows a plot of 1.45 GHz brightness temperature as a function of position along the loop ($\phi = 90°$). The width and peak brightness temperature of the resulting source are comparable to the observed values, as desired. (Note that the lowest contour on the 1.45 GHz map was 1.7×10^5 K [Fig. 1]. In computing the brightness temperature for Figure 9, a small contribution from the index of refraction has been neglected.)

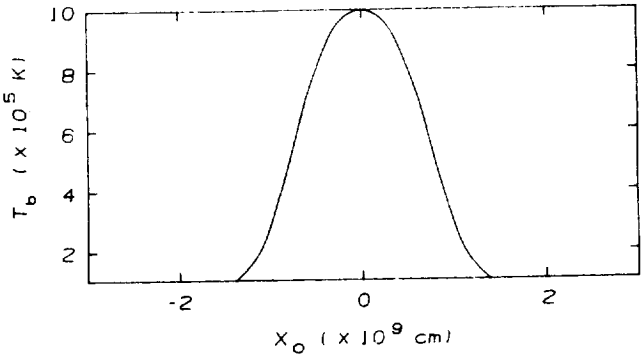

FIG. 9.—Brightness temperature at 1.45 GHz as a function of position along the loop for a scan ($\phi = 90°$) of a model semicircular loop embedded in 1×10^5 K ambient plasma with density decreasing exponentially with height. The outer and inner radii of the loop are 3×10^9 (the sides of the box) and 2.5×10^9 cm respectively. The loop electron temperature and density are assumed to be 2.5×10^6 K and 1.5×10^{10} cm^{-3}. The microwave emission is thermal bremsstrahlung. See text for details.

Although the model used in Figure 9 treats the external plasma as a uniform, plane-parallel atmosphere, it could, for example, also be a more localized sheath surrounding the X-ray loop. This model is preliminary and intended only to be illustrative; it is less reliable at lower heights, which are unobservable at 1.45 GHz. The model does suffice to demonstrate how the observed structure can be obtained and indicates what properties of the external plasma are required to explain the observational results. More detailed models are in preparation (Brosius and Holman 1986). An external temperature of $\lesssim 10^5$ K would be required to avoid observable emission at 1.45 GHz. A temperature of the plasma this low (with its corresponding scale height) is also required to produce a microwave source that is sufficiently compact. Lower temperatures and scale heights produce more compact sources. The required emission measure of the 10^5 K plasma is estimated for the model to be $\sim 10^{27}$ cm^{-5}. This value is two orders of magnitude smaller than the emission measure of the hot ($> 10^6$ K) loop plasma but an order of magnitude larger than observed in active regions with the Harvard EUV Spectrometer on *Skylab*

(Noyes *et al.* 1985).[5] The emission measure could be an order of magnitude smaller if the plasma temperature were closer to 10^4 K.

An alternative model that does not require such a large emission measure is to have the external absorption be gyroresonance rather than free-free. Third-harmonic absorption with $T \approx 10^5$ K requires a plasma density on the order of that required for free-free absorption (see Fig. 5*b*), so the absorption is likely to be at the second harmonic level. In this case the magnetic field strength at the absorbing level would be 260 G, and the emission measure of the 10^5 K plasma could be as low as $\sim 10^{21}$ cm^{-5} (cf. Fig. 5*b*). The compact microwave source could be reproduced if the second harmonic level either grazed the 2.5×10^6 K loop plasma or cut through a transition zone around the loop. In this case the microwave source would likely arise from a combination of gr and free-free emission.

A third alternative is that the entire X-ray loop was masked by either second harmonic gr or free-free absorption, and the microwave source arose from gr emission from a higher, cooler ($\lesssim 1 \times 10^6$ K) loop. Such a loop might be part of an arcade of coronal loops, with only the lower ones being sufficiently dense or hot to be detected in X-rays. The source would likely be third harmonic emission with $B = 170$ G. Such a model is similar to that discussed for the 4.9 GHz emission, since only a single, compact source was observed. Whichever model is correct, however, one conclusion remains: the X-ray loops must have been enveloped by cooler plasma with a temperature $\lesssim 10^5$ K.

V. DISCUSSION

We have analyzed two data sets in order to improve our understanding of the plasma and magnetic field properties of active region coronal loops. Each of these sets consisted of co-aligned, high spatial resolution soft X-ray, microwave and magnetogram images that were used to compare observations of coronal loops and their feet in the photosphere and to constrain possible microwave emission mechanisms. Each of the VLA observations was at a single frequency; the 1979 observation was at 5 GHz (6 cm) and had suitable polarization data (Paper I), and the 1981 observation was at 1.45 GHz (20 cm) with no polarization information. Many microwave sources were detected at 5 GHz (Paper I), whereas only a few sources of lower T_b were observed at 1.45 GHz. At both frequencies the correspondence between the X-ray and microwave emission was poor. However, within the three active regions analyzed, there were six X-ray loops with cospatial microwave sources near the loop top. The plasma parameters of these loops were typical of quiescent active region loops. The microwave loop top sources had $T_b = 1$–2.5×10^6 K, and three of the four 5 GHz sources were significantly polarized.

Using these results, we constructed model coronal loops and compared the predicted distribution of thermal microwave emission with the observations. At the higher frequency (4.9 GHz; 6 cm), simple isothermal, dipole loop models (i.e., Holman and Kundu 1985) do not fit the observations. The loop emission is best fitted by fourth-harmonic gr emission from a dipole loop (Fig. 8) with a magnetic field of ~ 440 G near the loop top and with the transition zone at or above the ~ 580 G level to suppress lower harmonic emission. This model has less longitudinal field variation than the models of Holman and Kundu (1985). Alternative possibilities, such as a model where the field is generated by a line current and remains constant along the loop, or one combining gr emission from the loop top and free-free absorption from an external plasma, were considered less likely. We also found that bremsstrahlung alone could not provide sufficient opacity to explain the 5 GHz sources (for which $T_b > 10^6$ K).

At the lower frequency (1.45 GHz; 20 cm), the loops are optically thick to free-free emission. In order to explain the restriction of the 1.45 GHz emission to the top of occasional loops, it is necessary to invoke absorption by cooler material ($T_e \lesssim 10^5$ K) existing either as a sheath around the loops or as part of an external medium. A possible model (Fig. 9) suggests that the loop field strength would have to be below 260 G, so that the loop top emission would not be masked by second-harmonic absorption in the external medium. Other possibilities we considered include loop emission from both free-free and second harmonic gr, or third harmonic emission with $B \approx 170$ G from a higher, cooler loop invisible in X-rays. The important result is that an external plasma of $T_e \lesssim 10^5$ K is required in all of these models to explain the combined observations at 1.45 GHz.

In several recent studies, researchers have claimed detection of neutral hydrogen and helium in absorption over active regions (see Webb 1981 for a review). Schmahl and Orrall (1979) found column densities of such cool $N_H > 10^{17}$ cm^{-2}. And Foukal (1981) discussed EUV observations of opaque coronal material at $\lambda > 912$ Å that was most likely due to absorption by the neutral carbon continuum. Sufficient amounts of such cool material could easily absorb the free-free microwave emission from all or portions of coronal loops and explain the general absence of emission from the X-ray loops. However, white-light and X-ray observations during solar eclipses suggest that any material between coronal loops must be at a pressure at least 3–6 times less than in the loops (e.g., Krieger 1977).

It has been argued from recent observations that entire, large coronal loops at 5 GHz (Kundu and Velusamy 1980; Shibasaki *et al.* 1983) and at 1.45 GHz (Lang, Willson, and Rayrole 1982; Lang and Willson 1983, 1984) are being observed. In fact, Lang and Willson (1983) have suggested that such 20 cm coronal loops, whose dominant emission should be bremsstrahlung, are the radio-wavelength counterparts of X-ray coronal loops. However, none of these observations were supported by simultaneous spatially resolved X-ray imagery. In studies such as ours, where resolved X-ray and microwave images have been compared, the detailed correspondence of the emission at both wavelengths has been poor. Specifically, we have found *no* cases of cospatial X-ray and microwave emission outlining entire loops and therefore cannot support the interpretation that complete magnetic loops filled with coronal plasma will be imaged at any single microwave frequency.

However, although our 1.45 GHz source A was roughly circular, elongated or curvilinear microwave structures have apparently been observed by others. This suggests that at least portions of coronal loops are being detected. For instance, McConnell and Kundu (1983) observed a looplike structure at 1.45 GHz and, using both 1.45 and 5 GHz observations and

[5] The portion of the active region discussed here is distant from sunspots and, therefore, is unlikely to be effected by so-called "sunspot plumes," which can have enhanced emission at $T_e \approx 2.6 \times 10^5$ K (e.g., Foukal *et al.* 1974; Webb 1981).

the Rosner, Tucker, and Vaiana (1978) loop model, they concluded that their data were most consistent with bremsstrahlung emission from the loop feet and gr emission from the loop top. They disputed the claims that at 20 cm the entire loop emission could be attributed to thermal bremsstrahlung. Other recent modeling results (e.g., Paper II; this paper; Strong, Alissandrakis, and Kundu 1984; Holman and Kundu 1985) support this view and imply that, at any given radio frequency, the emission from a quiescent coronal loop will be patchy and may be dominated by different mechanisms at different layers (or heights) of the loop. And our results suggest that external absorption may play a significant role in microwave loop emission. Taken together, these studies demonstrate that the physical interpretation of coronal loops requires an appropriate combination of high spatial resolution observations at several wavelengths with mature loop models.

Our observational and modeling results have revealed important differences in interpretation with other results based primarily on observations at a single microwave frequency. Further substantial progress in this field will require simultaneous imaging of coronal structures in soft X-rays, the EUV, and microwaves at several frequencies, and of the photospheric field for comparison with improved theoretical models of coronal loops.

We are grateful for data and discussions provided by the following individuals: R. Bentley of Mullard Space Science Laboratory, UCL, England, for magnetogram contour maps; E. Cliver of AFGL, Hanscom Air Force Base, for Sagamore Hill radio data; L. Gilliam of NSO–Sacramento Peak Observatory for Hα patrol film; H. Jones and J. Harvey of NSO–Kitt Peak Observatory for magnetograms; G. Hurford of OVRO for 10.6 GHz radio data; and S. Kahler of Emmanuel College for *GOES* X-ray plots. D. McConnell performed the initial reductions of the 1981 February 13 microwave data at the University of Maryland. We thank the AS&E Technical Publications Group for assistance with the images and figures. This study was supported at AS&E by NSF grant ATM-8314115 and at Emmanuel College by AFGL contract AF 19628-82-K-0039. G. D. H. acknowledges partial support from NASA grant 188-38-53-01. The work of M. R. K. and R. K. S. was supported by NASA grant NGR-21-002-199, NASA contract NAG 5511, and NSF grant ATM-84-15388.

REFERENCES

Brosius, J. W., and Holman, G. D. 1986, *Ap. J.*, submitted.
Cheng, C.-C. 1980, *Ap. J.*, **238**, 743.
Chiuderi-Drago, F., Bandiera, R., Falciani, R., Antonucci, E., Lang, K. R., Willson, R. F., Shibasaki, K., and Slottje, C. 1982, *Solar Phys.*, **80**, 71.
Davis, J. M., Gerassimenko, M., Krieger, A. S., and Vaiana, G. S. 1975, *Solar Phys.*, **45**, 393.
Davis, J. M., and Webb, D. F. 1985, *A Study of the Cyclical Variations of Coronal Holes and Their Relation to Open Magnetic Fields* (AFGL-TR85-0003).
Foukal, P. 1981, *Ap. J.*, **245**, 304.
Foukal, P. V., Huber, M. C. E., Noyes, R. W., Reeves, E. M., Schmahl, E. J., Timothy, J. G., Vernazza, J. E., and Withbroe, G. L. 1974, *Ap. J. (Letters)*, **193**, L143.
Holman, G. D., and Brosius, J. W. 1986, in preparation.
Holman, G. D., and Kundu, M. R., 1985, *Ap. J.*, **292**, 291.
Hurford, G. 1986, private communication.
Kahler, S. W., Davis, J. M., and Harvey, J. W. 1983, *Solar Phys.*, **87**, 47.
Kahler, S. W., Webb, D. F., Davis, J. M., and Kundu, M. R. 1984, *Solar Phys.*, **92**, 271 (Paper II).
Kahler, S. W., Webb, D. F., and Moore, R. L. 1981, *Solar Phys.*, **70**, 335.
Krieger, A. S. 1977, in *Proc. OSO-8 Workshop* (Boulder: University of Colorado), p. 98.
Kundu, M. R., Allissandrakis, C. E., Bregman, J. D., and Hin, A. C. 1977, *Ap. J.*, **213**, 278.
Kundu, M. R., Schmahl, E. J., and Gerassimenko, M. 1980, *Astr. Ap.*, **82**, 265.
Kundu, M. R., and Velusamy, T. 1980, *Ap. J. (Letters)*, **240**, L63.
Lang, K. R. 1980, *Astrophysical Formulae* (2d ed.; New York: Springer-Verlag).
Lang, K. R., and Willson, R. F. 1983, *Adv. Space Res.*, Vol. **2**, No. 11, p. 91.
———. 1984, *Adv. Space Res.* Vol. **4**, No. 7, p. 105.
Lang, K. R., Willson, R. F., and Gaizaukas, V. 1983, *Ap. J.*, **267**, 455.
Lang, K. R., Willson, R. F., and Rayrole, J. 1982, *Ap. J.*, **258**, 384.
McConnell, D., and Kundu, M. R. 1983, *Ap. J.*, **269**, 698.
Noyes, R. W., Raymond, J. C., Doyle, J. G., and Kingston, A. E. 1985, *Ap. J.*, **297**, 805.
Pallavicini, R., Sakurai, T., and Vaiana, G. S. 1981, *Astr. Ap.*, **98**, 316.
Rosner, R., Tucker, W. H., and Vaiana, G. S. 1978, *Ap. J.*, **220**, 643.
Schmahl, E. J., Kundu, M. R., Strong, K. T., Bentley, R. D., Smith, J. B. Jr., and Krall, K. R. 1982, *Solar Phys.*, **80**, 233.
Schmahl, E. J., and Orrall, F. Q. 1979, *Ap. J. (Letters)*, **231**, L41.
Shibasaki, K., Chiuderi-Drago, F., Melozzi, M., Slottje, C., and Antonucci, E. 1983, *Solar Phys.*, **89**, 307.
Solar Geophysical Data Bulletins 1981, (Boulder: US Dept. of Commerce, NOAA) (SGD).
Strong, K. T., Alissandrakis, C. E., and Kundu, M. R. 1984, *Ap. J.*, **277**, 865.
Takakura, T., and Scalise, Jr., E. 1970, *Solar Phys.*, **11**, 434.
Vaiana, G. S., Van Speybroeck, L., Zombeck, M. V., Krieger, A. S., Silk, J. K., and Timothy, A. 1977, *Space Sci. Instr.*, **3**, 19.
Webb, D. F. 1981, in *Solar Active Regions*, ed. F. Q. Orrall (Boulder: Colorado Associated Universities Press), p. 165.
Webb, D. F., and Davis, J. M. 1985, *Solar Phys.*, **102**, 177.
Webb, D. F., Davis, J. M., Kundu, M. R., and Velusamy, T. 1983, *Solar Phys.*, **85**, 267 (Paper I).
Webb, D. F., and Zirin, H. 1981, *Solar Phys.*, **69**, 99.

J. M. DAVIS: NASA/Marshall Space Flight Center, Code ES-52, Huntsville, AL 35812

G. D. HOLMAN: Laboratory for Astronomy and Solar Physics, Code 682, NASA/Goddard Space Flight Center, Greenbelt, MD 20771

M. R. KUNDU: Astronomy Program, Space Science Building, University of Maryland, College Park, MD 20742

R. K. SHEVGAONKAR: Indian Institute of Astrophysics, Bangalore 560 034, India

D. F. WEBB: AFGL/PHP, Hanscom Air Force Base, MA 01731

THE ASTROPHYSICAL JOURNAL, 315:729, 1987 April 15

ERRATUM

In the paper "Neutrino Flows in Collapsing Stars: A Two-Fluid Model" by J. Cooperstein, L. J. van den Horn, and E. A. Baron (*Ap. J.*, **309**, 653 [1986]), equations (4.30) and (4.33) erroneously contain the coefficient pertaining to neutrino-proton scattering (cf. eqs. [4.31] and [4.34]) and should be corrected to read

$$\mathscr{A}_{\nu n} = -\langle z \rangle \frac{5G^2}{3\pi^3}\left(\frac{1}{4}+\frac{5}{4}g_A^2\right) n_n T_\nu^6 F_4(\eta_\nu)\,, \tag{4.30}$$

$$\mathscr{A}_{\nu n} = -\langle z \rangle \frac{10G^2}{3\pi}\left(\frac{1}{4}+\frac{5}{4}g_A^2\right) n_n \epsilon_\nu T_\nu \omega_\nu\,. \tag{4.33}$$

4.18 The Flight Test of a Grazing Incidence Relay Optics Telescope for Solar X-Ray Astronomy Utilizing a Thinned, Back-Illuminated CCD Detector

J. Daniel Moses

American Science and Engineering, Inc.
Cambridge, Massachusetts 02139

and

John M. Davis

Marshall Space Flight Center, Alabama 35812

Reprinted from SPIE Vol. 982—X-Ray Instrumentation in Astronomy II

THE FLIGHT TEST OF A GRAZING INCIDENCE RELAY OPTICS TELESCOPE FOR SOLAR X-RAY ASTRONOMY UTILIZING A THINNED, BACK-ILLUMINATED CCD DETECTOR

J. Daniel Moses

American Science and Engineering, Inc.
Cambridge, Massachusetts 02139

and

John M. Davis

Marshall Space Flight Center, Alabama 35812

Abstract

The new AS&E Ultrahigh Resolution Soft X-Ray Solar Research Rocket Payload has been successfully flown twice on Black Brant IX Sounding Rockets from White Sands Missile Range. These flights, conducted on 15 August 1987 and 11 December 1987, provided the first test of the new payload which consists of 3.8X magnifying hyperboloid-hyperboloid grazing incidence relay optic used in conjunction with an existing Wolter-I primary mirror. An RCA SID 500 series CCD detector was utilized in a thinned, back-illuminated configuration for recording the images. The 5.4 m effective focal length of the compound optics system resulted in a plate scale of 1 arc second per pixel which is comparable to the inherent resolution of the primary mirror. These flights represent the first use in X-ray astronomy of either of these two new technologies. These observations are presented with comparison to laboratory measurements and theoretical expectations of the instrument performance.

Introduction

The scientific objective of the new AS&E Ultrahigh Resolution Soft X-Ray Solar Research Rocket Payload is high spatial resolution observations with short integration (exposure) times in order to search for fine scale transient coronal phenomena. The motivation for this search arises from the current interest in observations of coronal waves or nanoflares which may be associated with active region heating (e.g., Parker, 1988)[1]. These observations require several arc second spatial resolution with temporal resolution of the order of a second. Such observations have not been previously available.

In order to address this observational goal of simultaneous high temporal and spatial resolution, two emerging technologies were combined each having individual applications to X-ray astronomy. X-ray sensitive CCD detector technology provides high detection efficiency so that short integration times become possible. CCD detectors also provide accurate and consistent measurement of X-ray energy deposit which is straight forward to model and calibrate. Grazing incidence relay optic technology provides the means in the soft X-ray regime (<40 Angstroms) to match a variety of focal plane instruments to the same primary mirror. The combination of a CCD detector with a magnifying grazing incidence relay optic provided a match of the plate scale of the AS&E high resolution rocket borne X-ray mirror to the spatial resolution of the CCD detector so that the high temporal resolution available with the CCD detector could be obtained with the high spatial resolution of the existing X-ray optics.

Extensive modeling and laboratory testing was conducted to determine the performance in the X-ray regime of both the compound grazing incidence optical system and the CCD detector. Flight tests of the compound telescope/CCD detector system were conducted on 15 August 1987 and 11 December 1987 as an ancillary experiment during the 1987 X-ray Bright Point Observing Campaign. A proof of the design principle was established during these flights, but initial analysis of the observations indicates a level of performance below expectation in both sensitivity and spatial resolution. The reasons for this apparent lack of performance are not understood and further research is required to explore these questions.

Instrumentation

Grazing Incidence Relay Optics Compound Telescope

The compound X-ray optics system consists of a Wolter Schwarzschild primary mirror coupled with a diverging magnifier relay optic as illustrated in Figure 1. The relay

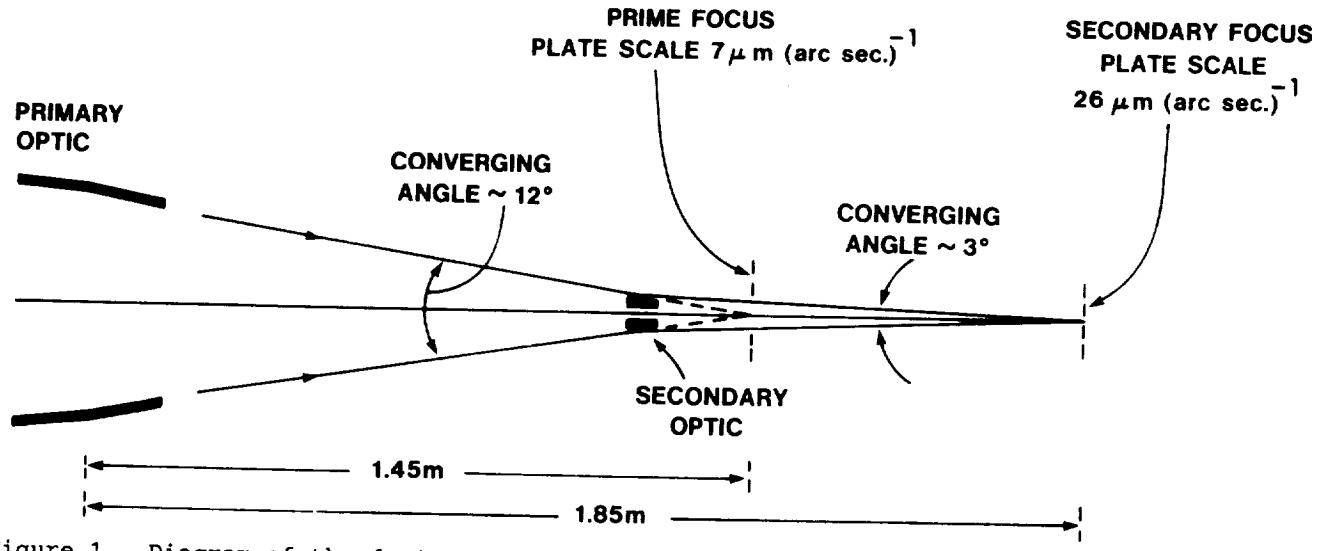

Figure 1. Diagram of the design for the grazing incidence relay optics system.

optic is an externally reflecting mirror with two hyperboloidal segments. This configuration is analogous to the well-known Barlow lens magnifier and the specific design considerations of such a grazing incidence mirror are described by Chase et al (1982)[2]. The relay optic manufactured for this payload has a magnification of 3.7 which produces the desired plate scale of 26 microns (arc sec)-1. Although the effective focal length is 5.4 m, the actual length of the imaging system is 1.85 m thereby fitting within the 2 m envelope available in the sounding rocket payload. The magnified plate scale matches the pixel size of the CCD used in this payload to the inherent resolution of the X-ray optical system. Table 1 summarizes the design of the primary and secondary mirrors.

The new AS&E Solar Research Rocket payload is constructed to obtain observations at both the prime focus and the secondary focus during a single flight. The secondary optic is mounted on a translation stage that can be inserted into or removed from the optical path upon command of the experiment computer. A film camera is also mounted on a separate translation stage that can be inserted into or removed from the prime focus upon computer command. At take off, the secondary optic is stowed out of the optical path and the film camera is positioned in the prime focus to accomplish the primary mission of these flights acquisition of full disk photographic images of the solar X-ray corona. Following the completion of the primary mission, the film camera is retracted from the optical path and the relay optic inserted into the optical path to form a magnified image at the secondary focus where the CCD camera image plane is located.

The performance of compound telescope in the X-ray regime has been measured utilizing the 89.5 meter vacuum collimator long-tube facility (LTF) at AS&E. A report on these measurements was made by Moses et al. (1986)[3]. The on-axis performance of the compound telescope was found to be comparable with the one arc-second level resolution of the primary mirror alone as reported earlier by Davis et al. (1979)[4]. Since the distance from the relay optic to the image plane is 0.61 m while the effective focal length of the primary mirror is 5.4 m, the plate scale for scattering from the relay optic (from figure error or surface roughness) is much smaller than the equivalent scattering from the primary mirror projected onto the focal plane. The off-axis performance of the compound telescope was found to be much worse than the primary mirror alone. Because the off-axis

Table 1. Design Requirements of the X-Ray Mirrors

	Primary	Secondary
Figure	Wolter Schwarzschild	Hyperboloid Hyperboloid
Material	Fused Silica	Nickel Coated Beryllium
Principal Diameter	30.48 cm	3.15 cm
Focal Length	144.9 cm	-19.9 cm
Geometrical Area		
On-axis	42.4 cm^2	34.3 cm^2
2 arc minutes	39.6 cm^2	5.8 cm^2
Plate Scale	7.0 microns (arc sec)$^{-1}$	26.0 microns (arc sec)$^{-1}$
Field of View	60 x 60 (arc min)^2	2.5 x 2.5 (arc min)^2
Resolving Power (X-Ray)	1 arc sec	1 arc sec

performance of the compound telescope so strongly influences the appearance of the flight images, the previously reported off-axis measurements will be summarized.

The relay optic design was optimized for maximum on-axis resolution. The resulting lengths of the relay optic hyperboloid mirrors are insufficient to reflect much of the off-axis flux. Figure 2 illustrates the consequent vignetting of off-axis rays by the relay optic both as predicted by ray trace calculation and as measured in the 89.5 m LTF. The restriction of the vignetted field of view to a circle of radius 2.5 arc minutes is essentially the same for both the 89.5 m and infinite source distance. The compound telescope also suffers from a form of astigmatism. The off-axis image blur due to geometric optics (no scattering) is greater in the direction perpendicular to the displacement of the image from the on-axis point. A ray trace calculation of the rms blur of a point source displaced in the X direction from the on-axis point is presented in Figure 3. To express the asymmetric character of the off-axis

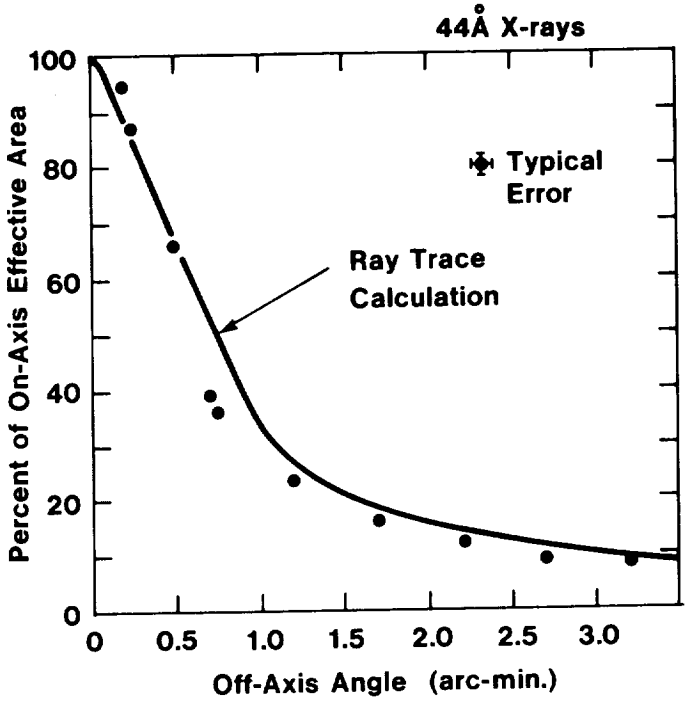

Figure 2. Ray trace calculation and observed off-axis decline in energy throughput of the compound telescope for a 89.5 m source distance.

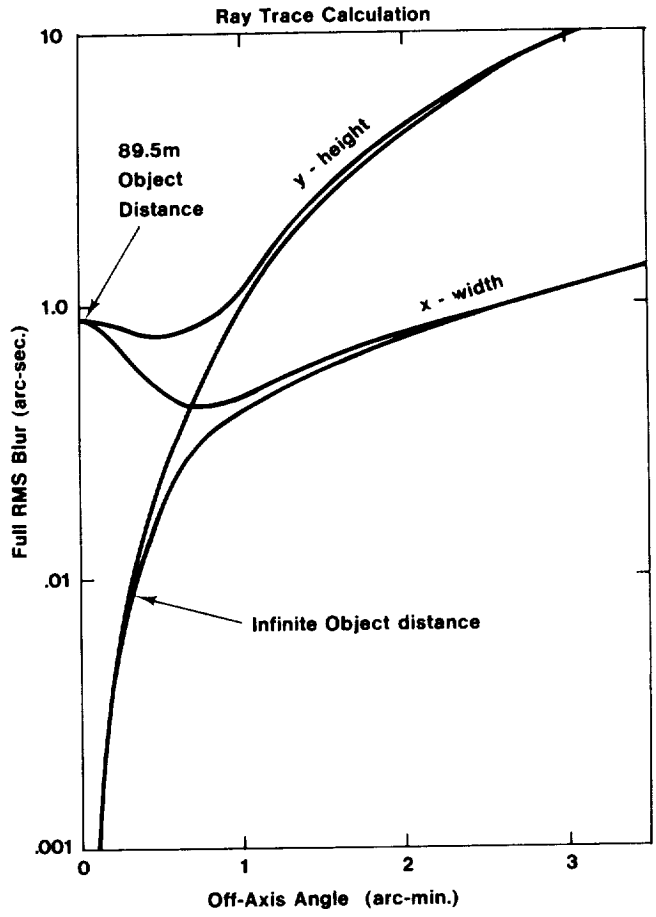

Figure 3. Ray trace calculation of blur (not including scattering) in the two dimensions of the compound telescope image plane for a point source off-axis in the X direction.

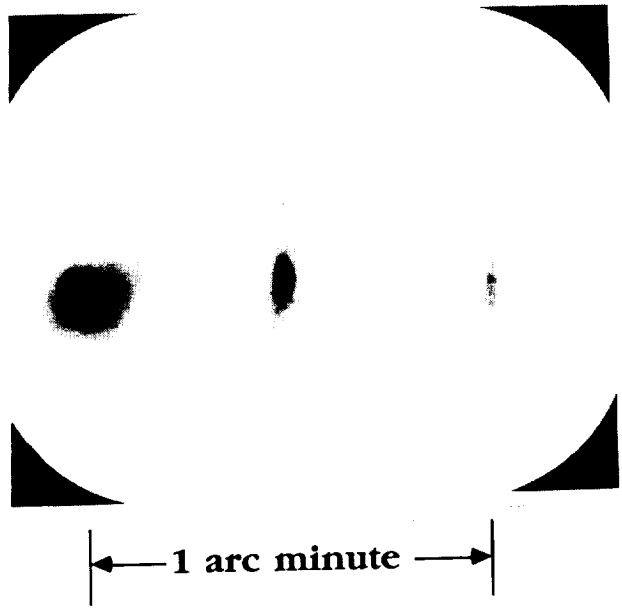

Figure 4. Photograph of X-ray source imaged by the compound telescope for the off-axis displacements (from left to right) of 0 arc seconds, 30 arc seconds, and 60 arc seconds.

aberration, the blur in the X and Y directions are plotted separately. For off-axis angles less than 2 arc min, the ray trace calculation predicts a different blur pattern for a 89.5 m and an infinite object distance, so both functions are plotted in Figure 3. This aberration is obvious in the photograph presented in Figure 4 of an X-ray point source in the AS&E 89.5 m LTF for off-axis displacements of 0, 30, and 60 arc seconds. Further, it can be seen in Figure 4 that the wings of the point response function (which are due to scattering and figure errors) clearly demonstrate the asymmetric off-axis aberration predicted by the ray trace calculations for the unscattered rays in the core of the point response function. Therefore, the net effect on the image is much greater than the several arc second blur indicated by the ray trace. A practical limit on the field of view is difficult to establish since the ray trace without scattering provides only a qualitative guide to the off-axis aberration, although a 30 arc sec radius field of view appears likely to be distortion free.

X-Ray Sensitive Charge Coupled Device Detector

The CCD detector is an RCA SID 500 series device operated in a back-side illuminated mode for soft X-ray sensitivity. This required thinning the device to a thickness of approximately 10 microns. This is a low noise, three-phase frame transfer device with 30 micron square pixels. The pixels are arranged in a 320 (H) by 256 (V) format. The CCD camera converts the X-ray imaged focussed on the CCD device into a 256 x 256 pixel array with each pixel magnitude represented by a digital word. As each pixel is sequentially clocked out of the CCD, it is analyzed, incorporated into the telemetry bit stream format, transmitted to a ground station receiver, and recorded.

The video chain of the X-ray CCD camera consists of a preamplifier, a correlated double sample and hold and an analog to digital converter (ADC). Ancillary circuits include a clock driver which provides the regulated analog clock voltages required by the CCD. It receives timing signals from a clock generator which is synchronized to the basic frequency of the PCM modulator. The clock driver also provides the digital control signals required by the correlated double sample and hold and the ADC. The preamplifier, which amplifies the analog video signal, is designed to operate with a CCD which has an on-chip source follower transistor. It is a linear amplifier with a gain of eleven, and it provides the sample and hold circuit with a low impedance source.

The correlated double sample and hold samples the difference between the video pulse generated by the CCD and a correlated null reference pulse and passes this difference signal for processing by the ADC. The reference or "background" level signal is generated, before transferring out the next pixel charge, by discharging the previous pixel charge at the CCD output transistor through a switching transistor. After the transient caused by this discharge has decayed, the output level is an indication of the "black" level of the CCD. This output level is not exactly equal to the pixel black level because of the leakage charge transferred by the switching transistor control signal. The resulting differential does not change because it depends only on the control signal voltage, which is well regulated, and the geometry of the switching transistor, which is extremely stable. It can therefore be accurately cancelled by an externally introduced offset signal. This signal is generated in the video offset control from a series of analog switches in the control register.

The circuits in the clock generator and clock driver generate the wave forms that are used to move the exposed image from the image area to the storage area in the CCD. The stored image is then moved, line by line, to a readout register and then, pixel by pixel, to the output transistor. Additional features of these circuits include:

* Raster limit feature which allows blanking of the beginning and the end of each line to reduce the line from 320 to 256 pixels.

* Line blanking, for the blanking of entire lines.

* The combination of "dummy" readouts with line blanking which allows the CCD to be partially or totally cleared without undesirable and time-consuming digital readout.

The sounding rocket telemetry clock has a basic frequency (frame rate) of 1024 Hz. Since no provision is made for on-board data storage other than the storage area of the CCD, the telemetry rate determines the timing for the CCD. The minimum time for a frame transfer of a complete image into the storage area with this clock is 15.6 msec. Since it is anticipated that exposure as short as 20 msec will be required, electronic shuttering is insufficient. A mechanical shutter system was fabricated utilizing an iris shutter in combination with a feedback controlled chopper wheel.

The total time for telemetry of a complete image is approximately 10 sec (8 image pixels are contained in a frame of image data). Exposure times on the order of tens of

seconds may also be required for some applications. Therefore, it is necessary for the CCD to be cooled to reduce thermal noise. An -80°C operating temperature is obtained through a cold strap connection to a liquid nitrogen reservoir. Active temperature control is achieved by electric heaters and a feedback circuit. The CCD and the CCD head electronics board (containing the preamplifier and logic-level clocks) are mounted inside the vacuum jacket of the LN2 dewar to prevent condensation on the CCD. A window in the dewar is opened when the payload reaches observing altitude.

A qualitative indication of the performance of the CCD camera in the X-ray regime can be seen in the shadowgraph image presented in Figure 5. Edges are clearly resolved at the 3 pixel level in this photograph with a finite mask to CCD distance. The 6-minute exposure time also indicates the high level of background suppression obtained with the cooled device.

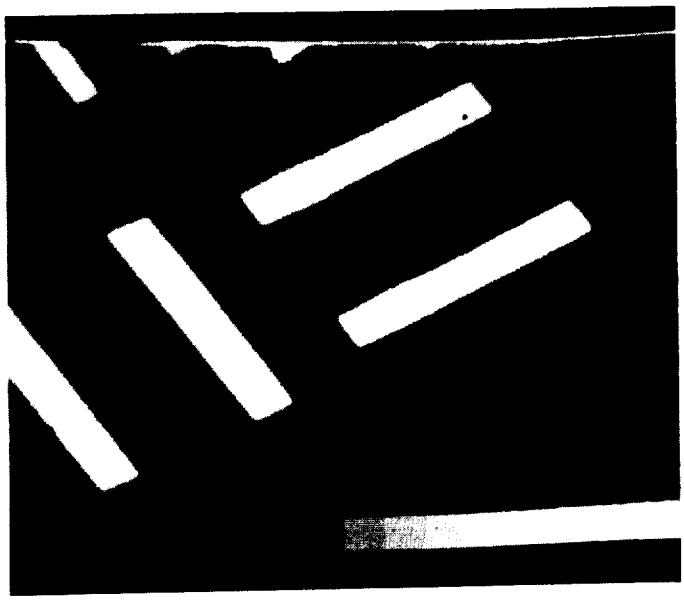

Figure 5. A shadowgraph taken at 44 Angstroms with the CCD camera. The exposure time was 6 minutes.

Detailed, quantitative measurements of the quantum efficiency (QE) of the CCD have been made. The QE is defined here as the ratio of the charge at the output gate of the device to the charge which would have been collected in a pixel if all the radiation incident on that pixel had been converted into electron-hole pairs (3.6 eV per electron-hole pair). The CCD camera with flight electronics was coupled to a test vacuum chamber with filtered electron bombardment sources of either carbon or aluminum K-alpha X-rays. Dosimetry was determined with cross calibrated gas flow proportional counters. An average ADC value over a 50 x 50 pixel array was computed by the GSE computer for each exposure.

In order to determine a charge at the CCD output gate from the ADC value, two quantities must be well known: the capacitance of the CCD output floating diffusion charge collector and the total electronic gain between the output gate and the ADC. The value of the output gate capacitance is taken from the calibration reports provided by RCA when the device was purchased. A value of 0.19 pF was obtained by measuring the output transistor discharge current during video rate readout of white light exposure. The gains of the various stages of the video chain are:

Sample and Hold Post Amplifier:	5.01
Sample and Hold Preamplifier:	3.55
Sample to Hold Switching:	0.90
Camera Head Preamplifier:	11.0
CCD Output:	0.99
Total	174.3

The QE for the Al source (1.49 keV) and C source (0.278 keV) are plotted in Figure 6. Also plotted in Figure 6 is the theoretical efficiency of a backside illumi-

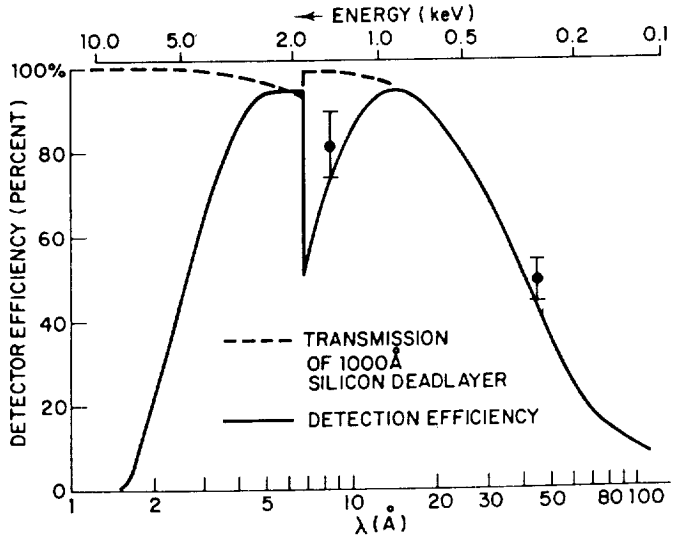

Figure 6. Measurements of the detector efficiency of the RCA SID 500 CCD detector and theoretical efficiency curve for a back-illuminated CCD thinned to 10 microns.

nated device 10 microns thick with a 1000 angstrom dead layer. Perfect charge collection and transfer are assumed. The low energy efficiency is determined by the filtering effect of the dead layer. The high energy efficiency is determined by the X-ray transmission of the 10 micron thick sensitive region. Error bars on the QE observations are representative of 10% uncertainty in output gate capacitance and electronic gains.

Flight Observations

X-ray images of the solar corona obtained during AS&E Solar Research Rocket flights on 15 August 1987 and 11 December 1987 are presented in Figures 7 and 8, respectively. The top image in each figure is a full disk photograph taken at the prime focus of the telescope. The lower image in each figure is a CCD image taken at the secondary focus of the telescope. All images are filtered through 1 micron of polypropylene and 3500 A of aluminum. The circles drawn on the full disk photographic images are 2 arc minutes in diameter and centered on the target region of the CCD exposure. The circles drawn on the CCD images are 2 arc minutes in diameter and centered on the region of maximum compound telescope throughput. Although the optical axis of the CCD/compound telescope system cannot currently be determined after final assembly, the CCD optical axis implied by the technique utilized in Figures 7 and 8 approximately agree with the optical axis last determined before final assembly. Review of the rapid decline in throughput with off-axis angle, as illustrated in Figure 2, instills confidence in this method of locating the optical axis of the CCD system for an image of any active region larger than 2 x 2 (arc min)^2.

The first impression created by the CCD images is the lack of resolved spatial structure. The on-axis resolution of the compound telescope as measured in the laboratory leads one to expect a high resolution core to the CCD image. While the off-axis aberrations illustrated in Figures 3 and 4 could combine in a non-intuitive way with the source image, the tentative conclusion on the spatial resolution of the flight images is that they do not match that obtained in the laboratory.

A second surprise is the lack of sensitivity of the flight observations. Calculations based on a typical 2.5 x 10^6 °K active region emission measure of 2 x 10^{29} cm^{-5} and the measured CCD and telescope performance indicates CCD saturation should be obtained with a 0.5 second exposure. Flight measurements imply that CCD saturation by the observed active region requires approximately an order of magnitude greater exposure!

The CCD X-ray response is found to increase linearly exactly as expected. For the CCD images with pixel values significantly above background, the histograms of pixel intensity are found to map into each other simply by the factor of exposure time. Therefore, the value of the CCD detector as a calorimeter has been established in these flight tests.

Conclusions

One possible explanation for the apparent lack of both spatial resolution and system throughput of the flight observations relative to the laboratory measurements is a misalignment of the relay optic. There are several ways in which such a misalignment could occur, including a deformation of the relay optic translation stage due to launch loads, extreme sensitivity to thermally induced changes in the optical bench, and a discrepancy between the ground-based white-light alignment technique and the in-flight, free-fall X-ray observation configuration. Pre-flight environmental testing was conducted on the relay optic translation stage to determine its sensitivity to launch loads. Damage to the translation stage during the reentry and recovery phase of both flights preclude a post-flight investigation of unexpected deformation of the stage during launch.

However, at the present level of analysis, it is premature to draw many conclusions. Two calculations are in progress which will address the question of whether the discrepancy between flight observations and laboratory measurements is real or illusory: (1) Since the rocket flights occurred near solar minimum, the observed active regions may have lower emission measures than typical active regions. Quantitative analysis is underway on the film images from these flights using standard techniques in order to determine the emission measures of the target regions. (2) The true convolution of the target active region emission with the point response function and geometrical aberration of the compound telescope as measured in the laboratory may result in the observed secondary focal plane image. It is possible that the narrow compound telescope field of view will only be useful for observing bright points and isolated active regions less than an arc minute in size. The calculation required to test this possibility is a deconvolution of the prime focus photographic image followed by a convolution of that image utilizing both the point response function and geometrical off-axis aberration of the compound telescope.

Finally, since two new systems were combined in the same observation, there remains an uncertainty as to which component did not perform in flight as it did in the lab. The CCD

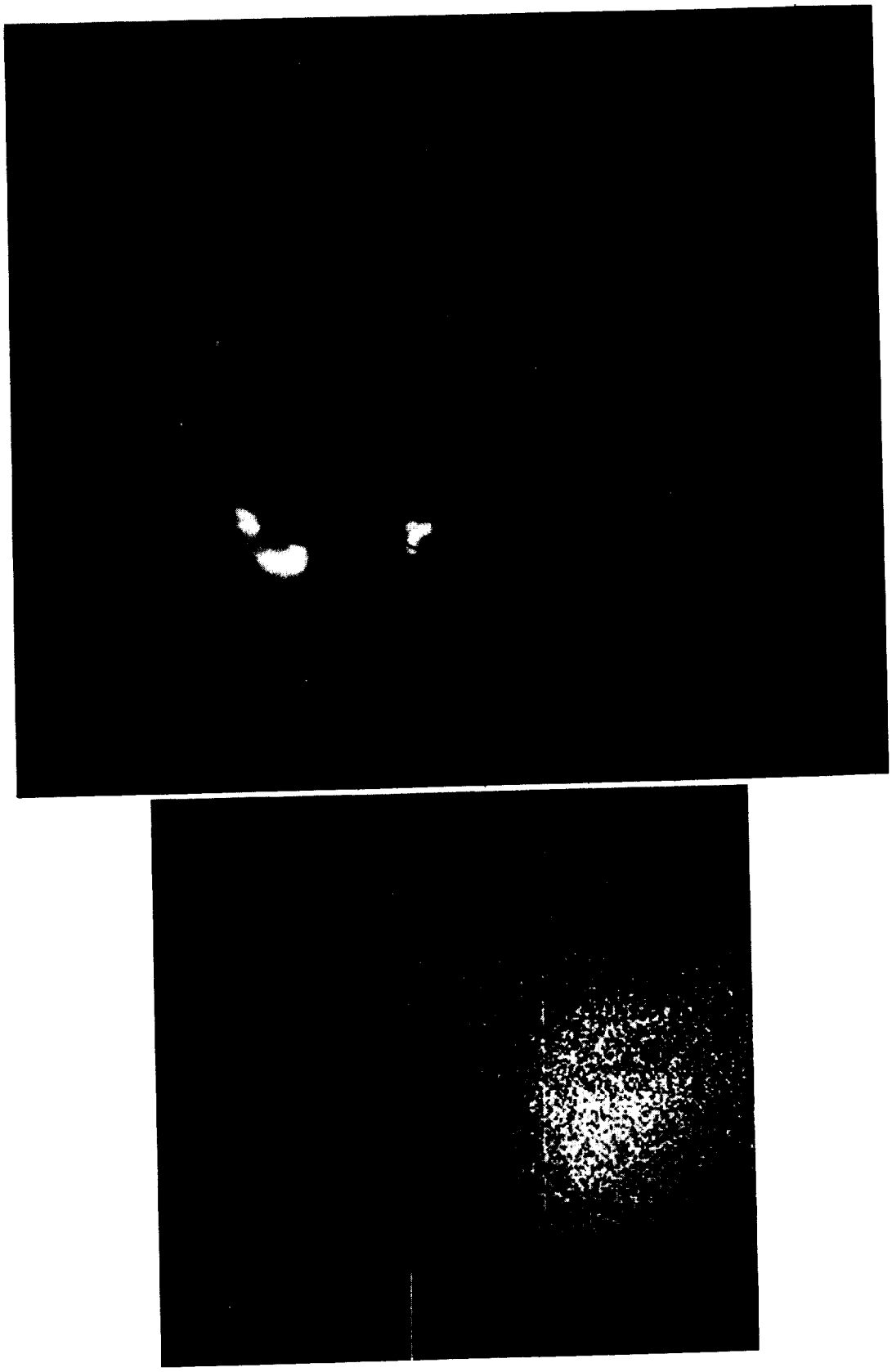

Figure 7. 15 August 1987 X-ray images of the solar corona through aluminized polypropylene filters. Both circles are 2 arc min diameter. Top: Full disk photographic image obtained at prime focus. Bottom: 0.280 second exposure CCD detector image obtained at secondary focus.

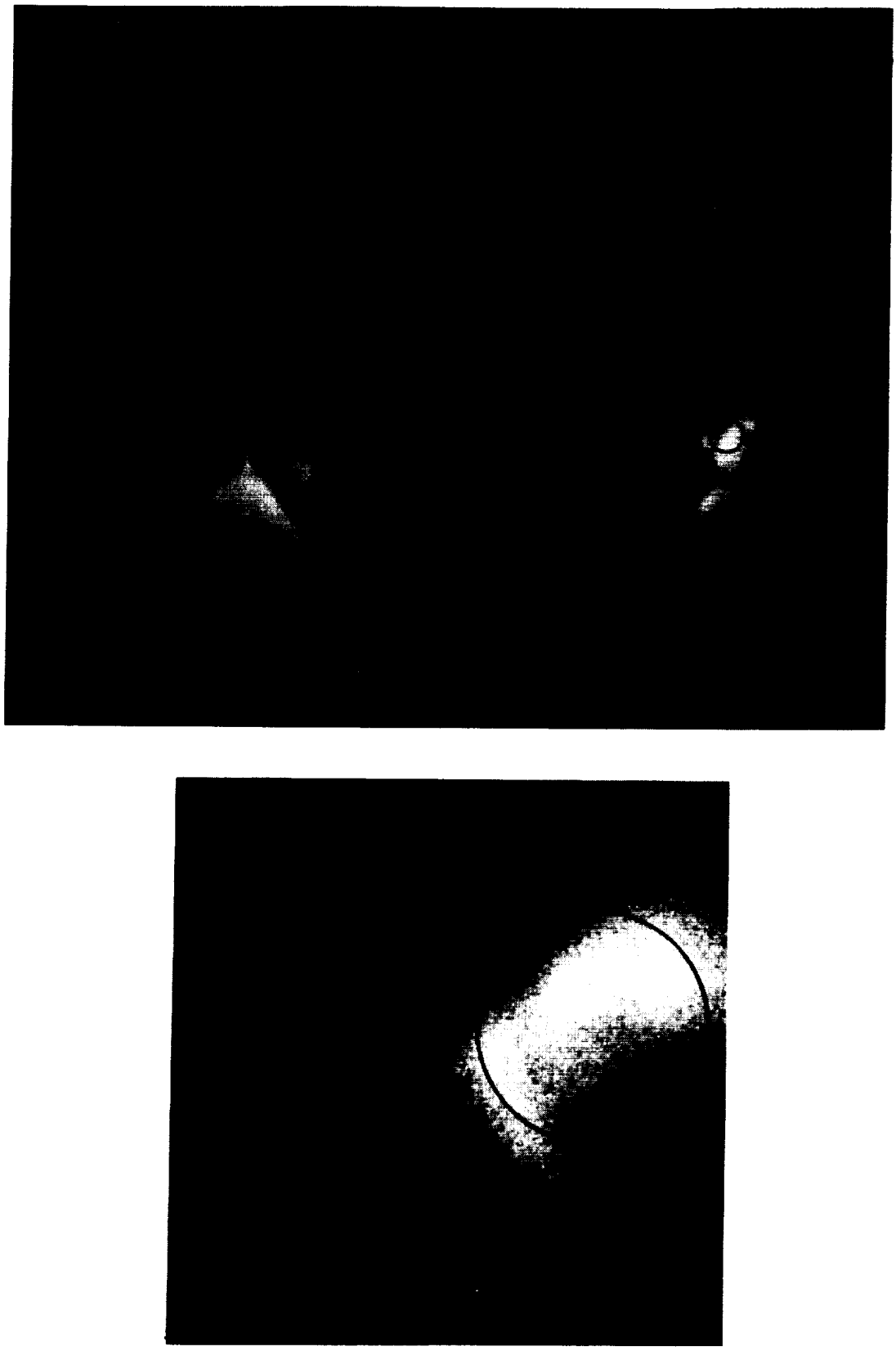

Figure 8. 11 December 1987 X-ray images of the solar corona through aluminized polypropylene filters. Both circles are 2 arc min diameter. Top: Full disk photographic image obtained at prime focus. Bottom: 1.0 second exposure CCD detector image obtained at secondary focus.

detector will be isolated with proven systems in the next planned flight of the AS&E Solar Research Rocket Payload. The payload will be configured with the CCD detector at the prime focus of the Wolter Schwarzschild mirror to obtain high precision calorimetry of large scale coronal structure. In this configuration the linearity and sensitivity (even in the worse case interpretation of the 1987 flight data as 10% of the laboratory efficiency) of the CCD detector will provide new and useful measurements of faint large scale coronal structures such as coronal holes and helmet streamers in which a 5 arc minute spatial resolution is useful. The insights gained from this flight on CCD performance can then be applied to the 1987 flight data.

Acknowledgments

We would like to acknowledge the efforts at AS&E of Ken Overoye in providing ray trace calculations and interpretations, Charles Carpenter and Frank Hills in providing electronics design, testing, and field support, and Roger Eng and Richard Schueller in providing mechanical design, testing, and field support. We would like to thank Drs. M. Annis, P. Bjorkholm, and A. Krieger for useful discussions. This work was performed under NASA contracts NAS5-25496 and NASW-3942.

References

1. E.N. Parker, Ap. J. 330 (1988) 474.

2. R.C. Chase, A.S. Krieger, and J.H. Underwood, Applied Opts. 21 (1982) 4446.

3. D. Moses, A.S. Krieger, and J.M. Davis, Proc. Soc. Photo-Opt. Instrum. Eng. 691 (1986) 138.

4. J.M. Davis, A.S. Krieger, J.K. Silk, and R.C. Chase, Proc. Soc. Photo-Opt. Instrum. Eng. 184 (1979) 96.

4.19 The Correspondence Between Small-Scale Coronal Structures and the Evolving Solar Magnetic Field

D.F. Webb

Emmanuel College
Boston, Massachusetts 02115

and

D. Moses

American Science and Engineering, Inc.
Cambridge, Massachusetts 02139